ABSTRACT

| | |
|---|---|
| Title of Dissertation: | DEPOSITION AND CHARACTERIZATION OF MULTIFERROIC BiFeO$_3$ THIN FILMS |
| | Junling Wang, Doctor of Philosophy, 2005 |
| Dissertation Directed By: | Professor Manfred Wuttig, Department of Materials Science and Engineering |

Multiferroics, defined as materials with coexistence of at least two of the electric, elastic, and magnetic orders, have attracted enormous research activities recently. A subsystem of multiferroics is the ferroelectromagnet, which possesses both electric and magnetic orders. One of the natural ferroelectromagnets is BiFeO$_3$, which has ferroelectric (T$_C$~1100K) and antiferromagnetic (T$_N$~640K) orders at room temperature. Even though bulk samples have been synthesized back in 1950s, characterizations of its intrinsic properties have been difficult due to poor sample quality.

This work is the first study on epitaxial BiFeO$_3$ thin films. Highly resistive films have been prepared using Pulsed Laser Deposition. (001), (110) and (111) cut SrTiO$_3$ substrates were used to control the film orientation. Film structures were characterized using both X-ray diffraction and transmission electron microscope. It was found that epitaxial stress changes the film structure. Monoclinic domain splitting was observed from both (101) and (001) oriented films, while (111) films remain rhombohedral

similliar to single crystals.

Much larger polarizations were observed for all three orientations (~55 $\mu C/cm^2$ for (001) films, ~80 $\mu C/cm^2$ for (101) films, and ~100 $\mu C/cm^2$ for (111) films). Calculation using the effective charges and reported ion displacements is performed; indicating that the large observed polarization is likely the intrinsic property of $BiFeO_3$. Magnetic measurements reveal that these resistive $BiFeO_3$ thin films show hysteresis behavior at room temperature, which was not observed in bulk single crystal under the same field range. Thickness dependence of the magnetic property was studied. It is proposed that epitaxial stress destroys the cycloidal spin structure of $BiFeO_3$, releasing the weak ferromagnetic property due to spin canting.

In addition, integration of $BiFeO_3$ with Si using $SrTiO_3$ template layer was also studied. Large dielectric constant and piezoelectric coefficients were observed, showing promise for applications in MEMs and actuators.

DEPOSITION AND CHARACTERIZATION OF MULTIFERROIC BiFeO$_3$ THIN FILMS

By

Junling Wang

Dissertation submitted to the Faculty of the Graduate School of the
University of Maryland, College Park, in partial fulfillment
of the requirements for the degree of
Doctor of Philosophy
2005

Advisory Committee:

     Professor Manfred Wuttig, Chair/Advisor
     Professor Lourdes G. Salamanca-Riba
     Visit Associate Professor Alison Flatau
     Professor Ichiro Takeuchi
     Professor Romel Gomez

# ACKNOWLEDGEMENTS

I would like to express my sincere gratitude to my advisor, Prof. M. Wuttig, for giving me the opportunity to work on this challenging and exciting project, and more importantly, his guidance and support throughout the course of my research. I benefited from all the discussions we had. It was his creative thoughts and suggestions that leaded to every progress during my Ph.D. study. The same gratitude goes to Prof. R. Ramesh, who served as my co-advisor before left for University of California, Berkeley. It is a great honor for me to have been a part of his team at the Advanced Thin Film Laboratory, which is at the forefront of research in oxide thin film materials. His enthusiasm, dedication and the drive for excellence in any task undertaken has been one of the primary motivating factors in this dissertation. I thank both of them for providing me with numerous opportunities to participate in conferences, for these are essential in building confidence and collaborations.

Also, I would like to thank Prof. D. Viehland at Virginia Tech for letting me to finish my research in his laboratory and helping me with my thesis writing. I will surly benefit from what I have learned during the 7 months throughout the rest of my life.

I would like to thank Prof. L. Salamanca-Riba, Prof. A. Flatau and Prof. I. Takeuchi for taking time out of their busy schedules to review my work. I specially thank Prof. I. Takeuchi for all the valuable discussions we had.

I would like to thank Prof. A. Roytburd and Dr. S. Ogale for all the useful and educational discussions.

I specially thank Dr. V. Nagarajan for leading me into the PLD thin film preparation, electrical characterization and structural analysis by XRD. I also thank Dr. S. Shinde for help with magnetic measurements.

I would like to thank Haimei Zheng for her help with the TEM analysis, most importantly, her constant encouraging and support during my research that helped me through all the difficult time.

All the friends and collaborators at Maryland, Dr. Tong Zhao, S. Y. Young, A. Prasertchoung, L. Mohaddes-Ardabili, Zhengkun Ma, Jianhua Li, Lang Chen and at Virginia Tech, Naigang Wang, Hu (Tiger) Cao, Li Yan, thank you. It is your friendships that make the work for Ph.D. more fun.

Finally, I want to thank my parents and my brother for their love and support. I own everything I achieved to them. This thesis is dedicated to them.

# TABLE OF CONTENTS

# LIST OF FIGURES

epitaxially grown on dissimilar cubic substrates. The second- and first-order phase transitions are shown by thin and thick lines, respectively. The triple or quadruple point at Sm=0 corresponds to the Curie-Weiss temperature u(x) of the stress-free bulk material. The dashed line indicates the (Sm ,T) conditions, at which the polarization in the r phase becomes oriented along the cube diagonal of the prototypic unit cell ($P_1=P_2=P_3$).

# LIST OF TABLES

# CHAPTER 1, INTRODUCTION

## 1.1 Ferroelectric and magnetic orders

### 1.1.1 Ferroelectricity and ferroelectric materials

**Ferroelectricity and perovskite ferroelectrics**

Ferroelectricity (FE) was first discovered in Rochelle salt in 1921. At that time, it was called Seignette-electricity, honoring its discoverer. For the past few decades, ferroelectric materials have received a great amount of interests because of their various uses in many applications such as nonvolatile ferroelectric random access memories (NVFRAM), dynamic random access memories, sensors and microactuators. [1]

A crystal is called to be ferroelectric when it possesses at least two equilibrium orientations of the spontaneous polarization vector in the absence of an external electric field, and the spontaneous polarization can be switched between those orientations by an electric field. The polar character of the orientation states should represent an absolutely stable configuration in null field. [2] Figure 1.1 shows a hysteresis loop illustrating polarization switching in ferroelectric materials. Important parameters such as coercive field (Ec), remnant polarization (Pr) and saturation polarization (Ps) are indicated in the figure.

It is well known that crystals can be classified into thirty-two crystal classes (point groups) according to the symmetry elements they possess. Among these thirty-two crystal classes, eleven of them are characterized by the existence of a center of symmetry: they are thus centrosymmetric. A centrosymmetric crystal can not posses any polar properties. The remaining twenty-one crystal classes do not have a center of symmetry; thus, it is possible for them to (i) have one or more polar axes, (ii) possess odd-rank tensor properties. With one exception (i.e., the group 432 which lacks a center of symmetry, but has other symmetry operations that destroy polarity), all

non-centrosymmetric point groups exhibit piezoelectric effect that is defined by a change in electric polarity under applied stress, and vice versa, that is the converse piezoelectric effect.

Out of the twenty piezoelectric classes, ten possess a unique polar axis. Crystals in these classes are called polar because they are spontaneously polarized. The value of the spontaneous polarization depends on temperature. When temperature changes, a change in the polarization occurs and electric charges can be observed on those crystal faces perpendicular to the polar axis. This is called the pyroelectric effect. The ten crystal classes with a unique polar axis are also called pyroelectric classes. Ferroelectric crystals belong to the pyroelectric family, but they only constitute the part that the direction of the spontaneous polarization can be reversed by external electric field. A complete analysis of symmetry and its relation to the ferroelectric phase transition has been summarized by Aizu. [3]

Among all the ferroelectric materials, the most extensively studied and widely used are the perovskite ferroelectrics. A perfect perovskite structure has a general formula of $ABO_3$, where A represents a divalent or trivalent cation, and B is typically a tetravalent or trivalent cation. The origin of ferroelectricity in this family of materials can be explained using the well-known example of barium titanate ($BaTiO_3$). As shown in Figure 1.2, the $Ba^{2+}$ cations are located at the corners of the unit cell. A dipole moment occurs due to relative displacements of the $Ti^{4+}$ and $O^{2-}$ ions from their symmetrical positions.
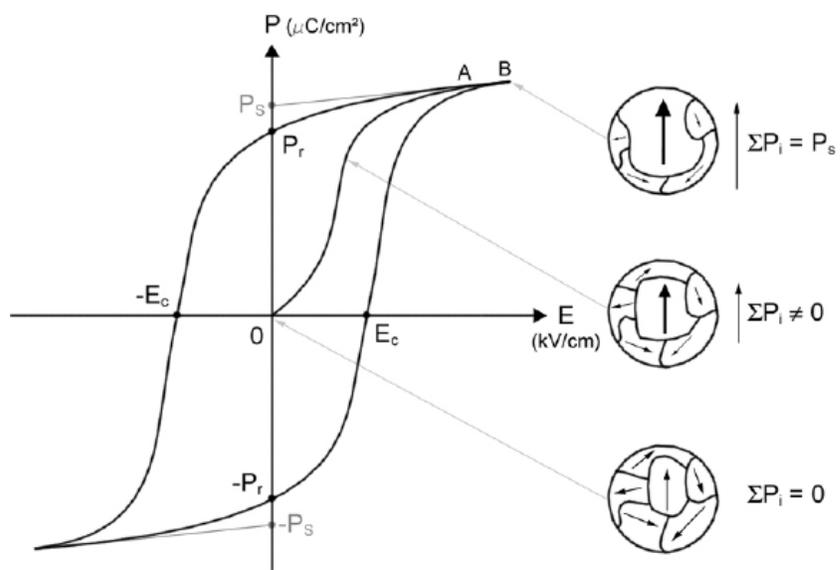
Figure 1. 1 Ferroelectric hysteresis loop illustrating the polarization switching. Figure adapted from Ruette. [4]
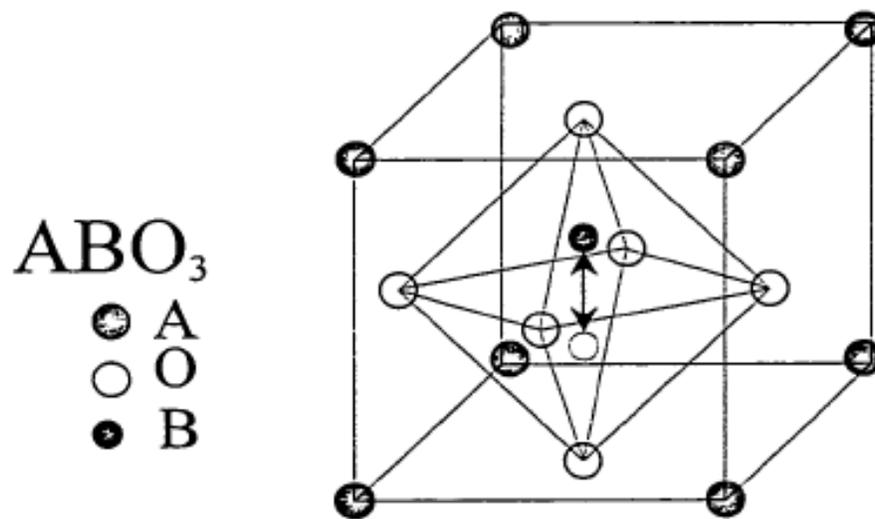
Figure 1. 2 Schematic illustration of the unit cell of perovskite ferroelectric materials.

Figure adapted from Li. [43]

**Lattice dynamic (soft phonon) theory of ferroelectricity**

In displacive ferroelectric materials, the spontaneous polarization is generated by minute displacements of atoms in the unit cell. About fifty years ago, Cochran and Anderson, [5, 6] suggested that the phase transition in these ferroelectrics might result from instability of one of the normal vibration modes of the lattice. According to this theory, for one particular normal mode, it is possible for the short range (ionic coulomb forces) and long range (dipole interaction) forces to almost cancel each other at certain temperatures. The total restoring force is then very small and the crystal becomes unstable for that particular mode. This mode is called the soft phonon or soft mode. The frequency of the soft phonon decreases when the temperature approaching the critical temperature. The restoring force decreases to zero, finally the phonon condenses out at the stability limit.

**Thermodynamic (Laudau-Ginzburg-Devonshire) theory**

While the soft phonon model gives the correlations between microscopic lattice vibrations and the macroscopic properties such as polarization, the thermodynamic theory correlates different macroscopic properties (such as polarization, dielectric constant and temperature). In the basic Landau-Devonshire theory, [7] one assumes that the free energy can be expanded in a power series of the order parameters for the system. For a ferroelectric, the macroscopic order parameter is polarization $P$.

$$F(P,T,E) = -EP + \alpha_0 + \frac{1}{2}\alpha_1 P^2 + \frac{1}{4}\alpha_2 P^4 + \frac{1}{6}\alpha_3 P^6 + ... \qquad \text{Equation 1.1}$$

where $\alpha_n$ is the dielectric stiffness that depends on the temperature, and n is the tensor rank of the stiffness. This series expansion does not contain terms in odd power of $P$ when the unpolarized crystal (parent phase) has a center of symmetry, which is generally true for most perovskite ferroelectrics. One can get the spontaneous

5

polarization $P_s$ in thermal equilibrium by minimizing the free energy as a function of P; differentiating equation 1.1 with respect to P gives

$$\frac{\partial F}{\partial P} = 0$$
$$-E + \alpha_1 P + \alpha_2 P^3 + \alpha_3 P^5 + ... = 0$$

Equation 1.2

The coefficient $\alpha_1$ is temperature dependent and of the form $\alpha_1 = \gamma(T - T_0)$, where $\gamma$ is a positive constant and $T_0$ may be equal to or lower than the phase transition temperature. This form of $\alpha_1$ is a necessary result of mean field theory, and its validity is supported by the experimentally observed Curie-Weiss law. A negative value of $\alpha_1$ would mean that the unpolarized state is unstable, i.e., the system is ferroelectric.

When $\alpha_2$ is positive, we can neglect the $\alpha_3$ term. The polarization under zero field can then be found from equation 1.2, given as

$$\gamma(T - T_0)P_s + \alpha_2 P_s^3 = 0$$

Equation 1.3

From this equation, either $P_s = 0$ or $P_s^2 = \frac{\gamma}{\alpha_2}(T_0 - T)$. For $T \geq T_0, P_s = 0$ since $\gamma$ and $\alpha_2$ are positive. For $T < T_0$, $|P_s| = \sqrt{\frac{\gamma}{\alpha_2}(T0 - T)}$. The minimum of the free energy under zero field is plotted in Figure 1.3 (a). The change of the free energy and polarization at the transition temperature are continuous. This is a second order transition.

When $\alpha_2$ is negative, we must retain $\alpha_3$ and take a positive value to keep F converged. The equilibrium condition is then

$$\gamma(T - T_0)P_s + \alpha_2 P_s^3 + \alpha_3 P_s^5 + ... = 0.$$

Equation 1.4

In this equation, either $P_s = 0$ or $\gamma(T - T_0) + \alpha_2 P_s^2 + \alpha_3 P_s^4 + ... = 0$. At the transition temperature, the free energies of the paraelectric and ferroelectric phases are equal.

6
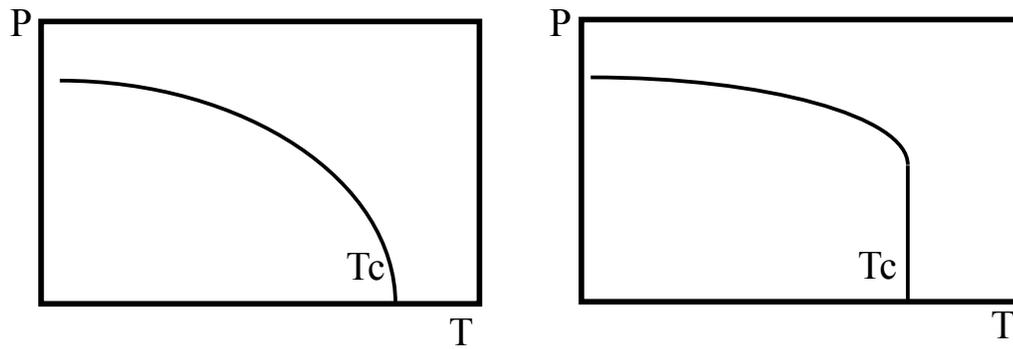
Figure 1. 3 Polarization vs. temperature plot for (a) second order and (b) first order phase transitions

| Ferroelectric phase stable | Ferroelectric phase stable<br>Non-polar phase meta-stable | Non-polar phase stable<br>Ferroelectric phase meta-stable | Non-polar phase stable |
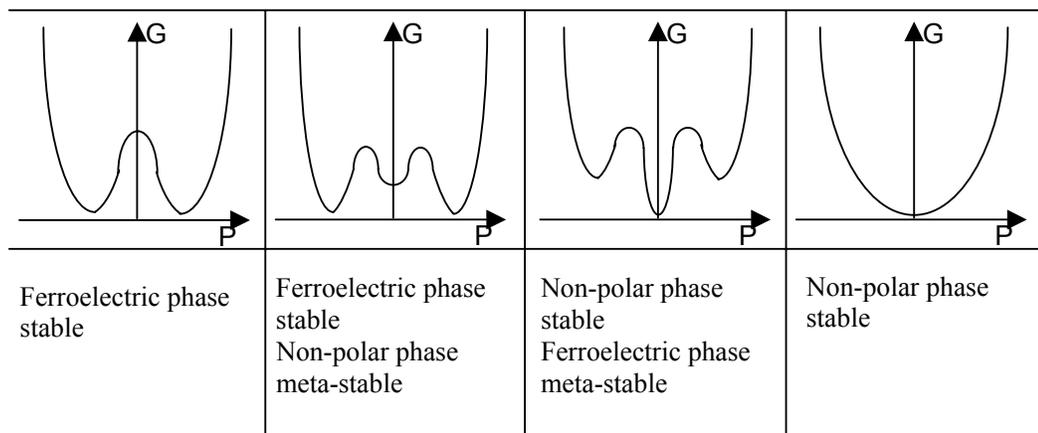
Figure 1. 4 Gibbs free energies as functions of polarization in a first order phase transition. Figure adapted from [2].

The plot of the free energy versus polarization at different temperature is shown in Figure 1.4. The existence of meta-stable phases during the phase transition is characteristic for first order transitions. Correspondingly, a sudden jump of polarization occurs at Tc. Figure 1.3 (b) plots the $P_s$ versus temperature for a first order phase transition.

### 1.1.2 Magnetism and magnetically ordered states

Magnetism is inseparable from quantum mechanics: a strictly classical system in thermal equilibrium can display no magnetic moment, even in a magnetic field. [7] The magnetic response of a material comes from the atoms/ions forming its lattice. The magnetic moment of an atom/ion has three principal sources: (1) the spin of electrons; (2) electron orbital angular momentum about the nucleus; and (3) a change in the orbital moment induced by an applied magnetic field. The first two effects give paramagnetic contributions to the magnetization, and the third gives a diamagnetic contribution. For example, in the ground 1s state of the hydrogen atom the orbital moment is zero, the magnetic response consists of the spin of that electron along with a small diamagnetic moment. In the $1s^2$ ground state of helium atom, the electron spins cancel due to Pauli Law, and the orbital moment is also zero. The magnetic response is only that of an induced diamagnetic moment.

In a crystal, the overall magnetic property depends on two factors: (i) the magnetic response associated with each atom/ion, and (ii) the interactions between these magnetic moments. In the case that there are no unpaired electrons around each atom/ion, there will be no net magnetic moments associated with them (bearing in mind that both orbital moments and electron spins cancel to zero in a fully filled orbital), the material will show diamagnetic behavior. When there are unpaired

electrons, every atom/ion has a net magnetic moment. Depending on the interactions between the magnetic dipoles, the material may show (i) paramagnetism (PM); (ii) ferromagnetism (FM); (iii) antiferromagnetism (AFM) and (iv) ferrimagnetism (FIM). In a paramagnetic material, alignment of adjacent moments is not observed due to thermal fluctuation. Ferromagnetism consists of parallelly aligned adjacent moments. Antiferromagnetic order consists of antiparallel aligned equal moments. And, ferrimagnetic order consists of antiparallel unequal moments, resulting in a non-zero net magnetization. Figure 1.5 illustrates FM, FIM and AFM type spin orderings.

The magnetic susceptibility, $\chi = \dfrac{dM}{dH}$, which defines the strength of materials' response to an external field, is a good indication of their magnetic properties.

**The Weiss theory and Heisenberg exchange interaction**

Ferromagnetism is a very strong magnetic response compared with paramagnetic and diamagnetic behavior. It is characterized by a transition temperature (Curie temperature, $T_c$). Above this temperature, the material is paramagnetic. Below this temperature, it is ferromagnetic and characterized by hysteresis response in external magnetic field, as shown in Figure 1.6. The saturation magnetization ($M_s$), coercive field ($H_c$) and remnant magnetization ($M_r$) are all shown in the figure. Based on the value of coercive field, magnetic materials are classified into hard and soft magnets.
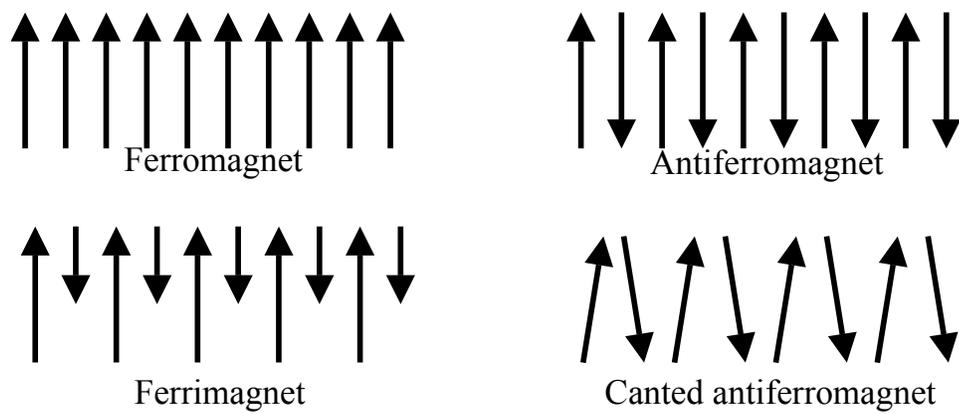
Figure 1. 5 Schematic picture of ferromagnetic, antiferromagnetic, ferrimagnetic and canted antiferromagnetic orders. Figure adapted from [7].
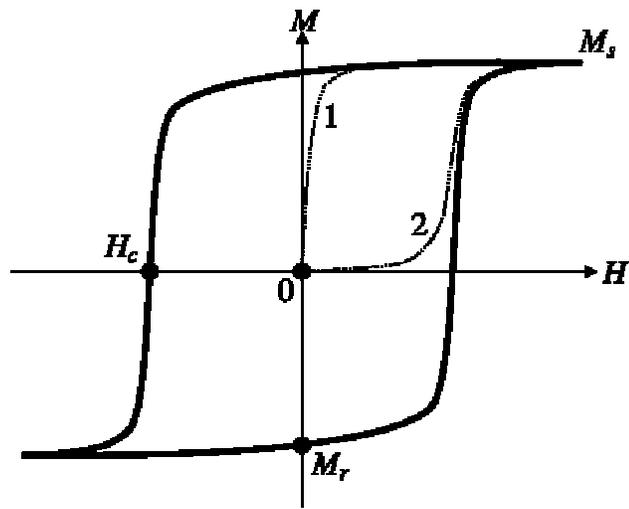
Figure 1. 6 Schematic of a magnetization hysteresis loop showing the saturation magnetization, Ms, coercive field, Hc and remanent magnetization, Mr. Virgin curves are shown dashed for nucleation (1) and pinning (2) type magnets. Figure adapted from [7]

To explain the spontaneous alignment of the spins and the hysteresis loop developed in the ferromagnetic materials, Weiss proposed that (1) there is a strong internal magnetic field (proportional to the magnetic moment) which aligns the dipoles even without an external field; and (2) macroscopically, there are small regions, called domains, each of them spontaneously magnetized. The magnetic moment of the entire specimen is then the vector sum of the magnetic moment of each domain. Since the direction of each domain may not be parallel, certain domain configurations lead to zero net moment. The application of a relatively small field changes the domain arrangement, and hence an appreciable change in net magnetization. Domain switching under external field produces hysteresis loop.

While the Weiss theory successfully explained the spontaneous magnetization and hysteresis, it was hard to interpret where such a huge internal field ($\sim 10^7$Oe) came from before the advance of quantum mechanics. In 1928, Heisenberg [8] showed that this internal field was the result of the quantum mechanical exchange interaction. This interaction has no classical analog. Heisenberg's theory is based on the Heitler-London method developed for the hydrogen molecule. The main features of this theory are as follows. In a two electrons system such as helium atom or the hydrogen molecule, if the interaction between electrons is neglected, then the Schrödinger equation can be given as

$$[-\frac{\hbar^2}{2m}(\nabla_1^2 + \nabla_2^2 + V(q_1) + V(q_2)]\psi = E\psi \ ; \qquad\qquad \text{Equation1.5}$$

where the subscripts 1 and 2 refer to the two electrons, considered distinguishable. The possible solutions are then

$$\psi_a(1)\psi_b(2) \ \text{ and } \ \psi_a(2)\psi_b(1) \ ; \qquad\qquad \text{Equation1.6}$$

with $E = E_a + E_b$ for both cases. Here, $\psi$ is the one-electron wave function. $\psi_a(2)$

and $\psi_b(1)$ mean when the electrons are interchangeable. However, the electrons are indistinguishable, and thus it is necessary that

$$|\psi(1,2)|^2 dq_1 dq_2 = |\psi(2,1)|^2 dq_1 dq_2;$$

where $\psi(1,2)$ is the wave function that describes the two electron system, and $\psi(2,1)$ is that of the state when the two electrons are interchanged. It is easy to see that either

$$\psi(1,2) = \psi(2,1) \quad \text{or} \quad \psi(1,2) = -\psi(2,1). \qquad \text{Equation 1.7}$$

Neither of the wave functions in equation 1.6 satisfies these requirements. However, the linear combinations

$$\psi_{sym}(1,2) = A[\psi_a(1)\psi_b(2) + \psi_a(2)\psi_b(1)] \qquad \text{Equation 1.8}$$

$$\psi_{anti}(1,2) = B[\psi_a(1)\psi_b(2) - \psi_a(2)\psi_b(1)] \qquad \text{Equation 1.9}$$

do satisfy equations 1.7, respectively.

Now we need to remember that these are only functions of the spatial coordinates, and not the spin. To get a complete wave function of the system, we need to take into account the electron spins and keep in mind that the Pauli exclusion principle requires that no two electrons can be in the same state. The following is the system functions for a two-electron system, as functions of both spatial coordinates and spin

$$\psi_1 = A[\varphi_a(1)\varphi_b(2) + \varphi_a(2)\varphi_b(1)][\chi_\alpha(1)\chi_\beta(2) - \chi_\alpha(2)\chi_\beta(1)] \qquad \text{Equation 1.10}$$

$$\psi_1 = A[\varphi_a(1)\varphi_b(2) - \varphi_a(2)\varphi_b(1)] \begin{bmatrix} \chi_\alpha(1)\chi_\alpha(2) \\ \chi_\alpha(1)\chi_\beta(2) + \chi_\alpha(2)\chi_\beta(1) \\ \chi_\beta(1)\chi_\beta(2) \end{bmatrix}; \qquad \text{Equation 1.11}$$

where $\varphi(r)$ is the solution of the Schrodinger equation for an electron without spin and $\chi$ is a function of the spin coordinates only, and A and B are normalizing factors. If the two electrons have a common z-axis, equation 1.10 represent the situation in which the electron spins are antiparallel (S=0, singlet state), whereas equation 1.11 represents the

situation in which the spins are parallel (S=1, triplet states) with components Ms=1,0,-1, respectively. The energies for these states are, respectively

$$E_1 = A^2(K_{12} + J_{12}) \text{ and } E_2 = B^2(K_{12} - J_{12})$$

where $K_{12} = \int \varphi_a*(1)\varphi_b*(2)H_{12}\varphi_a(1)\varphi_b(2)d\tau_1 d\tau_2$

and $J_{12} = \int \varphi_a*(1)\varphi_b*(2)H_{12}\varphi_a(2)\varphi_b(1)d\tau_1 d\tau_2$.

Here $K_{12}$ is the average Coulomb interaction energy and $J_{12}$ is called an exchange integral that is a direct result of the electrons indistinguishability. $H_{12}$ is the Hamiltonian for the interaction between the two electrons. Depending on whether $J_{12}$ is positive or negative, spins of the two electrons tend to align parallel or antiparallel.

## 1.2 Multiferroic materials and magnetoelectric effect

The term multiferroic is used to describe materials in which two or all three of the ferro-properties, - ferroelectricity, ferro/ferrimagnetism, and ferroelasticity - occur simultaneously. In a broader definition, it also covers materials with ferro- and antiferro- properties or pure antiferro- properties. Specific device applications that have been suggested for such materials include multiple-state memory elements, magnetic field sensors, electric-field-controlled ferromagnetic resonance devices, and transducers with magnetically modulated piezoelectricity. In addition, the ability to couple with either the magnetic or the electric polarization offers an extra degree of freedom in the design of conventional devices. More of the possible applications of multiferroic materials can be found the in previous review papers. [9,11]

### 1.2.1 Single Phase multiferroic materials: a brief history [10]

Boracites. The first ferromagnetic ferroelectric material to be discovered was

nickel iodine boracite, $Ni_3B_7O_{13}I$. This was followed by the synthesis of many more multiferroic boracite compounds, all of which have complex structures with many atoms per formula unit and more than one formula unit per unit cell. The large number of inter-ionic interactions in these materials prevented the isolation both of the essential factors causing multiferroism and of the nature of the coupling between the magnetic, electric, and structural order parameters. Nickel iodine boracite can be thought of as the "Rochelle salt" of magnetic ferroelectrics. It is invaluable for demonstrating proof of concept, but unlikely to find wide applicability or to contribute to our increased understanding in the field.

Mixed Perovskites. The search for other ferromagnetic ferroelectrics began in Russia in the 1950s, with the replacement of some of the $d^0$ B cations in ferroelectric perovskite oxides by magnetic $d^n$ cations, hoping that the dipole displacement will remain and the exchange interaction between the diluted magnetic ions is strong enough to give magnetic orders. The first synthetic ferromagnetic ferro-electric material, $(1-x)Pb(Fe_{2/3}W_{1/3})O_3 - xPb(Mg_{1/2}W_{1/2})O_3$, was produced in the early 1960s using this approach. Here, the Mg and W ions are diamagnetic and cause the ferroelectricity, and the formally $d^5$ $Fe^{3+}$ ion is responsible for the magnetic ordering. Other examples include B-site-ordered $Pb(Co_{1/2}W_{1/2})O_3$, which is ferroelectric and ferromagnetic; B-site disordered $Pb(Fe_{1/2}Ta_{1/2})O_3$, which is ferroelectric and antiferromagnetic. As a result of dilution of the magnetic ions, these materials all have rather low Curie or Neel temperatures.

Other Perovskites. A number of other perovskite materials are known to have ferroelectric and magnetic (mostly of the antiferromagnetic type) ordering. These include the manganites of the small rare earth elements and yttrium and a few compounds in which Bi is the large cation. Previous work on multiferroic materials

and their possible applications can be found in references. [11,12]

Table 1.1 lists some of the known multiferroic materials, adapted from reference 11. The readers are referred to the original paper for a complete list.

### 1.2.2 Multiferroic composites

The choices of single-phase materials exhibiting the coexistence of strong ferro /ferrimagnetism and ferroelectricity at room temperature are quite limited. Van Suchtelen et al. proposed that composites of piezoelectric and magnetostrictive phases can be electromagnetically coupled via stress mediation. [13] Subsequent theoretical and experimental works have focused on bulk ceramics. Lots of efforts have been devoted into this area, see for example, references [14,15,16,17,18].

### 1.2.3 Magnetoelectricity: Thermodynamic consideration

The first study of magnetoelectricity was by Landau and Lifshitz. [19] By using the Neumann's principle (stated "The symmetry elements of any physical property of a crystal must include the symmetry elements of the point group of the crystal."), they predicted the existence of ME effects based on the symmetry of the magnetic property tensors. The first explicit prediction of a ME effect in a material was by Dzyaloshinskii, [20] who showed that $Cr_2O_3$ had a ME effect, which is allowed by the magnetic symmetry. The effect was experimentally observed for the first time in an unoriented $Cr_2O_3$ crystal by Astrov. [21] Rado and Folen [22] then revealed the anisotropic nature of the ME effect in oriented $Cr_2O_3$ crystals. These investigations defined what we now call the electric field induced ME effect [$(ME)_E$ effect]. Later, Rado and Folen observed the converse effect, the magnetic field induced ME effect [$(ME)_H$ effect].

Table 1.1 Examples of materials that exhibit ME effect. Notation: FE-ferroelectric, AFE-antiferroelectric, FM-ferromagnetic, AFM-antiferromagnetic and WFM-weak ferromagnetic. Table adapted from Smolenskii. [11]

| Compound | Type of electric order | Type of magnetic order | $T_C$ (K) | $T_N$ (K) |
|---|---|---|---|---|
| $Pb(Fe_{2/3}W_{1/3})O_3$ | FE | AFM | 178 | 363 |
| $Pb(Fe_{1/2}Nb_{1/2})O_3$ | FE | AFM | 387 | 143 |
| $Pb(Co_{1/2}W_{1/2})O_3$ | FE | WFM | 68 | 9 |
| $Pb(Mn_{2/3}W_{1/3})O_3$ | AFE? | AFM | 473 | 203 |
| $Pb(Fe_{1/2}Ta_{1/2})O_3$ | FE | AFM | 233 | 180 |
| $Eu_{1/2}Ba_{1/2}TiO_3$ | FE | FM | 165 | 4.2 |
| $BiFeO_3$ | FE | AFM | 1123 | 650 |
| $BiMnO_3$ | AFE | FM | 773 | 103 |
| $YMnO_3$ | FE | AFM | 913 | 80 |
| $YbMnO_3$ | FE | AFM/WFM | 983 | 87.3 |
| $HoMnO_3$ | FE | AFM/WFM | 873 | 76 |
| $ErMnO_3$ | FE | AFM | 833 | 79 |
| $Ni_3B_7O_{13}I$ | FE | WFM | 64 | 64 |
| $Ni_3B_7O_{13}Br$ | FE | WFM | 398 | 30,40 |
| $Co_3B_7O_{13}I$ | FE | WFM | 197 | 38 |
| … | … | … | … | … |

The equation of state for magnetoelectricity has been derived using thermodynamic considerations. The magnetoelectric effect is a secondary ferroic effect with a Gibbs energy of the form

$$-dG = SdT + P_i dE_i + M_i dH_i - \varepsilon_{ij} d\sigma_{ij} ;$$   Equation 1. 12

where $S$ is the entropy, $P_i$ the polarization vector, $M_i$ the magnetization vector, $\varepsilon_{ij}$ the elastic strain tensor, $E_i$ the applied electric field, $H_i$ the applied magnetic field, and $\sigma_{ij}$ the applied stress. Under an isothermal condition, the term $-SdT$ is zero. And, assuming zero applied stress, the last term of equation 1.12 also becomes zero. Using a Maclaurin two-variable expansion (equivalent to a Newtonian two-variable series at 0), equation 1.12 becomes

$$-G = P_i E_i + M_i H_i + \frac{1}{2}\varepsilon_0\varepsilon_{ij}E_i E_j + \frac{1}{2}\mu_0\mu_{ij}H_i H_j + \alpha_{ij}E_i H_j + \frac{1}{2}\beta_{ijk}E_i H_j H_k + \frac{1}{2}\gamma_{ijk}H_i E_j E_k + ... ;$$   Equation 1.13

where $\alpha_{ij}$ is the linear magnetoelectric coefficient (2nd rank property tensor which contains 9 independent coefficients), and $\beta_{ijk}$ and $\gamma_{ijk}$ are the quadratic magnetoelectric coefficients ($3^{\text{rd}}$ rank property tensor, 27 coefficients). The ME coefficient $\alpha$ is a second rank tensor with a maximum of nine independent coefficients. In matrix form, $\alpha$ is given as

$$\alpha = \begin{bmatrix} \alpha_{11} & \alpha_{12} & \alpha_{13} \\ \alpha_{21} & \alpha_{22} & \alpha_{23} \\ \alpha_{31} & \alpha_{32} & \alpha_{33} \end{bmatrix}.$$

Table 2.2 presents the possible couplings between magnetic and polarization ordering. To derive the resultant polarization $P_i$, equation 1.13 can be differentiated with respect to $E_i$, given as

$$P_i = -\frac{\partial G}{\partial E_i}$$

$$= P_i^s + \frac{1}{2}\varepsilon_0\varepsilon_{ij}E_j + \alpha_{ij}H_j + \frac{1}{2}\beta_{ijk}H_jH_k + \frac{1}{2}\gamma_{jki}H_jE_k + ...$$

Equation 1.14

The induced polarization when $E = 0$ is

$$P_i = P_i^s + \alpha_{ij}H_j + \frac{1}{2}\beta_{kij}H_jH_k + \frac{1}{2}\gamma_{jki}H_jE_k + ...;$$

Equation 1.15

where $\alpha_{ij}$ is the linear and $\beta_{kij}$, $\gamma_{jki}$ are the quadratic magnetoelectric coefficients.

Table 1.2 Terms of the density of stored "free enthalpy", g, for magnetic and electric phenomena. Terms of strain-electric and strain-magnetic are omitted.

| Terms of the density of stored "free enthalpy" | Corresponding phenomena | Name of coefficient |
|---|---|---|
| $P_i E_i$ | Ferroelectricity | Spontaneous polarization |
| $M_i H_i$ | Ferromagnetism | Spontaneous magnetization |
| $\frac{1}{2}\varepsilon_0\varepsilon_{ij}E_iE_j$ | Induced polarization | Electric susceptibility |
| $\frac{1}{2}\mu_0\mu_{ij}H_iH_j$ | Induced magnetization | Magnetic susceptibility |
| $\alpha_{ij}E_iH_j$ | Magnetoelectric effect | Magnetoelectric susceptibility |
| $\frac{1}{2}\beta_{ijk}E_iH_jH_k$ | Second order magnetoelectric effect (1) | First non-linear magnetoelectric susceptibility |
| $\frac{1}{2}\gamma_{ijk}H_iE_jE_k$ | Second order magnetoelectric effect (2) | Second non-linear magnetoelectric susceptibility |

### 1.3 Ferroelectric/antiferromagnetic BiFeO₃

BiFeO₃ is one of the few single phase materials that show both ferroelectric and antiferromagnetic properties at room temperature. It was first synthesized in 1957 by Royen and Swars. Numerous studies have been devoted to this compound, mostly on ceramics, motivated by the potential high magnetoelectric property. But for many years, structural and physical properties of BiFeO₃ remained the subject of controversies between different laboratories.

### 1.3.1 Structure of BiFeO₃

The atomic structure of BiFeO₃ was determined by Michel et al. in 1969. [23] They performed X-ray diffraction on single crystal and neutron diffraction on powder samples. The space group is R3c, the rhombohedral unit cell contains two formula units of BiFeO₃. Fig 1.7 shows the hexagonal unit cell of BiFeO₃.

The displacement of each ion is shown in Fig 1.8. Owing to the oxygen shifts, the ideal cell is not unit cell of BiFeO₃. Instead the primitive cell is a rhombohedron containing 2 formula units of BiFeO₃. The magnitude of ion shifts are Bi: 0.62 Å along [111]; Fe: 0.23 Å along [111]; O: 0.30Å along [111], all values ± 0.03 Å. The nature of the oxygen shifts is more easily visualized by considering the atomic positions and shifts on a (111) rhombohedral plane. It is seen that the oxygen shifts are essentially along a line between the projections of two Bi atoms on this plane. In the ideal perovskite structure, Bi atoms would lie in this (111) plane, but in BiFeO₃, Bi shifts 0.62 Å normal to the plane. The unit cell of BiFeO₃ is not the unimolecular cell shown in Fig 1.8, but may be represented by a rhombohedron, having twice the volume of the unimolecular cell, and generated by taking three face diagonals meeting at a vertex of the cube shown as three intersecting edges of the rhomboherdon.

22
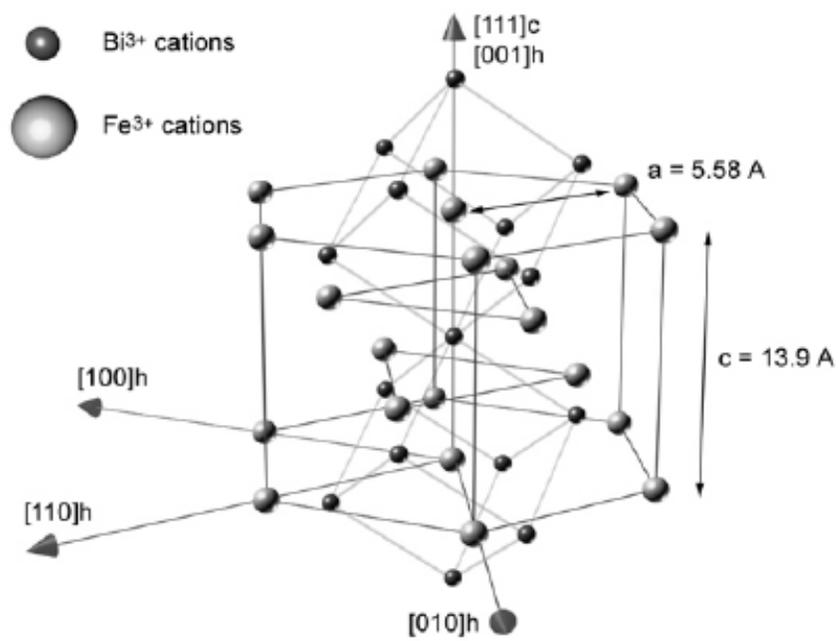
Figure 1. 7 Hexagonal unit cell of $BiFeO_3$. Figure adapted from Ruette et al. [4]
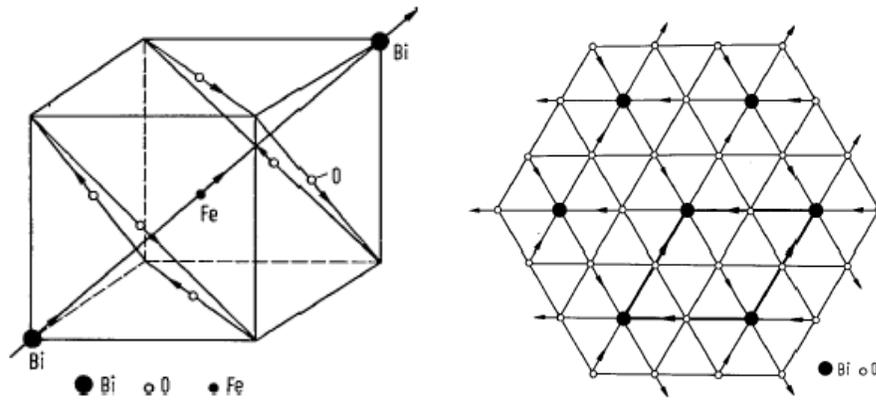
Figure 1. 8 Ion shifts in BiFeO$_3$, shown superimposed on the ideal perovskite cell.

Figure adapted from Michel et al. [23]

In this report, the authors also pointed out based on structural analysis that, 1) electric reversal of the Bi and Fe shifts would require a very high electrical field; 2) the oxygen distortion may be responsible for the comparatively low values of the dielectric constant observed at the Curie peak; 3) the space group R3c permits weak ferromagnetism.

There have been extensive studies trying to determine the lattice parameters and phase transition temperatures of $BiFeO_3$. Bucci et al reported the following results in 1971 [24]: At $25.13\pm0.02$°C, the hexagonal parameters are $a_h=5.5799\pm0.0003$ and $c_h=13.8670\pm0.0005$Å, transforming to the rhombohedral cell yields: $a_{Rh}=5.6336\pm0.0003$ Å and $\alpha_{Rh}=59°20.86\pm0.30$'. The linear coefficients of thermal expansion are determined to be

| Temperature range (°C) | $\alpha_t = \frac{1}{x_0}(\frac{\partial x}{\partial t})_P$ (deg$^{-1}$) |
|---|---|
| 25.13 - 325 | $\alpha_{ah} = 10.9 \times 10^{-6}$ <br><br> $\alpha_{ch} = 15.1 \times 10^{-6}$ |
| 344 - 838 | $\alpha_{ah} = 12.2 \times 10^{-6}$ <br><br> $\alpha_{ch} = 65.0 \times 10^{-6} - 18.0 \times 10^{-8} t + 20.3 \times 10^{-11} t^2 - 10.3 \times 10^{-14}$ |

More studies about the structure, lattice parameters and atomic displacements can be found in other literatures. [25,26,27,28]

### 1.3.2 Electrical properties of BiFeO$_3$

Electrical characterization on bulk BiFeO$_3$ has been very difficult due to the low resistivity of samples. The controversy about whether it is ferroelectric or antiferroelectric was finally settled based on the hysteresis loop measured by Teague et al. [29] They performed the experiment in liquid nitrogen, which lowered the charge carrier density and mobility, and in turn lowered the leakage current. The measured spontaneous polarization was $3.5\mu C/cm^2$ along the <100> direction, which represents $6.1\mu C/cm^2$ in the <111>direction.

This value is much smaller than what would be expected for a ferroelectric material with such high Curie temperature and large distortion. The leakage problem, likely due to defects and non-stoichiometry, has been hampering more comprehensive studies about the bulk BiFeO$_3$ and has limited applications of this material. To overcome this problem, recent work has focused on solid solutions of BiFeO$_3$ with other ABO$_3$ materials, such as BaTiO$_3$, which can prevent second phase formation and increase sample resistivity. For example, Ueda et al. have reported a remnant polarization of $2.5\mu C/cm^2$ from $(Bi_{0.7}Ba_{0.3})(Fe_{0.7}Ti_{0.3})O_3$ film. [30] BiFeO$_3$ ceramic bulk and films with high resistivity have also been studied. [31,32] Nevertheless, the reported polarization values were mostly less than $10\mu C/cm^2$.
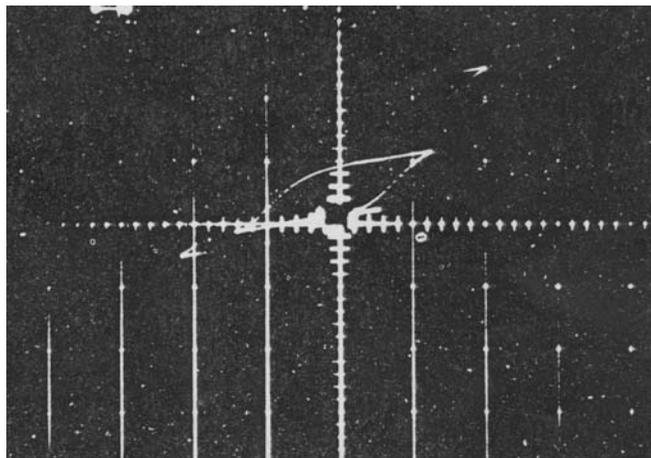
Figure 1. 9 Dielectric Hysteresis loops obtained on a single crystal of $BiFeO_3$ in liquid nitrogen. The maximum field applied was 55kV/cm, and the spontaneous polarization was $3.5\mu C/cm^2$. Figure adopted from Teague et al. [29]

### 1.3.3 Magnetic properties

Magnetic properties of bulk $BiFeO_3$ have been studied for many years. Sosnowska et al reported the unusual magnetic spiral arrangement in $BiFeO_3$. [33,34] Basically, $BiFeO_3$ has G-type antiferromagnetic configuration, where each $Fe^{3+}$ is surrounded by six antiparallel nearest neighbors. [35] But original neutron study did not have the resolution to obtain information on the exact spin orientation. Later, Sosnowska et al. performed high-resolution time-of-flight (TOF) diffractometer studies on a $BiFeO_3$ powder sample.

Their main observations can be summarized as following: (i) At the wavelength where one expects purely magnetic scattering (101, 105, 107, 205 reflections), no sharp lines but only broadened patterns were observed. (ii) At the (113) and (211) peak positions where nuclear and magnetic scattering are superposed, the magnetic contributions can be seen at the base of the nuclear Bragg reflections.

These observations can not be explained based on a simple G-type antiferromagnetic structure as indicated by original neutron studies. Sosnowska et al first excluded contributions from other phases and system error. They also confirmed the magnetic origin of these broadened patterns by their disappearance at temperatures above the Neel temperature of $BiFeO_3$.

To explain the observed patterns, Sosnowska et al proposed a modified G-type antiferromagnetic structure where the spin of $Fe^{3+}$ is subjected to a long-range modulation. Theoretical model was established, and it was concluded that (1) spins in $BiFeO_3$ were modulated into a cycloidal spiral with a long period of 620±20 Å. (2) the spiral direction q lies in the hexagonal base plane and can vary its direction within the base plane. A schematic picture of the spin rotation and spiral direction is shown in Figure 1.11. Details of the analysis can be found the reference. [33]
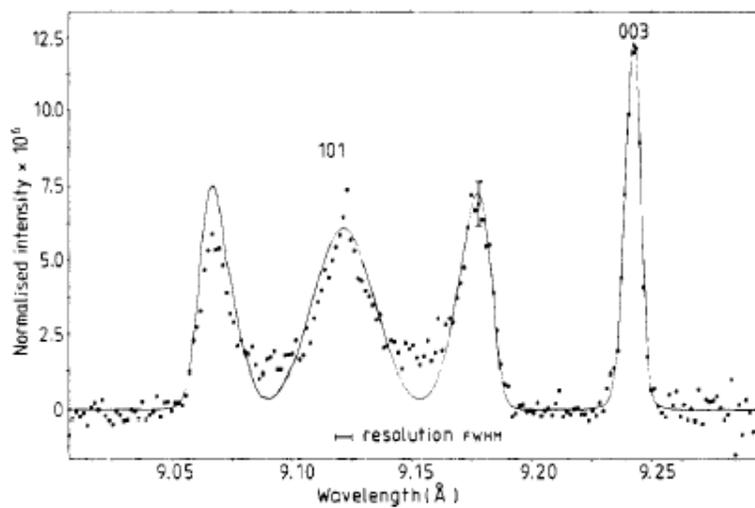
Figure 1. 10 Normalized TOF spectrum from BiFeO$_3$ power sample at about 9.2 Å. The full curve represents the spectrum calculated from the proposed model of spin configuration. Figure adapted from Sosnowska et al. [33]
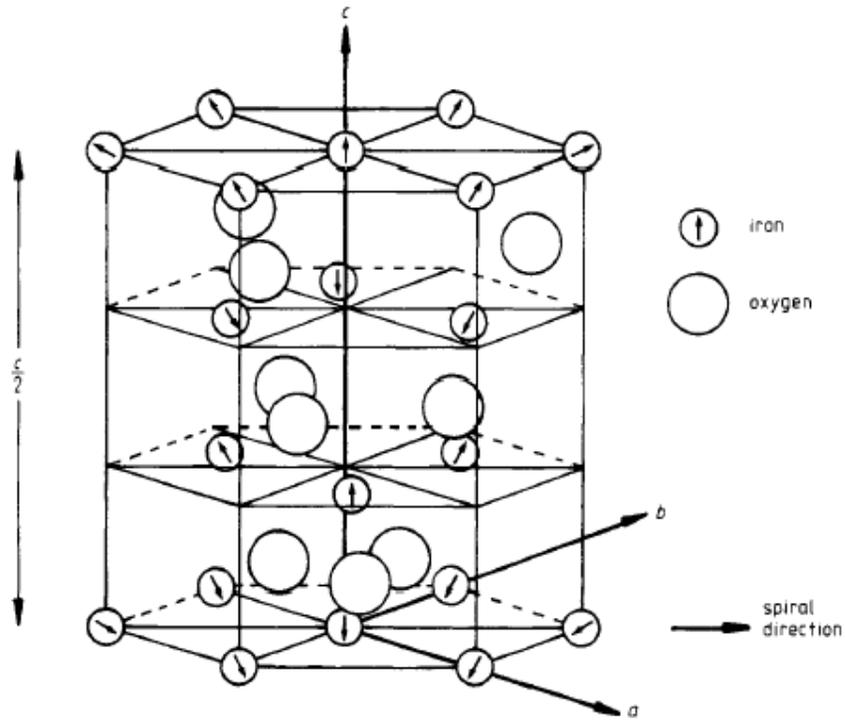
Figure 1. 11 Portion of $BiFeO_3$ lattice. The arrows indicate the $Fe^{3+}$ moment direction of the proposed model. The spiral period is reduced for illustration purpose. Figure adapted from Sosnowska et al. [33]

# CHAPTER 2, PURPOSE OF RESEARCH

$BiFeO_3$ has been the subject of numerous investigations since its discovery in the 1950s. Due to its simple perovskite structure, $BiFeO_3$ is a model material system for investigating the nature of interactions between structural, electrical and magnetic order parameters. It is expected to have large polarization and piezoelectric coefficients because of its high Curie temperature and large distortion: but this has previously not been observed. It should have a noticeable saturation magnetization due to spin canting: but has only been observed in single crystal under ultra high magnetic field. Furthermore, the coexisting ferroelectric and antiferromagnetic order parameters offer an additional degree of freedom, via the magnetoelectric (ME) exchange. However, the ME exchange interaction remains a myth in $BiFeO_3$.

The controversies concerning $BiFeO_3$ can be summarized as follows

(1)  Due to the samples' high conductivity, electrical characterization of bulk signal crystal/ceramics has been difficult. Teague et al. reported the first dielectric hysteresis loop and the spontaneous polarization was $\sim 3.1 \mu C/cm^2$. The experiment was performed in liquid nitrogen. But, as noted by the authors, this value is much smaller than what would be expected for a ferroelectric material with such a high Curie temperature and large distortion. Later, scientists tried to mix other $ABO_3$ materials into $BiFeO_3$ forming solid solutions; this helps to increase the sample resistivity. Ueda [30] et al reported a Pr of $\sim 2.5 \mu C/cm^2$ from $BiFeO_3/BaTiO_3$ thin films. More recently, $BiFeO_3$ thin films with high resistivity have also been made. [ 36 ] Nevertheless, the reported spontaneous polarizations before this study are small.

(2)    Early neutron diffraction study revealed a G-type antiferromagnetic spin

order for $BiFeO_3$ with a small canting between neighboring antiparallel $Fe^{3+}$

ions. [37] It was concluded that $BiFeO_3$ should show weak ferromagnetic

property at room temperature. But no such behavior has been reported. Later,

Sosnowska [38,39] reported that the antiferromagnetic order of $BiFeO_3$ is

subjected to a spiral modulation that cancels out the net magnetization. By

breaking this cycloidal structure, one could release the magnetization due to

canting. [40,41]

This thesis is the first study of epitaxial thin films of $BiFeO_3$. In the course of this

work, we have begun to resolve some of these controversies that have plagued $BiFeO_3$.

Again, our findings concentrate on epitaxial thin-layer form of the material. The

roadmap steps or milestones of the work have been as following:

(i)    Optimization of the pulse laser deposition parameters for $BiFeO_3$ thin films.

In Chapter 3, deposition and characterization tools used in this study are introduced.

Basic operating principles are presented. Deposition parameters for $BiFeO_3$ thin films

as used in this study are introduced.

(ii)    Characterize the structure of $BiFeO_3$ films. Investigate the effects of

substrate orientation and film thickness on its structure.

Chapter 4 covers the structure analysis using X-ray diffraction (XRD) and

transmission electron microscopy (TEM). Room temperature XRD shows the films

grown on (111) cut $SrTiO_3$ substrate have a rhombohedral structure, identical to that

of a single crystal, whereas films grown on (001) and (101) substrates are

monoclinically distorted due to the epitaxial constraint, since $SrTiO_3$ has a smaller

lattice constant. Mesh-scans were performed to identify domain structures in the film. The BiFeO$_3$(111) films are found to be in a single domain state. On the other hand, (001) and (101) films both show domain splitting with two variants populated.

(iii) Study the electrical properties of BiFeO$_3$ films along different crystallographic directions.

Electrical properties of BiFeO$_3$ films along different crystallographic directions are presented in Chapter 5. It was found that the BiFeO$_3$ (111) films have a spontaneous polarization as large as $\sim$95$\mu$C/cm$^2$. This is 10x larger than previously reported result and is close to the expected value based on structural distortion. (001) and (101) oriented films show Ps of $\sim$55$\mu$C/cm$^2$ and $\sim$75$\mu$C/cm$^2$ respectively. Simple calculation shows that these values are very close to the projections of Ps(111) as

$$\sqrt{3}P_{(001)} = \frac{\sqrt{6}}{3}P_{(101)} = P_{(111)}.$$ A piezoelectric coefficient as large as 70pm/V was observed for 200nm BiFeO$_3$ (001) film, promising for applications in Micro-Electro-Mechanical Systems (MEMS), actuators and transducers. Strain effect on these properties was also investigated by varying film thickness.

(iv) Study the magnetic properties of BiFeO$_3$ in thin films form. Shed light on the coupling between polarization and magnetization in BiFeO$_3$.

Chapter 6 presents the magnetic properties of BiFeO$_3$ thin films. It was reported very recently that the cycloidal antiferromagnetic structure in BiFeO$_3$ single crystal can be destroyed by a large external field (>25T), thus releasing the net moment due to spin canting. Our results show that BiFeO$_3$ thin films show weak ferromagnetism at room temperature under a small field. This could be attributed to the destruction of the

cycloidal structure by epitaxial constraint or size effect. Thickness dependence of magnetization supported this conjecture. Larger moments were observed in thinner films since strain relaxes over thickness. Comparisons between samples with different orientations, between thin films, ceramics and single crystals provide more insight into the intrinsic magnetic property of $BiFeO_3$. Attempts to study the coupling between electric and magnetic order parameters in $BiFeO_3$ thin films are also covered.

    (v)    Studies towards integration of $BiFeO_3$ on Si.

One of the reasons that people are interested in $BiFeO_3$ is that it could be an alternate for the most widely used ferro/piezoelectric PZT system, which has toxic Pb. From this point of view, it is very important to integrate $BiFeO_3$ with the well-developed Si industry. In chapter 7, I present my work on depositing and characterizing epitaxial $BiFeO_3$ thin films on Si substrate. Pre-deposited $SrTiO_3$ layer is used as a template. Structural and electrical properties of these films are characterized and compared with films grown directly on $SrTiO_3$. It was found that thermal mismatch between Si substrate and $BiFeO_3$ dominates during the cooling process and induces smaller out-of-plane lattice parameter. XRD analysis reveals different domain features. Large piezoelectric coefficient of ~120pm/V was observed for 200nm films.

# CHAPTER 3, DEPOSITION AND CHARACTERIZATION

# OF BiFeO$_3$ THIN FILMS

Pulsed laser deposition (PLD) has been used to deposit BiFeO$_3$ thin films. X-ray diffraction (XRD) and transmission electron microscopy (TEM) were used to characterize the structure. The electrical properties of the films were measured using a commercially available Radiant Technology (RT6000) system. The magnetic properties were measured using both a vibrating sample magnetometer (VSM) and a superconductive quantum interference device (SQUID).

## 3.1 Pulsed Laser Deposition of BiFeO$_3$ thin films

### 3.1.1 Introduction to Pulsed Laser Deposition

Figure 3.1 shows a schematic diagram of a basic PLD system. During the deposition process, a pulsed laser beam (typically 30ns pulses with energy in the range of 0.1-1 J and a frequency of 1-30Hz) is focused onto the target in a vacuum chamber. Lasers that are commonly used include ArF, KrF excimer lasers, and Nd:YAG laser. It is generally recognized [42] that the shorter the wavelength, the more effective the ablation. Accordingly, excimer lasers have become the standard ones. When the laser energy density (energy per unit area at the target surface) is above a threshold value, the target (bulk ceramic or crystal) is evaporated, forming a plasma plume. The plume is normal to the target surface and collected on a suitably positioned and heated substrate. Deposition parameters have to be optimized to achieve high quality epitaxial films. These include substrate temperature, laser energy density and frequency, target-to-substrate distance, base pressure and deposition gas pressure, etc. During oxide deposition, oxygen must be introduced into the chamber in

order to assisting the formation of the desired phase and film composition.

There are a number of advantages of PLD over other film deposition methods, these include

(i) versatility- its biggest advantage. A very wide range of materials, including oxides, metals, semiconductors and even polymers, can be grown by PLD. All that is required is a target of the desired composition. It is unlike Molecular Beam Epitaxy (MBE) and Chemical Vapor Deposition (CVD), where different sources of precursors are required for each element of the desired compound.

(ii) its ability to maintain target composition in the deposited thin films. Because of the very short duration and high energy of the laser pulse, target material plumes instantly toward the substrate: every component of the phase has a similar deposition rate. This makes optimization of the deposition process much easier.

(iii) the energy associated with the high ionic content in laser ablation plumes (typically of the order of 10% and rising with increasing incident laser power density) and high particle velocities (of the order of $10^6$ cm.s$^{-1}$) appear to aid crystal growth and lower the substrate temperature required for epitaxy.

(iv) the fact that PLD is clean, low cost, and capable of producing heterostructures simply by switching between several different targets.

There are also a number of disadvantages of PLD, which limit the method to

fabrication of new material systems under research environments. These include:

(i)   a small plume cross sectional area of the order of $cm^2$, due to a limited laser spot size. This, in turn, limits the sample size that can be prepared by PLD. In addition, it also brings difficulty to controlling thickness uniformity across the sample: This problem can be overcome, to some extent, by scanning the laser beam on a larger size target.

(ii)  the plume of ablated materials is highly forward directed, which causes poor conformal step coverage. It also makes thickness monitoring difficult.

(iii) Finally, there is an intrinsic "splashing" associated with laser ablation itself, which produces droplets or big particles of the target material on the substrate surface. From an industrial perspective, this is particularly serious as it will result in device failure.
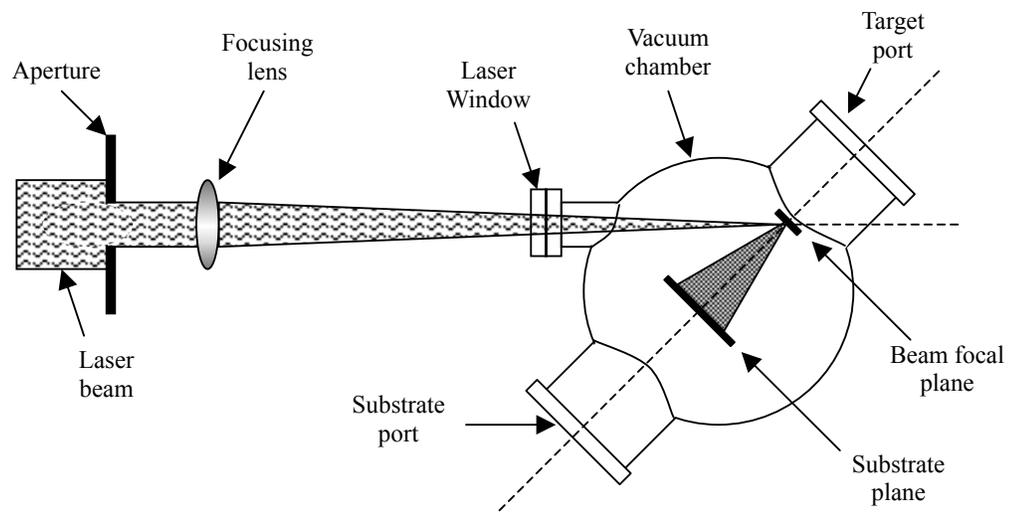
Figure 3. 1 Schematic illustration of a Pulsed Laser Deposition system

**3.1.2 Pulsed Laser deposition of BiFeO$_3$ thin films**

Typical oxide depositions by PLD are done according to the following steps:

(i)     Substrate cleaning and target preparation.

Before deposition, the substrates have to be cleaned thoroughly to remove the organic and inorganic residuals on the surface due to polishing. A three steps ultrasonic cleaning process is common practice, as used in this thesis. The substrate is soaked for two minutes in tricloroethylene (TCE), acetone and isopropanol with ultrasonic agitation successively. The targets surface must be polished with fine sandpaper before deposition. This helps to remove the laser burned layer formed during previous deposition, which may have different composition.

(ii)     Setting up and pre-pump the chamber.

Once the substrate and target are ready, they can be put into the deposition chamber, which will then be pumped to a base pressure of $<10^{-5}$ Torr. The pumping valve is then closed with a very small leak left and the oxygen flow rate is adjusted to maintain a dynamic pressure of 100mTorr during substrate heating. The heating rate is typically 20$^o$C/min. Before the deposition, laser energy and frequency are adjusted to the desired values. Once deposition is finished, the valve leak is closed and ambient pressure oxygen is introduced into the chamber while the substrate remains at its deposition temperature. It is then cooled down to room temperature at 5$^o$C/min.

(iii)     Substrate heating, oxygen pressure adjustment, laser energy calibration
        and deposition.

We used KrF excimer laser with 248nm wavelength. The laser energy was ~400mJ,

while the energy at the target surface is ~30mJ. The target-substrate distance is ~6cm. Stoichiometric $BiFeO_3$ and $SrRuO_3$ targets were used. During the substrate heating, oxygen was introduced into the chamber; a dynamic partial pressure of 100mTorr was maintained. Details of the deposition parameters are listed in Table 3.1. We note that the oxygen partial pressure suitable for deposition of highly resistive perovskite $BiFeO_3$ thin films, 20mTorr, is much lower than typical values for perovskite oxides (~100mTorr).

   (iv)    Post-deposition annealing in oxygen.

After deposition, the chamber was filled with oxygen (1atm) and the films were cooled down at $5^oC$/min. For $SrRuO_3$, it is cooled directly to room temperature, while after $BiFeO_3$ deposition, it was cooled to $390^oC$, annealed for 1 hour and then to room temperature.

Table 3. 1 Deposition parameters used in this study

|  | Substrate temperature | $O_2$ partial pressure | Energy density | Post-deposition annealing | Laser Rep rate | Deposition rate |
|---|---|---|---|---|---|---|
| SRO | 650°C | 100mTorr | ~1.2J/cm$^2$ | no | 3Hz | ~0.7nm/min |
| BFO | 670°C | 20mTorr | ~1.2J/cm$^2$ | $390^oC$, 1hr | 20Hz | ~5nm/min |

**3.2 Characterization tools**

**3.2.1 Structure analysis: XRD, TEM**

In 1912, Bragg recognized that x-ray diffraction in crystals obeys particular geometric restriction related to inter-planar crystal spacings. Later, this relationship was designated as Bragg's Law that states $n\lambda = 2d \sin\theta$; where $\lambda$ is the x-ray

wavelength, d is the crystal plane spacing, and $\theta$ is the x-ray incident angle. This forms the basis for the interpretation of XRD results. The XRD system used in this thesis was an X'pert PRO (Philips Inc.), which is the basic platform for a wide variety of applications in analytical x-ray diffraction. This system was used in my thesis to perform (i) high-resolution lattice parameter measurements, both at room temperature and as a function of temperature up to $600^{o}C$, and (ii) $\omega$-$2\theta$ scans to characterize the elastic domain structures of our films. These results will be covered in Chapter 4.

XRD can be used to distinguish multiple equivalent directions, such as elastic domain variants. The idea behind elastic domain analysis is shown schematically in Figure 3.2. Suppose we have two sets of planes with the same inter-plane spacing that have different directions. These related planes can be accessed together by a mesh or $\omega$-$2\theta$ scan, where at different $2\theta$ values, the diffraction condition is rocked about $\omega$. When the incident and reflected x-ray are at positions 1 and 2 respectively, $2\theta$ is the Brag angle and $\omega$ is the angle between incident x-ray and sample surface, we observe the peak, which we can designate as the first domain. As both the values of $2\theta$ and $\omega$ are varied, additional domains will be revealed.

Transmission electron microscopy studies were performed in this thesis using a JEOL 4000FX, which operated at 300 kV. Lattice parameters were calculated from electron diffraction patterns. In addition, high-resolution images were examined for defects at the interfaces and inside the films. For details of TEM operation and analysis, the reader is referred to references [43,44].
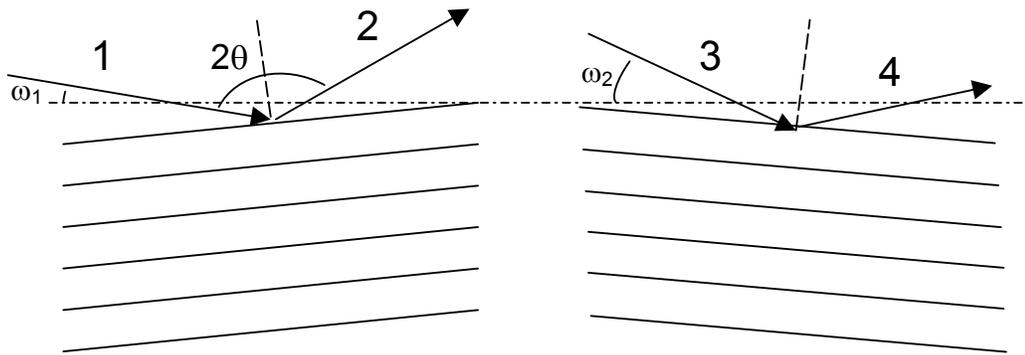
Figure 3. 2 Schematic illustrations showing how the XRD system detects domain structure.

### 3.2.2 Electric measurements: RT6000, PFM

The ferroelectric properties (including hysteresis loop, pulsed polarization, polarization retention and fatigue, and resistivity) were measured using a commercially available Radiant Technology Precision 6000 system. The dielectric constant was measured using a HP impedance analyzer.

A standard photolithography technique was used to define a pattern upon which to make small capacitors. First, photoresist was spin coated onto the surface of the sample, which was then baked at 110°C for 10 minutes. The next step was to align the selected mask pattern with the sample and expose it to UV radiation for crosslinking. After developing, the right pattern for the top Pt-electrode was achieved. The final structure (after Pt deposition and lift-off) is shown in Figure 3.3. Since the big capacitor has a much larger capacitance, the voltage can be treated as though it has been applied solely to the small capacitor. The polarization was then determined by integrating the current flow,

$$P = \frac{Q}{A} = \frac{1}{A}\int I dt,$$

where A is the small capacitor area. The same setup was used for other electrical characterizations such as leakage, pulsed polarization and dielectric constant measurements.

Piezoelectric analysis, both $d_{33}$ measurement and domain imaging, were performed using a scanning force microscope (SFM). This technique has been used to characterize PZT thin films by several groups. [45,46,47] It is based on the detection of the vibration of a ferroelectric sample, which is induced by an external ac voltage. Figure 3.4 demonstrates the set up of this technique; the signal from lock-in amplifier can be displayed quantitatively ($d_{33}$) or qualitatively (domain imaging). An external voltage with a frequency $\omega$ was applied through the tip, which causes the sample area
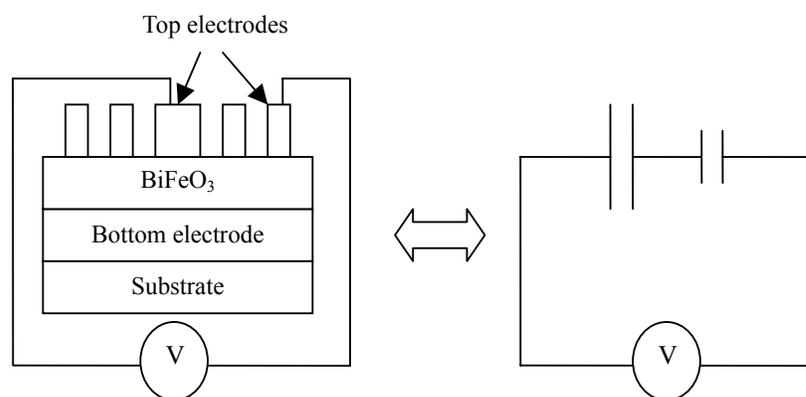
Figure 3. 3 Schematic structure and equivalent circuit of the electrical measurements setup.

under the electric field to vibrate at the same frequency due to the converse piezoelectric effect. This vibration then forces the SFM tip to oscillate, and the modulated deflection signal is detected using the lock-in amplifier.

In the imaging mode, the conducting tip is in direct contact with the sample surface. The electric field underneath the tip measures local domain orientation information. By scanning along the sample surface, the domain configuration of the sample can be mapped out. The resolution of the domain features depends on the sharpness of the tip.

In the quantitative (or $d_{33}$) mode, the voltage is applied through the tip to a capacitor with a Pt top electrode. This ensures a homogenous electric field under the electrode; it also prevents the build up of electrostatic interaction between the cantilever and the sample. Care was taken such that the frequency of the applied voltage was far lower than the cantilever resonant frequency: this was done to avoid mechanical resonance of the cantilever. We used standard silicon tips, which were coated with a Pt/Ir alloy for electrical conduction. The typical force constant of these tips was 5 N/m, and the resonance frequency (as specified by the manufacturer) was 60-80KHz. The contact force was ~ 70 to 100 nN. The measurement frequency used was 6.39 KHz. Each capacitor was driven at particular DC voltage to study the field dependence.

To calibrate the output signal from the photodiode, we used x-cut quartz crystal coated with top and bottom Au electrodes. The quartz was driven from 0 to 10 Volts and the displacement of the tip was recorded, as illustrated in Figure 3.5. The slope of the linear displacement vs. voltage plot is equal to $d_{33}$ of quartz, i.e., 2.3 pm/V. [48] We compared this calibration method to a different technique used by Harnegea et al., [49] who calibrate the output of the photodiode with the slope of the AFM force

$$\Delta z(t) = \int_{0}^{h_F} d_{33} E(z, t) dz$$
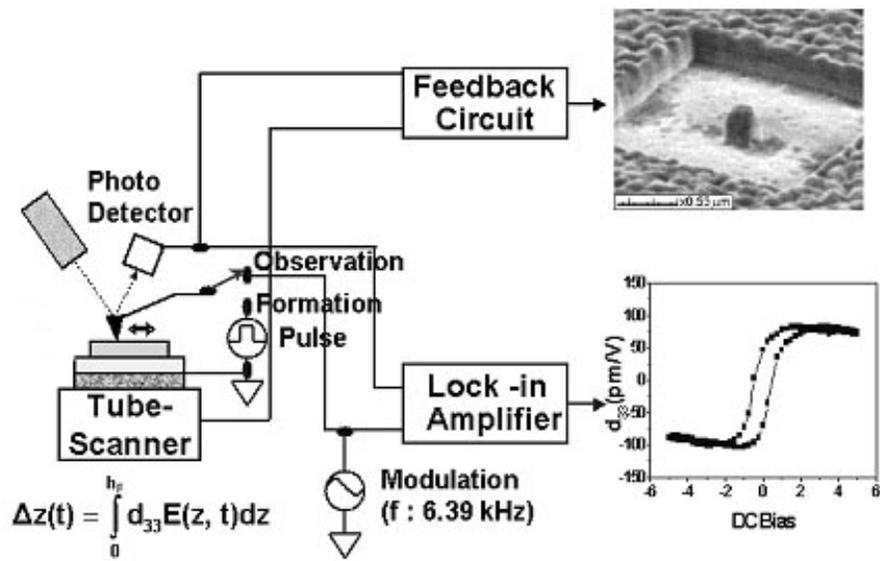
Figure 3. 4 Schematic illustration of the PFM setup
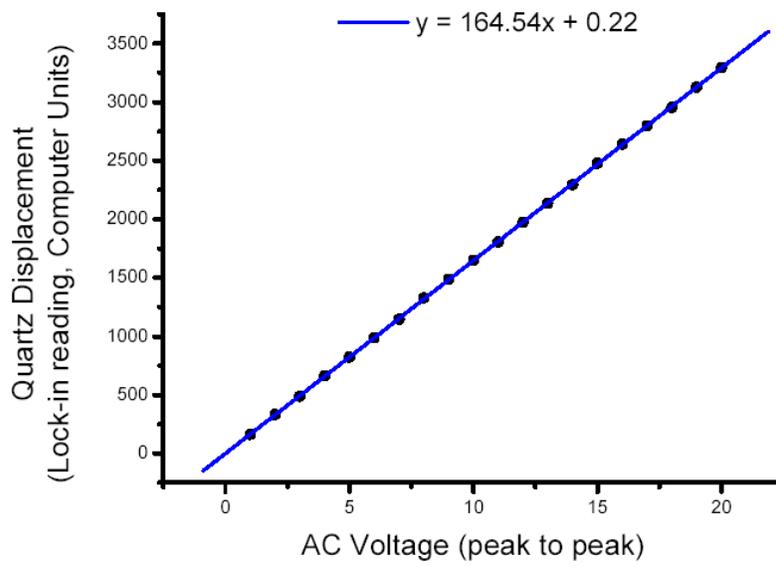
Figure 3. 5 Calibration of piezoelectric response

curve. Our results were in good agreement for both approaches. For each measurement, care was taken to keep the AC voltage constant, as it has been reported that increasing AC amplitude can result in an increase in the effective $d_{33}$. [50]

### 3.2.3 Magnetic analysis

Magnetic analyses of the $BiFeO_3$ thin films were done using a vibrating sample magnetometer (VSM), and a superconductive quantum interference device (SQUID). The M-H hysteresis loop, the temperature dependence of the saturation magnetization and the AC magnetic susceptibility were all characterized using these instruments.

The VSM method is based on Faraday's law, which states that an emf will be generated in a coil when there is a change in the flux going through the coil. For a coil with n turns of cross-sectional area a, the emf (V) is related to $\dfrac{dB}{dt}$, given as

$$V = -na\frac{dB}{dt}.$$

Since $\Delta B = \mu_0 M$, when we place a magnetic sample into the coil, this relationship becomes $V = -na\mu_0 M / dt$.

A typical VSM setup is illustrated in Figure 3.6. It has a pair of electromagnets that generate a DC magnetic field, and a pick-up coil that acquires the sample signals. When a sample has a net magnetization, it produces magnetic flux in its vicinity. During VSM measurements, the sample is mechanically vibrated (up and down) at a fixed frequency (generally 82Hz). This vibration produces a flux change, which generates an AC voltage proportional to the magnetic moment of the sample in the pick-up coil. A lock-in amplifier is then used to measure the voltage. The AC signal picked up by the coil is proportional to the frequency and amplitude of the sinusoidal motion and the total magnetic moment of the sample at that applied magnetic field.
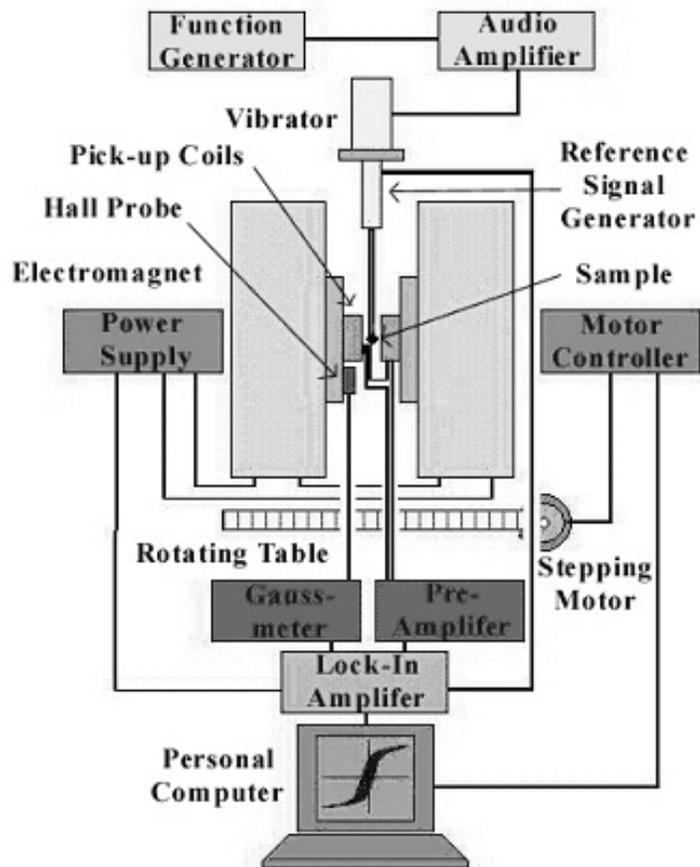
Figure 3. 6 Schematic diagram of VSM.

The frequency and amplitude of the sinusoidal motion are held constant, which is controlled by a capacitor (reference signal generator). By feeding the signals from the pick-up coils and the reference signal into a demodulator, the magnetic moment of the sample is extracted. The magnetic moment determined by VSM is given in terms of the basic electromagnetic unit (or, emu), which can be related to the magnetization, susceptibility, and Bohr magnetron. VSM provides a fast and easy way for measuring the magnetic properties of materials. However, it does have a few drawbacks. These include (i) the resolution of VSM is $\sim10^{-5}$ emu, which is insufficient for thin film samples or sample with low intrinsic magnetization, i.e., canted antiferromagnetic or ferrimagnetic materials; and (ii) most VSMs do not have low temperature capability.

A SQUID with a magnetic field resolution of $10^{-15}$ Tesla is the most sensitive device for detecting magnetic flux. It uses the properties of superconducting electron-pair wave coherence and Josephson junctions to detect very small magnetic fields.

In superconductors, current is carried by pairs of electrons, known as Cooper Pairs. Each pair can be treated as a single particle with a mass and charge twice that of a single electron. Unlike in normal conductor where electrons get scattered and have short wavelength, the superconductive electron pairs are not scattered, hence their wavefunctions are coherent over long distances. Each pair can be represented by a wavefunction of the form $\varphi = \varphi_0 e^{i(P\bullet r)/\hbar}$, where $\vec{p}$ is the net momentum of the pair whose center of mass is at $\vec{r}$. In a uniform current density all the electron wavelengths are equal. The superposition of these coherent waves produces a single wave of the same wavelength; thus all of the electron pairs in a superconductor can be described by a single wavefunction $\psi = \psi_0 e^{i(P\bullet r)/\hbar}$ or $\psi = \psi_0 \sin 2\pi(\frac{x}{\lambda} - \upsilon t)$. The

long coherent wave of superconductive electron pairs also requires that if a superconductive current passes through a ring, that the total phase has to be $n2\pi$, thus no point can have two different phases.

Two superconductors separated by a weak link is called a Josephson junction. When the layer is thin enough, electron pairs can actually tunnel through the barrier forming the supercurrent. This current is related to the critical current, $i_c$, by $i_s = i_c \sin \Delta\Phi$, where $\Delta\Phi$ is the phase difference across the link.

SQUIDs generally use two Josephson junctions, as illustrated in Figure 3.10, which form a ring with weak-links (generally thin insulating layers) at points W and X. The ring must be kept at superconductive state. A current is divided evenly between the two junctions when there is no magnetic field, and the phase difference across the two junctions ($\alpha$ and $\beta$) are the same. But when a magnetic field is applied, $\alpha$ and $\beta$ are no longer equal, but their sum remains constant. Now that along the ring,

$$\alpha + \beta + 2\pi \frac{\phi_a}{\phi_0} = n2\pi \quad \text{must be satisfied, where } 2\pi \frac{\phi_a}{\phi_0} \text{ is the phase change due}$$

to the applied magnetic field and $\phi_0 = \dfrac{\hbar}{2e} = 2.07 \times 10^{-15} Wb$ is called the floxon. The

values of $\alpha$ and $\beta$ can be written as $\alpha = \pi[n - (\frac{\phi_a}{\phi_0})] - \delta$, and $\beta = \pi[n - (\frac{\phi_a}{\phi_0})] + \delta$.

The total current from Y to Z is then given as

$$I = I_X + I_W = i_C \sin\alpha + i_C \sin\beta,$$

$$\text{or} \quad I = 2i_C \left| \cos\pi \frac{\phi_a}{\phi_0} \cdot \sin\delta \right|.$$

As $\sin\delta \leq 1$, we can obtain the critical measuring current as

$$I_C = 2i_C \left| \cos\pi \frac{\phi_a}{\phi_0} \right|.$$
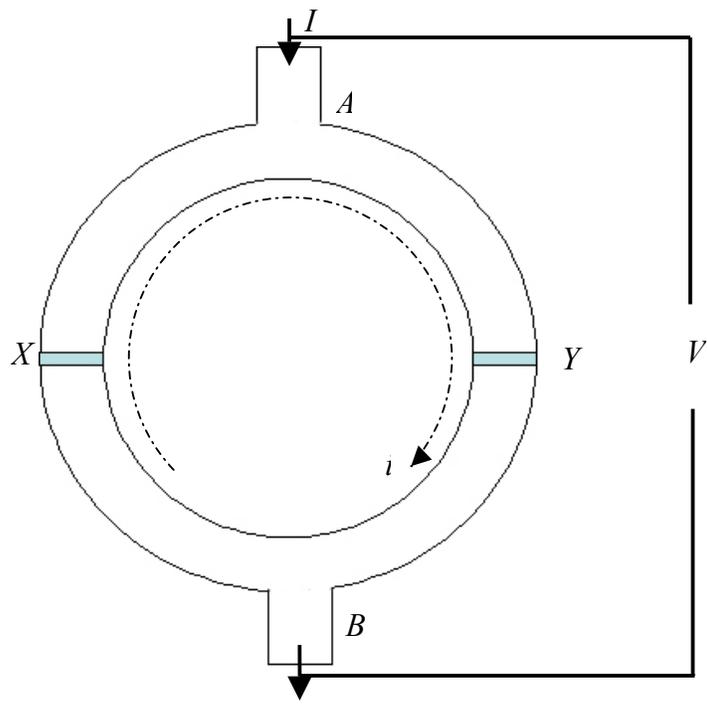
Figure 3. 7 Current flow in a SQUID coil.

This relationship gives a periodic dependence on the magnitude of the magnetic field. A maximum value occurs when the field is an integer number of fluxons, and a minimum value occurs at half integer values.

A set of superconducting sensing loops is arranged in a configuration that only detects the magnetic flux from the magnetization of the sample (expels the uniform field applied to the sample by the superconducting magnet). The superconducting loops are detection gradiometer coils, which are accurately balanced. As a sample moves through the coils, the magnetic moment of the sample induces an electric current in the detection coils. Since the coils, the connecting wires and the SQUID input coil form a closed superconducting loop, this current is not damped and any change in magnetic flux in the detection coils produces a proportional change in the persistent current in the detection circuit.

# CHAPTER 4, STRUCTURAL ANALYSIS OF (001), (101) AND (111) BiFeO$_3$ THIN FILMS

In this chapter, structural characterization results of BiFeO$_3$ films grown on (100), (110) and (111) oriented single crystal SrTiO$_3$ substrates are presented. A pseudo-cubic index will be used throughout the chapter unless otherwise specified. SrTiO$_3$ has a cubic structure with a lattice parameter of a=3.905 Å at room temperature. Films both with and without an intermediate SrRuO$_3$ electrode layer were studied. SrRuO$_3$ has orthorhombic structure of space group Pbnm with a=5.5670 (1)Å, b=5.5304(1)Å and c=7.8446 (2)Å. [51] It can be treated as cubic with a~3.94 Å. [52] To study the effect of lattice mismatch (i.e. epitaxial strain), the BiFeO$_3$ and SrRuO$_3$ films thickness were varied between 30-600nm, and 10-50nm, respectively.

## 4.1 Strain effect in epitaxial thin films

It is well established that the mismatch strain between the film and substrate plays an important role on the structure and properties of epitaxial thin films. Numerous studies have been conducted in this area, both experimentally and theoretically [53,54,55,56,57,58]. Generally, as the film thickness is increased, the excess elastic energy is relaxed by lattice deformation, dislocations and elastic domain formation.

During deposition, films initially grow coherently on a substrate. In the case of heteroepitaxial growth, the substrate and the film usually have different lattice constant, but similar/same structure type (i.e. for example, perovskite on perovskite). The film deforms to accommodate to the lattice of the substrate. Above a critical thickness (h$_c$), the creation of misfit dislocations is energetically favored to release the excess elastic strain energy. For a specific substrate/film couple, this critical thickness

can be given as

$$h_c = \frac{b}{8\pi f(1+\nu)}\left[\ln\left(\frac{h_c}{b}\right)+1\right];$$

where f is elastic constant of the film, $\nu$ is Poison ratio of the film, and $b = \frac{a_f - a_s}{a_s}$ is the lattice mismatch between the film and substrate. Assuming that there are no additional dislocations which form during cooling of the film from the growth temperature ($T_G$), the relaxation of lattice parameter of the film can be taken into account by using an effective substrate lattice parameter, given as [59,60]

$$\bar{a}_s(T) = \frac{a_s(T)}{\rho(T_G)a_s(T)+1},$$

$$\rho(T_G) \approx \frac{\varepsilon(T_G)}{a_0(T_G)}\left(1-\frac{h_c}{h}\right);$$

where $\rho(T_G)$ is the equilibrium linear dislocation density at the deposition temperature, $\varepsilon(T_G)$ is the misfit strain at $T_G$, $a_0(T_G)$ is the substrate lattice constant at the growth temperature, h is the film thickness, and again, $h_c$ is the critical thickness for dislocation generation below which dislocation formation is not feasible. Since the density of dislocations depends on the ratio $\frac{h_c}{h}$, it is obvious that the degree of relief provided by dislocations also increases as the film thickness increases.

Poly-domain formation is another stress release mechanism. However, it can only occur in systems that undergo a structural phase transition. For perovskite ferroelectric epitaxial thin films, the lattice mismatch with various substrates is known to create a driving force for the formation of a domain (twin) structure at temperature below Tc. Twinning in ferroelectric thin films has been theoretically predicated using a continuum approach by Roitburd in 1976.
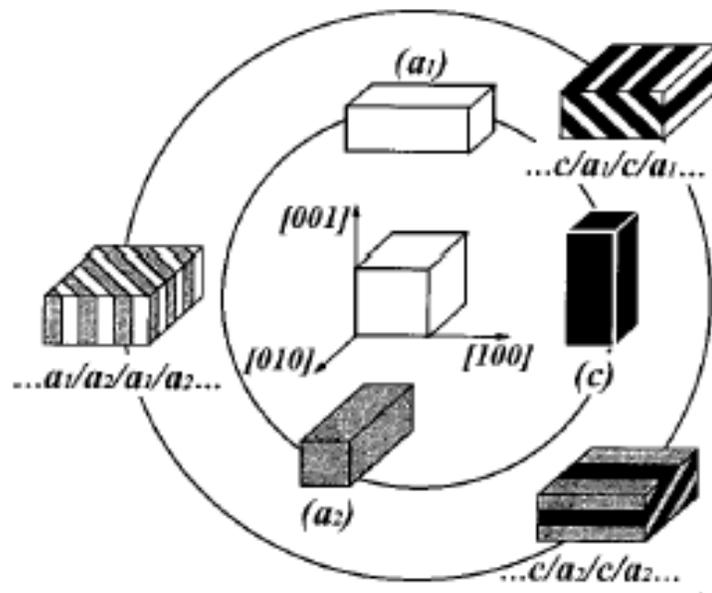
Figure 4. 1 Orientational variants of the ferroelectric phase (inner circle) and possible polydomain structures (outer circle) due to a cubic-tetragonal transformation. Figure adapted from Nagarajan et al. [82]

During the last several decades, the domain patterns of $PbTiO_3$, $Pb(Zr_xTi_{1-x})O_3$, $BaTiO_3$ and $KNbO_3$ epitaxial thin films grown on various substrates have been studied. As an illustration, Figure 4.1 shows all possible orientation variants of the ferroelectric phase (inner circle) and possible poly-domain structures (outer circle) due to cubic-tetragonal transformation.

Epitaxial strain can dramatically change the film structure and properties. For example, Burke and Pressley [61,62] have shown that a [111] stress greater than 26.5 $kg/mm^2$ produces a change in the crystal field of $SrTiO_3$ from a tetragonal to a trigonal one. In addition, upon the application of a <100> or <110> uniaxial stress at 4.2°K in $SrTiO_3$, they observed a spontaneous polarization and a maximum in the dielectric constant. The critical stress for the transition to the ferroelectric phase was estimated as 10.1 $kg/mm^2$ along <100> and 53 $kg/mm^2$ along <110>. Later, Hiromoto, Uwe, and Tunetaro reported similar results. [63]

More recently, Pertsev et al [64] developed a thermodynamic theory for $SrTiO_3$ epitaxial thin films. The misfit strain-temperature phase diagram of (001)-oriented single-domain $SrTiO_3$ films grown on cubic substrates was constructed. It was found, except over a narrow range of small negative misfit strains, that the ferroelectric phase transition should take place in $SrTiO_3$ films at a finite temperature. By calculating all minima of the free energy, F(P, q , Sm, T), with respect to the components of the polarization and structural order parameters, and then by selecting the most energetically favorable phase, they determined the equilibrium single-domain thermodynamic states of $SrTiO_3$ films under various strain-temperature conditions. It was found, besides the high temperature tetragonal (HT) phase being a distorted prototypic cubic phase, that only states with their polarization P and/or order parameter q directed along the edges of the prototypic cubic cell were stable in $SrTiO_3$

films. They include purely ''structural'' tetragonal and orthorhombic states (denoted as ST and SO), purely ferroelectric tetragonal and orthorhombic phases ($FT_I$ and $FO_I$), and three ''mixed'' states ($FT_{II}$, $FO_{II}$, and $FO_{III}$), where both P and q were non-zero. The phase diagram showing the stability ranges of these states is given in Figure 4.2. The most interesting feature of their predicted phase diagram is the presence of two wide misfit strain-temperature ranges, in which $SrTiO_3$ becomes a true ferroelectric material. This phenomenon is due to the coupling between polarization and strain (electrostriction), which favors the formation of a ferroelectric phase with an out-of-plane polarization in films grown on ''compressive'' substrates (Sm ,0), or with an in-plane polarization in the case of films grown on ''tensile'' substrates (Sm.0). In addition, the ''paraelectric gap,'' which separates the stability ranges of the aforementioned ferroelectric states, narrows rapidly with decreasing temperature.
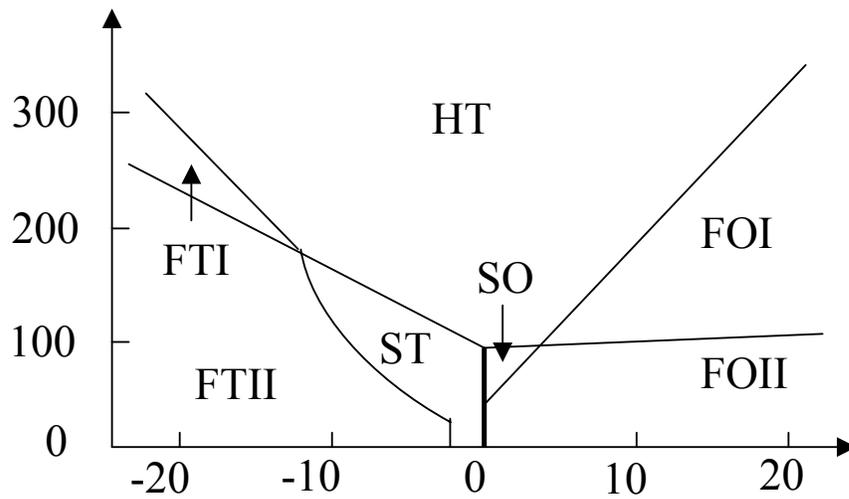
Figure 4.2 Phase diagram of (001)-oriented single domain $SrTiO_3$ thin films epitaxially grown on different cubic stustrates. The second- and first-order phase transitions are shown by thin and thick lines, respectively. Figure adapted from Pertsev et al. [64]

**4.2 Confirmation of 1:1 cation ratio in BiFeO₃ stoichiomtry**

Rutherford Back Scattering (RBS) was used to determine the composition of the films. As shown in Figure 4.3, the Bi/Fe ration was close to 1 within instrument resolution. This is an important fact to establish first, in order to make relation the following structural changes with respect to bulk crystals. However, the oxygen content is difficult to determine due to its small scattering cross section.

**4.3 Structure of (001), (101) and (111) oriented BiFeO₃ thin films**

This part of the work is conducted in collaboration with JieFang Li at Virginia Tech, also reported in ref [65]. In this section, films of 200nm BiFeO₃ and 20nm SrRuO₃ were used as model systems for the structural analysis, which in following sections will be extended to include the structural evolution for various film thickness and temperatures. Since SrTiO₃ has a smaller lattice constant compared with BiFeO₃, BiFeO₃ films grown on (100) oriented SrTiO₃ substrate will experience a compressive stress along (100). This will tend to favor films having tetragonally distorted lattice. Whereas for films deposited on (111) oriented SrTiO₃, the compressive stress will act along the (111) plane, favoring a rhombohedrally distorted structure. In consideration that bulk BiFeO₃ has a rhombohedral structure that is polarized along (111), films deposited on SrTiO₃ (111) should have a similar structure to that of free bulk. However, films grown on (001) and (101) SrTiO₃ should be expected to distort from the bulk rhombohedral structure.

Typical wide range θ-2θ scans for all three films are shown in Figure 4.5 (a). Only (00l), (l0l) and (lll) type diffraction peaks were observed, in the respective orientations; in addition to the peaks from SrRuO₃ and SrTiO₃. No peaks were detected that would be indicative of second phase formation in the films. Phi scans of
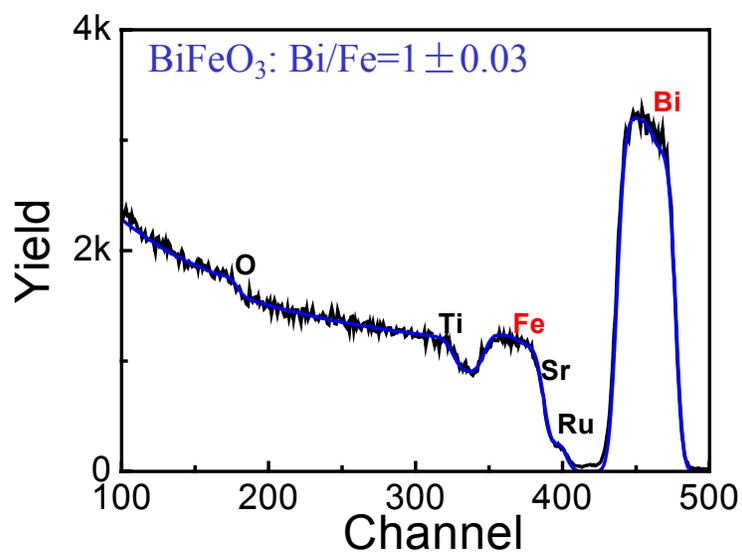
Figure 4. 3 RBS confirms that the films have a stoichiometric BiFeO$_3$ composition
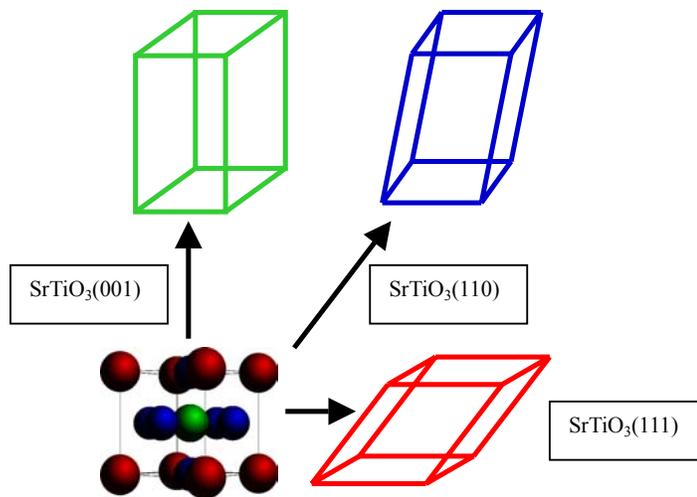
Figure 4. 4 Schematic illustration of the strain effect in BiFeO$_3$ thin films along different crystallographic directions.
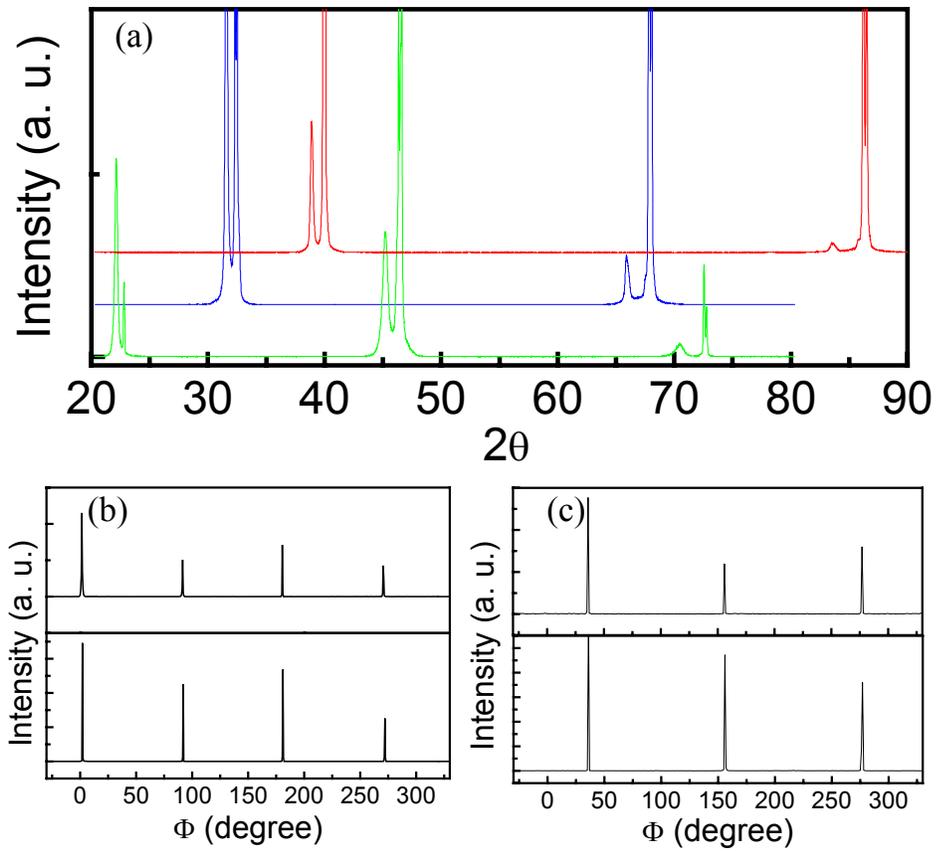
Figure 4. 5 Typical θ-2θ (a) scans for (001), (101) and (111) oriented BiFeO₃ thin films. (b) Φ scans for (001) oriented and (c) (111) oriented thin films, indicating four/three fold symmetry.

the BiFeO$_3$ (202) and SrTiO$_3$ (220) planes for a BiFeO$_3$/SrRuO$_3$/SrTiO$_3$ (001) specimen are shown in Figure 4.5 (b). The four sharp peaks originate from BiFeO$_3$, indicating that the film has good in-plane orientation. These four peaks show up at the same positions as four corresponding peaks from the SrTiO$_3$ substrate, demonstrating a cubic-on-cubic growth of BiFeO$_3$ with respect to the substrate. This observation also indicates that the film has a four-fold symmetry axis (or one very close to being four fold symmetric). Accordingly, Figure 4.5 (c) shows a phi scan of a BiFeO$_3$/SrRuO$_3$ /SrTiO$_3$ (111) specimen. A three-fold symmetry axis is clearly evident, indicating that this film has a rhombohedral structure.

We next performed XRD mesh scans along different zone axis for samples grown on differently oriented substrates. Mesh scans around (101) and (002) peaks are shown in Figure 4.6 for the (001) oriented BiFeO$_3$ thin film. The contour lines in this figure are given in a logarithmic scale. Besides the peaks from substrate and SrRuO$_3$, three peaks can be seen in the (101) mesh scan, consisting of (i) a splitting of $a_m$-domains along (H00); and (ii) a splitting between $a_m$- and $b_m$- domains along (H0L). $a_m$ and $b_m$ are defined in Figure 4.7. Only one peak was observed in the (002) mesh scan. These data give direct evidence that the stable phase of (001) oriented BiFeO$_3$ epitaxial thin layer is monoclinic. The monoclinic lattice parameters are (a=b,c; $\beta$-90$^o$)= (3.935 Å, 4.001 Å; 0.5$^o$). This is the monoclinic M$_a$ structure. It should be noted that the monoclinic angle $\beta$ of the thin-layer is nearly equal to that of the rhombohedral angle $\alpha$ of the bulk crystal.

Splitting of the BiFeO$_3$ (101) peak in the mesh scan indicates domain formation, which can relax the elastic energy. The monoclinic domain structures are illustrated schematically in Figure 4.7. Since the film is deposited on a substrate, the biaxial mismatch stress acting on the film's (100) plane fixes its out-of-plane axis. In the

monoclinic Ma phase, the polarization then lies in the (101) plane. The unit cell is deformed from the cubic parent structure, along one of the face diagonal, as indicated in the figure. Suppose the unit cell deforms along $b_m$, then in reciprocal space, $b_m^*$ will have two variants (tilted up and down respectively), and $a_m^*$ will have only one. Accordingly, when scans are taken along the $(H, H, 0)_c$ zone axis, three reflections will be observed, corresponding to the two $b_m^*$ variants and one $a_m^*$ variant. Whereas along $(0, 0, L)$, only one spot will be observed, which conrrsponds to the one $c_m^*$ variant, that is fixed by the substrate/film mismatch stress. Along the $(H, 0, 0)c$ zone axis, two reflections will be observed corresponding to the four variants of $a_c^*$ and $b_c^*$; but, since they are exactly the same in magnitude and tilt angle, the spots will overlap with each other, and consequently, only two can be seen. Unfortunately, it was impossible to do $(H, 0, 0)$ zone scan on the thin films with our XRD system as the separation of the domain states requires tilting to high angles outside of our system capability. However, as will be shown later in Chapter 7, we can create a materials system where the $c_c/c_m$ axis lies in-plane, and the $a_c/b_c$ lies out-of-plane by changing the substrate to $SrTiO_3$ coated Si. In this case, clear $(H, 0, 0)$ zone domain splitting was observed. [See Figure 7.3].
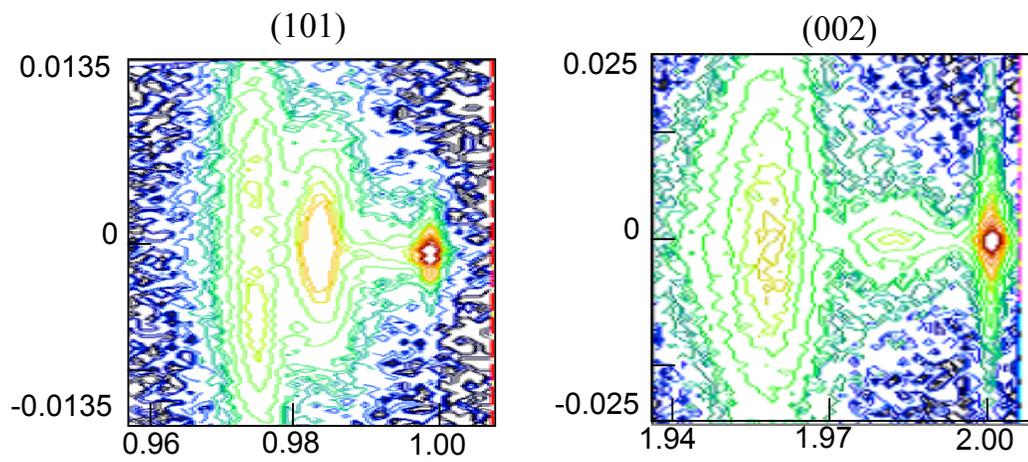
Figure 4. 6 (101) and (001) mesh scans for a (001) oriented BiFeO₃ thin layer. The intensity lines on the contour maps are shown in a logarithmic scale. The values of (HKL) are normalized to those of SrTiO₃ substrate, i.e., $(H,K,L)_{SrTiO3} \equiv (1,1,1)$.
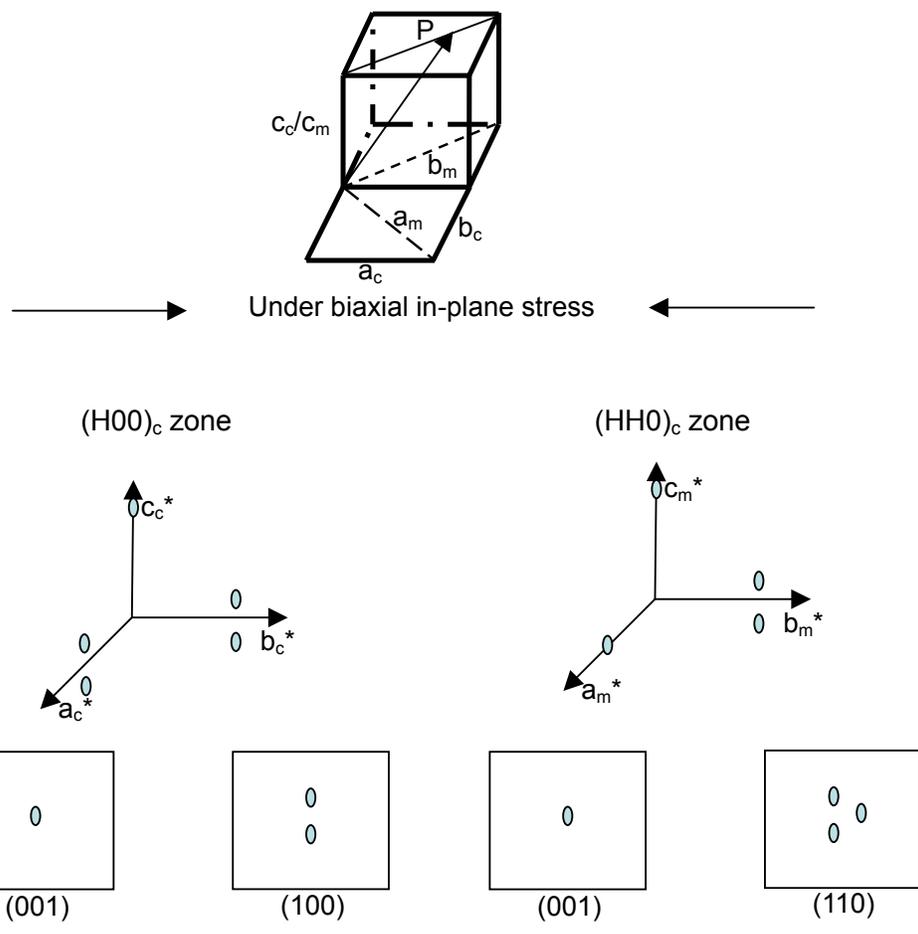
Figure 4. 7 Schematic illustrations showing the monoclinic domain structure in the films with Ma structure

Mesh scans taken along (001), (101) and (111) for a (111) oriented $BiFeO_3$ thin film are shown in Figures 4.8 (g)-(i). Both a sharp peak from the $SrTiO_3$ substrate (illustrated by doted lines) and a broad peak from the film can be seen in each figure. The values of (HKL) were determined by referencing to the interplanar spacings of the bulk single crystal ($d_{<001>}$=3.958 Å, $d_{<101>}$=2.809 Å, and $d_{<111>}$=2.306 Å). The (111) oriented $BiFeO_3$ films were found to grow epitaxially on (111) $SrTiO_3$ substrates with values of the interplanar spacings of $d_{<001>}$=3.959 Å, $d_{<101>}$=2.810 Å, and $d_{<111>}$= 2.306 Å. These interplanar spacings are almost equal to those of the bulk single crystal, as can be seen by comparisons in Table 4.1. Apparently, the (111) $BiFeO_3$ films are in a single domain state with a rhombohedral structure.

The lattice structures of (101) and (001) oriented $BiFeO_3$ thin films were found to be monoclinically distorted from the rhombohedral one. Mesh scans taken about (001), (101) and (111) are shown in Figures 4.8 (d)-(f) for (101) films, and in Figures 4.8 (a)-(c) for (001) films, respectively. The values of the interplanar spacings are summarized in Table 4.1. For both the (101) and (001) films, $d_{<101>}$ and $d_{<001>}$ show split. The (101) film is nearly single domain with $d_{<111>}$=2.307 Å (relative intensity, RI=0.98) and $d_{<101>}$=2.828 Å (RI~1). Whereas, the (001) film has a peak splitting about (111) and (101), with the dominant variant having values of $d_{<111>}$=2.278 (RI=0.9) Å and $d_{<101>}$=2.792 Å (RI=0.72). The value of $d_{<111>}$ is equal to that of one of the domain variants of the rhombohedral structure of the bulk crystal; whereas, $d_{<110>}$ was notably different than that for the bulk single crystal. This splitting indicates domain formation, with two variants populated. For both (101) and (001) oriented films, pronounced deviations in the value of $d_{<001>}$ were found from that of the bulk rhombohedral lattice. The value of $d_{<001>}$ increased from 3.959 Å for the (111) film to 3.984 Å for the (101) film, to 4.001 Å for the (001) film. The difference in the
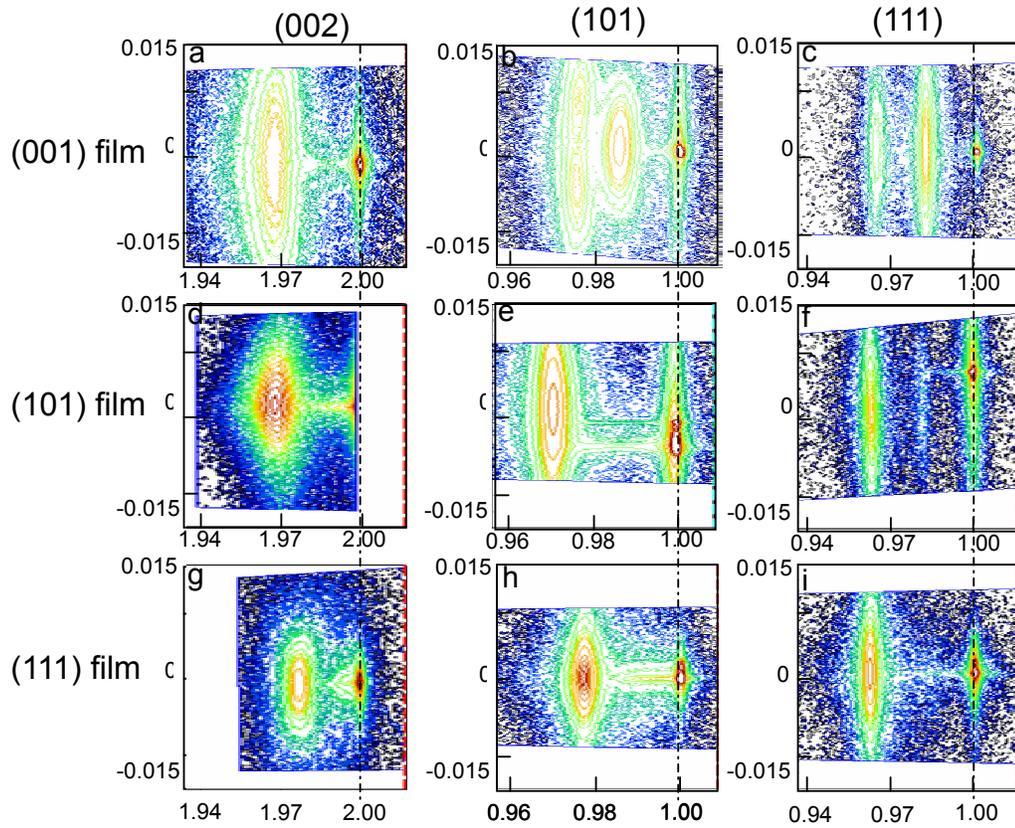
Figure 4. 8 Reciprocal lattice scans for various oriented BiFeO$_3$ films. (a) (002) scan for (001) film; (b) (101) scan for (001) film; (c) (111) scan for (001) film; (d) (002) scan for (101) film; (e) (101) scan for (101) film; (f) (111) scan for (101) film; (g) (002) scan for (111) film; (h) (101) scan for (111) film; and (i) (111) scan for (111) film. The values of (HKL) are normalized to those of SrTiO$_3$ single crystals, i.e., $(H,K,L)_{crystal} \equiv (1,1,1)$. Intensity is given on a log scale.

(001) and (101) spacings can be easily seen in Figure 4.8 as peaks shift away from $SrTiO_3$ peak.

For comparison, Mesh scans that were taken about (001), (101), and (111) for a $BiFeO_3$ bulk single crystal are shown in Figures 4.9 (a)-(c), respectively. A single peak was found along the (001), with $d_{<001>}$=3.958 Å. This is in agreement with previous reports of a rhombohedral phase. A peak splitting was found along the (101) with $d_{<101>}$=2.783 and 2.809 Å, and along the (111) with $d_{<111>}$=2.277 and 2.306 Å. The values of the interplanar spacings are summarized in Table 4.1. These results evidence a polydomain rhombohedral state.

In summary, $BiFeO_3$ films grown on (111) have a rhombohedral structure, identical to that of single crystals, whereas films grown on (101) or (001) are monoclinically distorted from the rhombohedral structure. The results demonstrate that lattice mismatch between the films and the substrate can dramatically change the film structure.
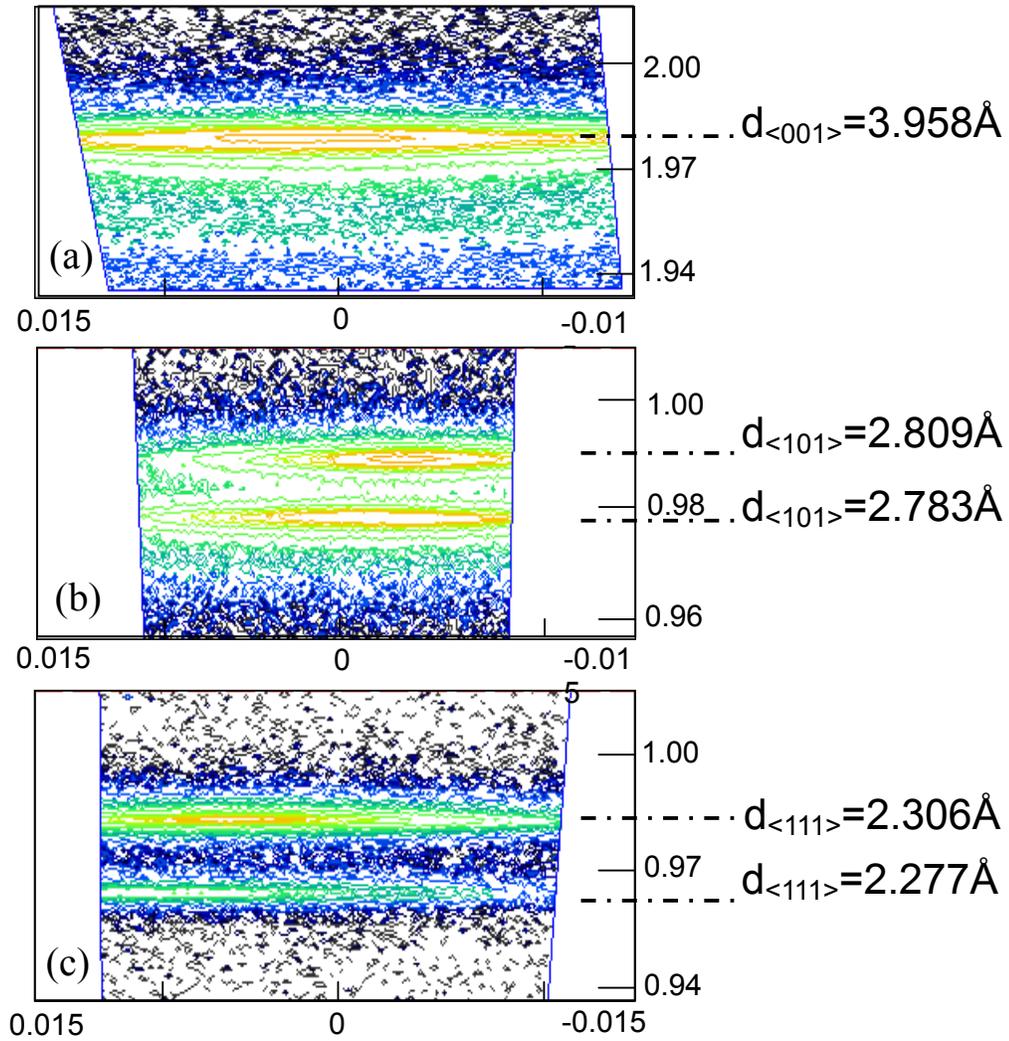
Figure 4. 9 Reciprocal space scans for BiFeO₃ single crystals taken about various zones about (001). (a) (H0L) zone; (b) (HHL) zone; and (c) (HHH) zone. The intensity is given on a log scale.

Table 4. 1 Summary of interplanar spacings and lateral correlation lengths obtained from small area reciporcal lattice scans for the variously oriented $BiFeO_3$ films and crystal. Peak splitting was observed along the (101) and (111), the relative intensities are designated by I, and the weaker peak is designated by brackets.

| Lattice spacing | Crystal | (111) Film | (101) Film | (001) Film |
|---|---|---|---|---|
| $d_{<001>}$ | 3.958 Å | 3.959 Å | 3.984 Å | 4.001 Å |
| $d_{<101>}$ | 2.783 Å (I=0.62) <br> [2.809 Å (I=0.38)] | 2.810 Å | 2.828 Å | 2.792 Å (I=0.72) <br> [2.816 Å (I=0.28)] |
| $d_{<111>}$ | 2.277 Å (I=0.87) <br> [2.306 Å (I=0.13)] | 2.306 Å (I=1.00) | [2.278 Å (I=0.02)] <br> 2.307 Å (I=0.98) | 2.278 Å (I=0.90) <br> [2.304 Å (I=0.10)] |

**4.4 Transmission Electron Microscopic analysis of the structure of BiFeO$_3$ thin films**

Transmission Electron Microscopy was used to characterize the quality and structure of BiFeO$_3$ thin films, in collaboration with Haimei Zheng. Figure 4.10 (a) illustrates a characteristic cross section image of a (100) oriented films. This image shows clear interfaces between substrate, SrRuO$_3$ and BiFeO$_3$; as also can be seen in the high resolution image, given in Figure 4.10 (b). The selected area electron diffraction pattern (SAED) taken along the pseudo-cubic (100) zone axis is shown in Figure 4.10 (c). Only one set of spots was observed, corresponding to the (001) and (010) variants, respectively. The in-plane and out-of-plane d-spacings were calculated from SAED pattern to be 3.94 Å and 4.00 Å, in good agreements with XRD results (within experimental error). We did not observe 90$^o$ domain, as typically seen in PZT in spite of the fact that BiFeO$_3$ has a fairly large distortion. The lack of 90$^o$ domains is due to the fact that BiFeO$_3$ has a Curie temperature of ~1100K, which is much higher than our deposition temperature of 943K. The film grows not in the prototypic cubic state, but rather the ferroelectric distorted one. Accordingly, no phase transition will occur on cooling. In addition, the structure of the BiFeO$_3$ thin films will be distorted by the substrate constraint, which will fix its in-plane parameter. Since two variants (see Figure 4.6) due to the tilting of c-lattice were observed in the XRD mesh scans, the two variants should also be observed in SAED by directing the electron beam along the appropriate zone axis. This was confirmed by tilting the sample to the (11$\bar{1}$) zone. Accordingly, three diffraction spots were found in the SAED pattern, corresponding to the domain and rotation splitting of the two (101) variants, as shown in Figure 4.11. Unfortunately, due to the large tilting angle, clear dark field images could not be obtained from the diffraction pattern, which could have revealed the
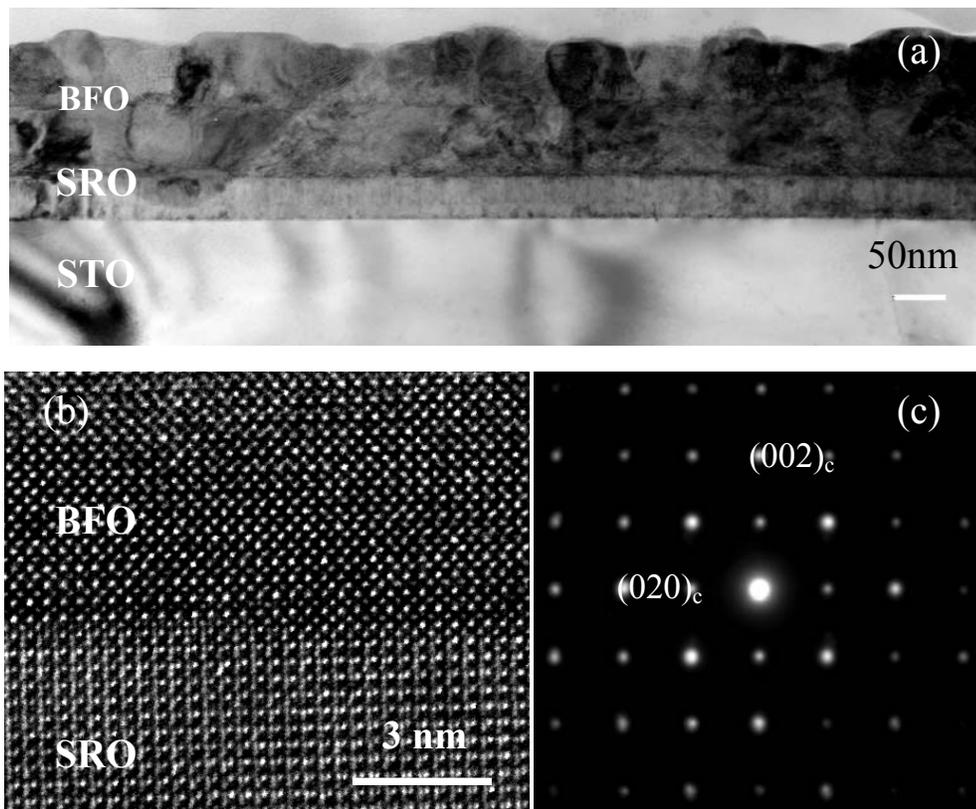
Figure 4.10 (a) TEM cross-section image of $BiFeO_3/SrRuO_3/SrTiO_3$ (001) samples. (b) High resolution of the $BiFeO_3/SrRuO_3$ interface. (c) (100) zone selected area electron diffraction pattern of the same sample with pseudo-cubic index.

domain configuration of the film giving rise to this splitting.

The pseudo-cubic (100) zone SAED was also indexed based on a rhombohedral structure, as shown in Figure 4.12 (a). In the rhombohedral structure, the (012) and $(11\bar{2})$ are equivalent planes (i.e., the pseudo-cubic (001)). Thus, they should have the same interplanar d-spacing, as shown in the simulated SAED given in Figure 4.12 (b). However, analysis of the SAED pattern revealed that these planes were not equivalent, indicating lose of three-fold symmetry. This demonstrates that the (001) $BiFeO_3$ films have lost the 3-fold symmetry axis along the (111) and can not be rhombohedral.

The transmission electron microscopic images of (101) and (111) oriented $BiFeO_3$ films and corresponding SAED patterns are shown in Figure 4.13. Uniform contrast of the images reveals better quality of the epitaxial films, compared with the (001) oriented films. This could be due to a small distortion from single crystal. SAED patterns revealed single domain states for both films, consistent with the XRD results.

Superstructure diffraction spots were observed along the $(1\bar{1}0)$ zone from both (111) and some of the (101) oriented films. These spots are the ½(1,1,1) type, likely originate from the counter rotation of the oxygen octahedrons about (111). Study of superstructure arises from octahedron tilting in perovskite oxides traces back to 1970s. [66,67] Detail investigations in this direction will help to understand the effect of epitaxial strain on the lattice deformation and oxygen octahedron rotation, which could in turn change the electric and magnetic properties in case of $BiFeO_3$.
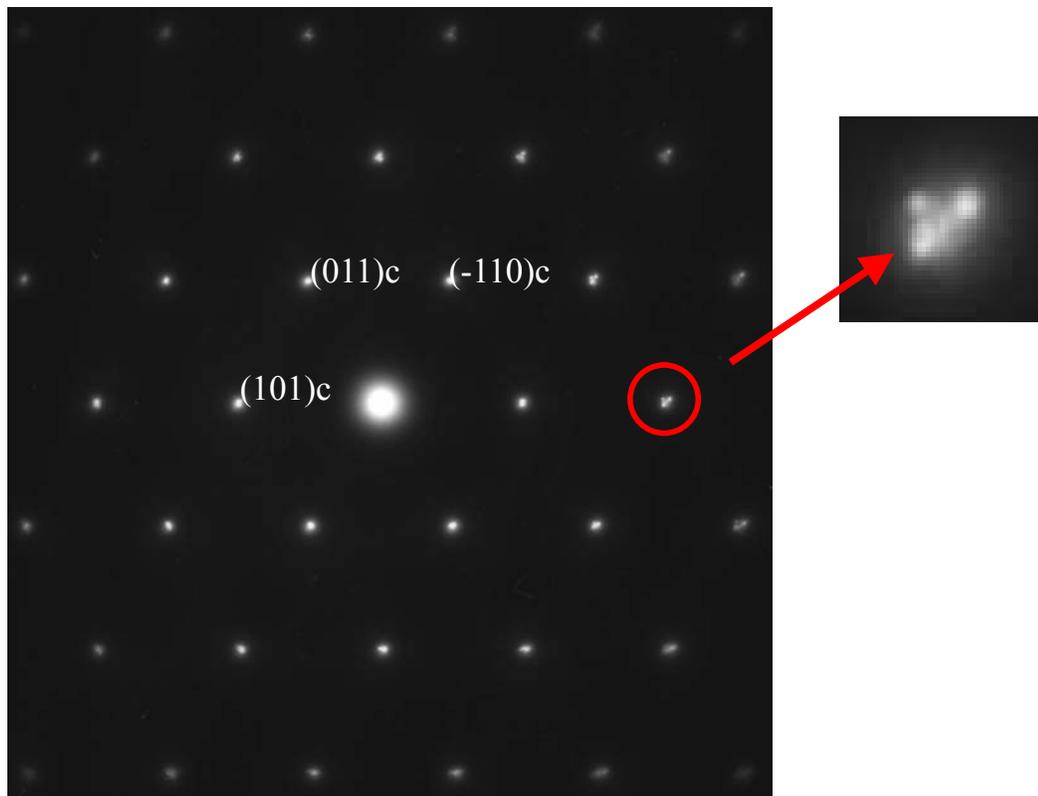
Figure 4. 11 (11-1) zone SAED for a (001) oriented BiFeO$_3$ thin film. Two variants were observed for (1-10) planes, and one variant has a rotation split.
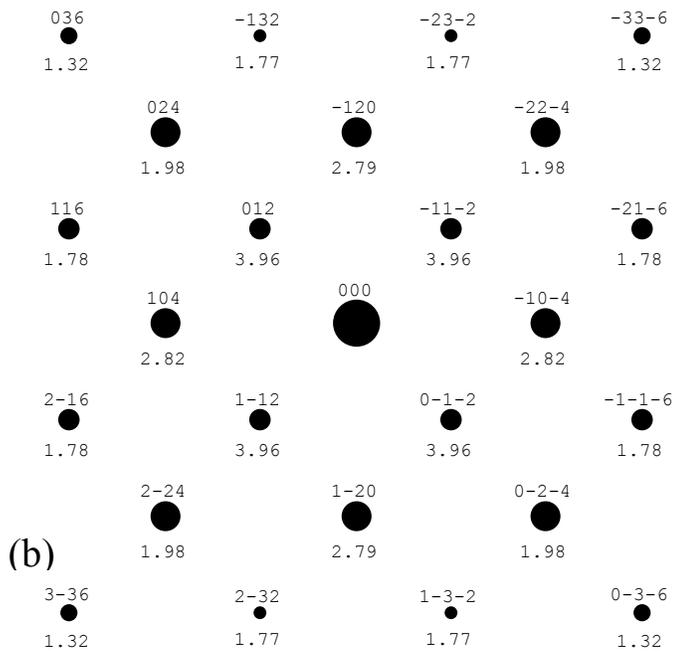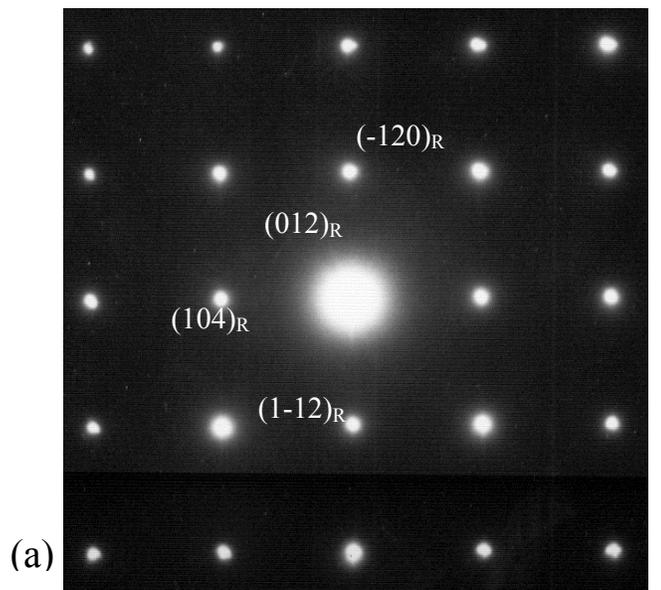
Figure 4. 12 (a) Electron diffraction pattern with rhombohedral index. (b) Simulated [42-1] zone diffraction pattern of rhombohedral BiFeO$_3$
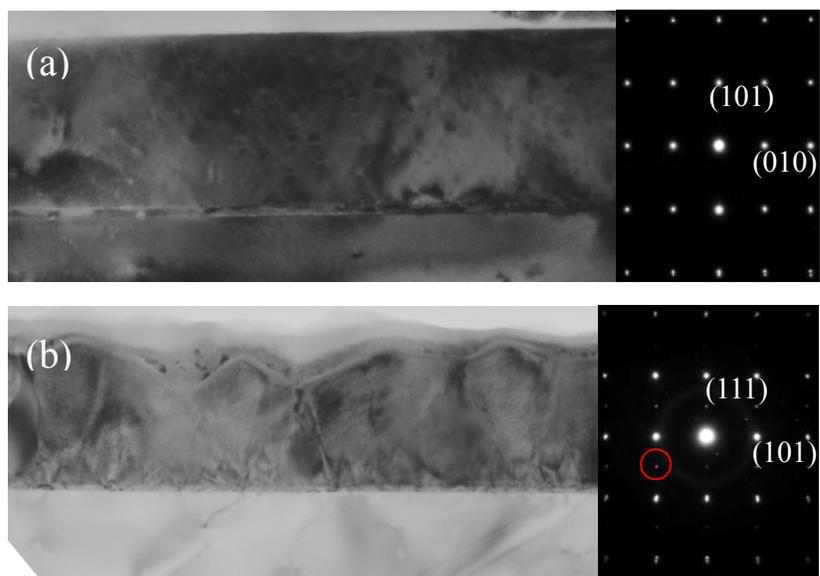
Figure 4. 13 TEM images for (a) (101) and (b) (111) oriented films with (10-1) zone

SAEDs as insets. Superstructure diffraction spot is indicated by a circle.

**4.5 Film thickness and temperature dependence**

**4.5.1 Thickness and buffer layer effects**

The (001) oriented films have a monoclinic structure, which is different from the bulk structure. This was attributed to the epitaxial stress from the substrate. To better understand the effect of epitaxial strain, we performed investigations on $BiFeO_3$ films of various thicknesses. A set of films with thickness between 30nm and 600nm were deposited by PLD. The effect of $SrRuO_3$ electrode was also studied, by comparing specimens with and without electrodes.

Figure 4.14 (a) shows sections of the θ-2θ scan for a set of $BiFeO_3$/$SrRuO_3$ /$SrTiO_3$(001) films. The $SrRuO_3$ was ~20nm thick. Strain effect is clearly seen from the peak shifting. The out-of-plane d-spacing was found to decrease with increasing film thickness as can be seen in Figure 4.14 (b). Such a decrease is expected, as $SrRuO_3$ and $SrTiO_3$ have smaller lattice parameters than $BiFeO_3$. Figure 4.14 (b) also shows similar measurements for (i) a set of specimens without intermediate $SrRuO_3$ electrodes, and (ii) another set with ~50nm $SrRuO_3$ electrodes to illustrate the influence of buffer layer thickness. Films grown directly on $SrTiO_3$ were found to have similar out-of-plane parameters as those grown on thin $SrRuO_3$. However, $BiFeO_3$ films grown on top of 50nm $SrRuO_3$ layers were different.

These observations are consistent with the critical thickness of $SrRuO_3$ being ~30nm on $SrTiO_3$. Below this thickness, the in-plane lattice is coherent with that of the $SrTiO_3$ substrate. However, 50nm $SrRuO_3$ layer has a larger in-plane parameter close to its bulk value due to stress relaxation by dislocation formation. The $BiFeO_3$ films thus experience less compressive stress in-plane and have a smaller out-of-plane d-spacing. These results are consistent with dislocation formation playing an important role on epitaxial strain relaxation.
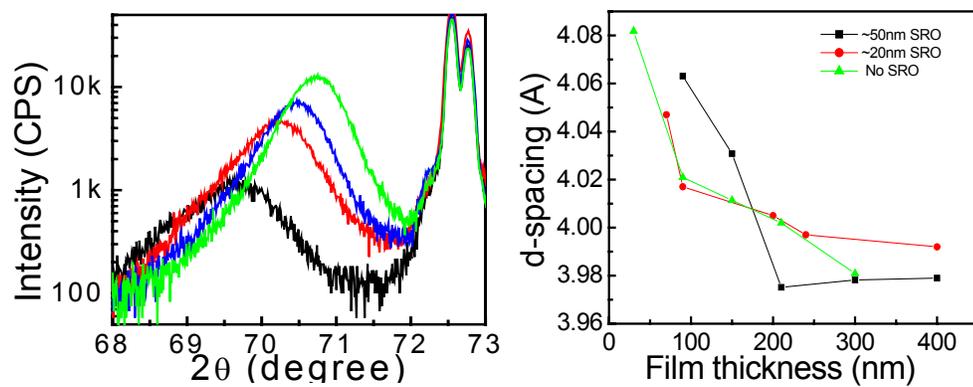
Figure 4. 14 (a) Sections of θ-2θ scan for a set of films $BiFeO_3/SrRuO_3/SrTiO_3(001)$ films. The $SrRuO_3$ is ~10nm. (b) Out-of-plane d-spacing vs. films thickness, films grown with/without $SrRuO_3$ are shown.
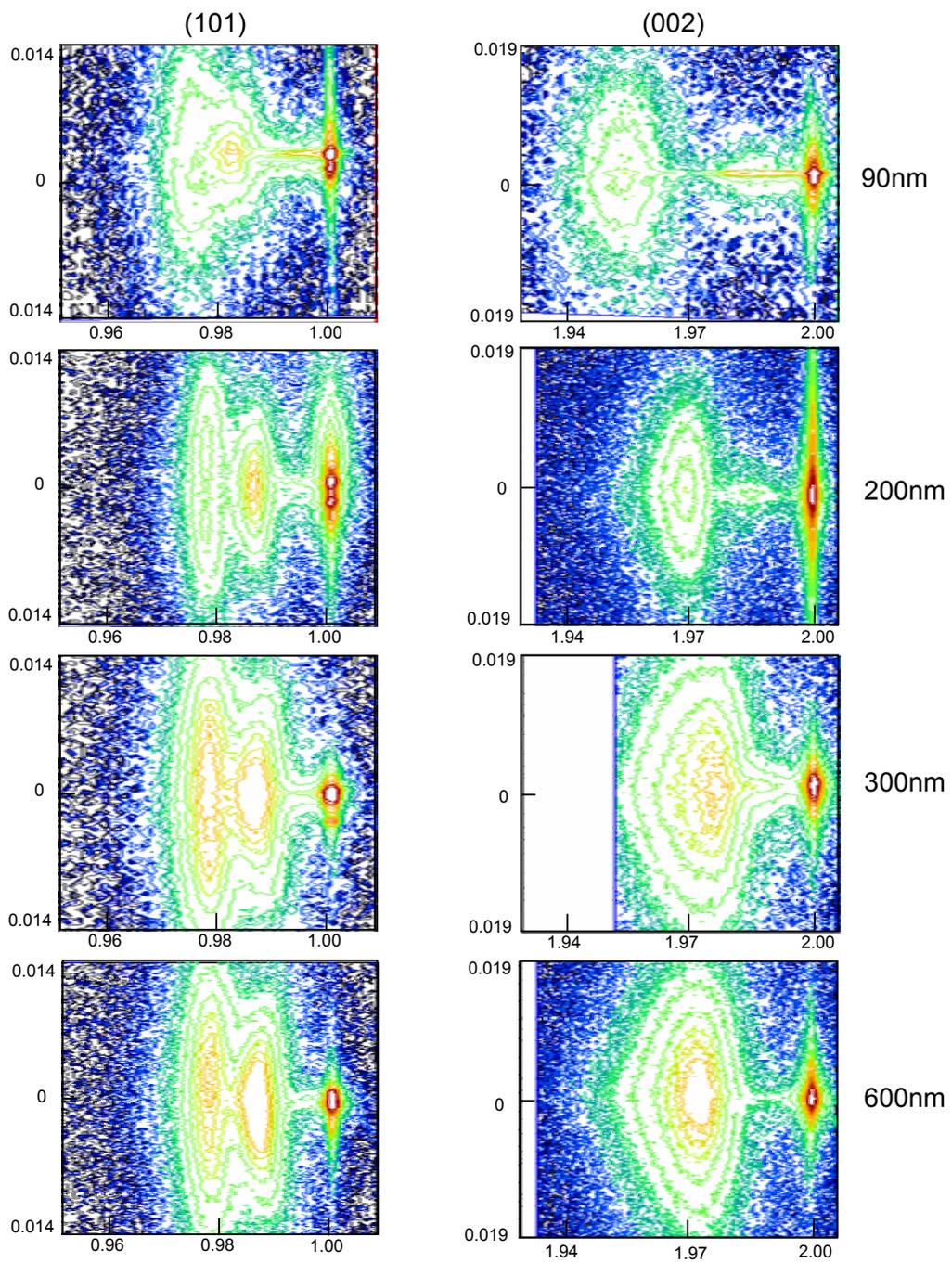
Figure 4. 15 Mesh-scans of BiFeO$_3$/SrRuO$_3$/SrTiO$_3$(001) samples with different thickness.

It is interesting to note that the out-of plane lattice parameter of $BiFeO_3$ films does not relax back to the single crystal value even at a thickness of >400nm, even though a relaxation behavior was observed. This is quite unusual for perovskite oxides, since typical relaxation length is ~200nm or less. One possible reason is that a noticeable amount of oxygen vacancies were incorporated in the film and increased the unit cell volume due to their larger radius. This is likely because that the films were deposited in an oxygen partial pressure of 20mTorr, much smaller than typical value for perovskite oxides of ~100mTorr.

Figure 4.15 shows mesh scans taken along the (H0L) and (H00) zones for a set of samples with different thickness. The $SrTiO_3$ (101) and (001) interplanar d-spacings were set as the reciprocal lattice unit. Relaxation of the strain in the $BiFeO_3$ layers is clearly evident by a peak shift towards the $SrTiO_3$ reflections. Furthermore, in the (002) scans, $BiFeO_3$ has a symmetric peak profile for a 90nm film. However, for thicker films, the (002) peak becomes increasingly asymmetric, indicating a lattice d-spacing gradient in the films. This is consistent with a relaxation of the epitaxial strain through the thickness of the films.

Similar strain effects were also observed for films grown on (110) and (111) oriented $SrTiO_3$ substrates, as shown in Figure 4.16. Again, an effect of the $SrRuO_3$ electrode layer on the thickness dependence of the structure of $BiFeO_3$ films can be seen. The changes of $BiFeO_3$ out-of-plane lattice d-spacing are much smaller in both cases comparing with films grown on (001) $SrTiO_3$ substrates. This is consistent with smaller mismatch with the substrate.
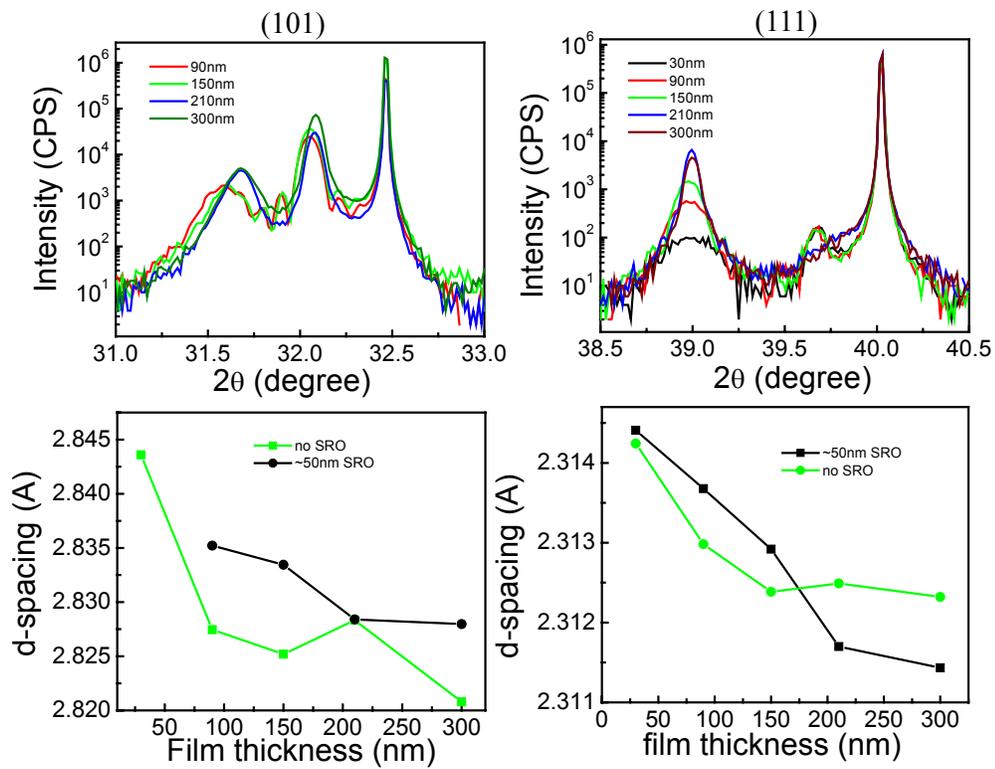
Figure 4. 16 Lattice thickness dependence with/without SrRuO$_3$ for (101) and (111) oriented thin films

**4.5.2 Lattice parameter temperature dependence**

Temperature dependent lattice parameter measurements were conducted to determine the structural evolution of the BiFeO$_3$ films. It is well known that BiFeO$_3$ is unstable at elevated temperature in an atmosphere of air without contact with the Fe$_2$O$_3$/Bi$_2$O$_3$ flux. [68] This leads to decomposition of BiFeO$_3$ into Bi$_2$O$_3$ and Bi$_2$Fe$_4$O$_9$ at temperature exceeding that of the eutectic temperature of 777$^o$C, and into Bi$_{46}$Fe$_2$O$_{72}$ and Bi$_2$Fe$_4$O$_9$ at temperature below that. This instability prevented us from measuring the lattice parameters at higher temperature.

During the temperature dependent measurements, some of the films survived up to 600$^o$C without noticeable decomposition. The results for these films are shown in Figure 4.17 for a (001) film. A lattice expansion with increasing temperature can be seen, whose derivation ($\frac{d\varepsilon}{dT}$) is close to that of the thermal expansion coefficient 6x10$^{-5}$ deg$^{-1}$ of bulk crystals. Similar thermal expansions of the lattice parameters were found for the (101) and (111) oriented films, as shown in Figure 4.18.

In addition, the results for these films exhibit possible evidence of a small structural change at around 400$^o$C, as indicated by a sudden change of lattice d-spacing. It is interesting to note that the temperature of this anomaly corresponds to the paramagnetic-antiferromagnetic Neel temperature of bulk BiFeO$_3$ crystal. This transition has been observed by different groups on bulk samples [24,69,70], with similar lattice parameter changes as shown in Figure 4.17 and 4.18 for my films. This offers plausible arguments for a spin-phonon coupling in the epitaxial thin film system. However, this possibility in the films must be counterbalanced by the fact of film decomposition not limit my ability to repeatable reconstruct the results.
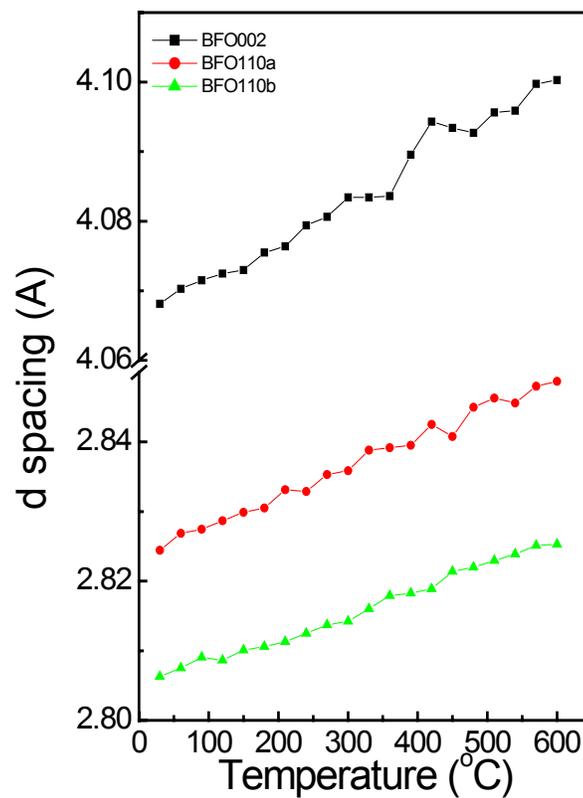
Figure 4. 17 Lattice vs. temperature for $BiFeO_3$(100nm)/$SrTiO_3$(001). A jump in the out-of-plane lattice can still be seen despite the noise due to the small thickness.
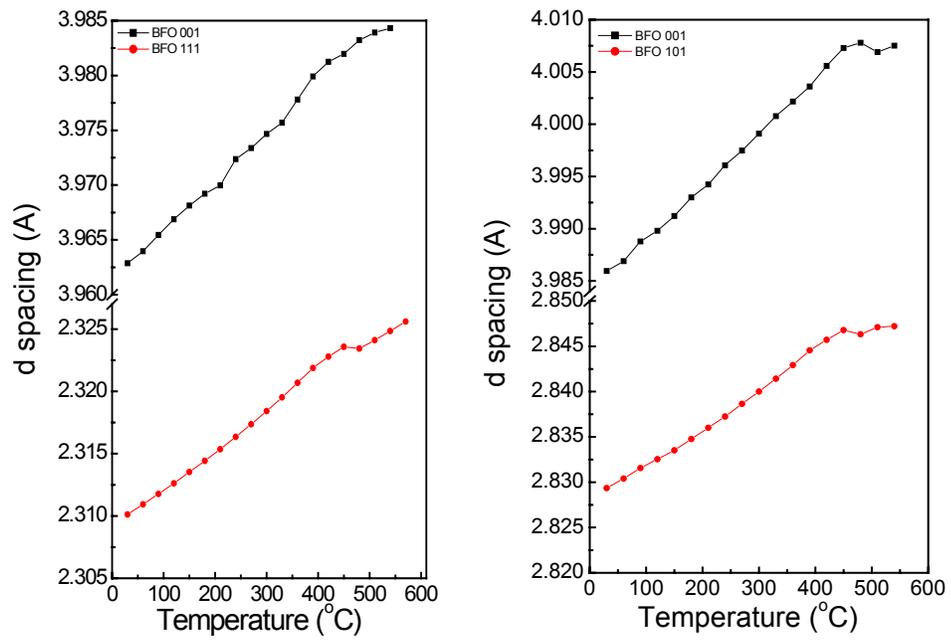
Figure 4.18 Lattice parameters vs. temperature for (a) $BiFeO_3$(200nm)/$SrRuO_3$ (~20nm) /$SrTiO_3$(111) and (b) $BiFeO_3$(200nm)/$SrRuO_3$ (~20nm) /$SrTiO_3$(101). Clear lattice change between $400^o$-$500^o$ can be seen.

# CHAPTER 5, ELECTRICAL PROPERTIES OF BiFeO$_3$

# THIN FILMS

In chapter 4, the structures of BiFeO$_3$ thin films deposited on (001), (101) and (111) SrTiO$_3$ substrates were characterized by XRD and TEM. In this chapter, corresponding electrical property characterizations are presented. 200nm films deposited on (001), (101) and (111) SrTiO$_3$ substrates were used as model systems to establish the properties along different crystallographic directions. Then, studies as a function of film thickness were performed for each orientation.

## 5.1 Electrical properties of (001), (101) and (111) oriented BiFeO$_3$ thin films

All films were found to have resistivities of ~$10^9$ $\Omega$cm under zero bias field. This is comparable to prior values for other typical perovskite thin films, such as Ti-rich epitaxial Pb(Zr$_x$Ti$_{1-x}$)O$_3$. [71] Good insulation resistance enables measurements of the high field electrical properties of films. The ferroelectric properties were characterized for the differently oriented thin layers using a polarization hysteresis (i.e. P-E loop) measurement.

Figure 5.1 (a) shows P-E loops for all three orientations, taken at a measurement frequency of 17 kHz. Square loops were observed for all three orientations, indicating little contribution to the polarization from leakage current. Remnant polarizations (P$_r$) of ~55 $\mu$C/cm$^2$ for (001) films, ~80 $\mu$C/cm$^2$ for (101) films, and ~100 $\mu$C/cm$^2$ for (111) films were found. A simple calculation shows that the values of $\sqrt{3}$ P$_{(001)}$, $\dfrac{\sqrt{6}}{2}$ P$_{(101)}$, and P$_{(111)}$ are nearly equal, indicating that the spontaneous polarization (P$_s$) lies close to (111). The values observed along (001) and (101) directions are its projections. The stability of the polarization was confirmed by retention measurements, no noticeable
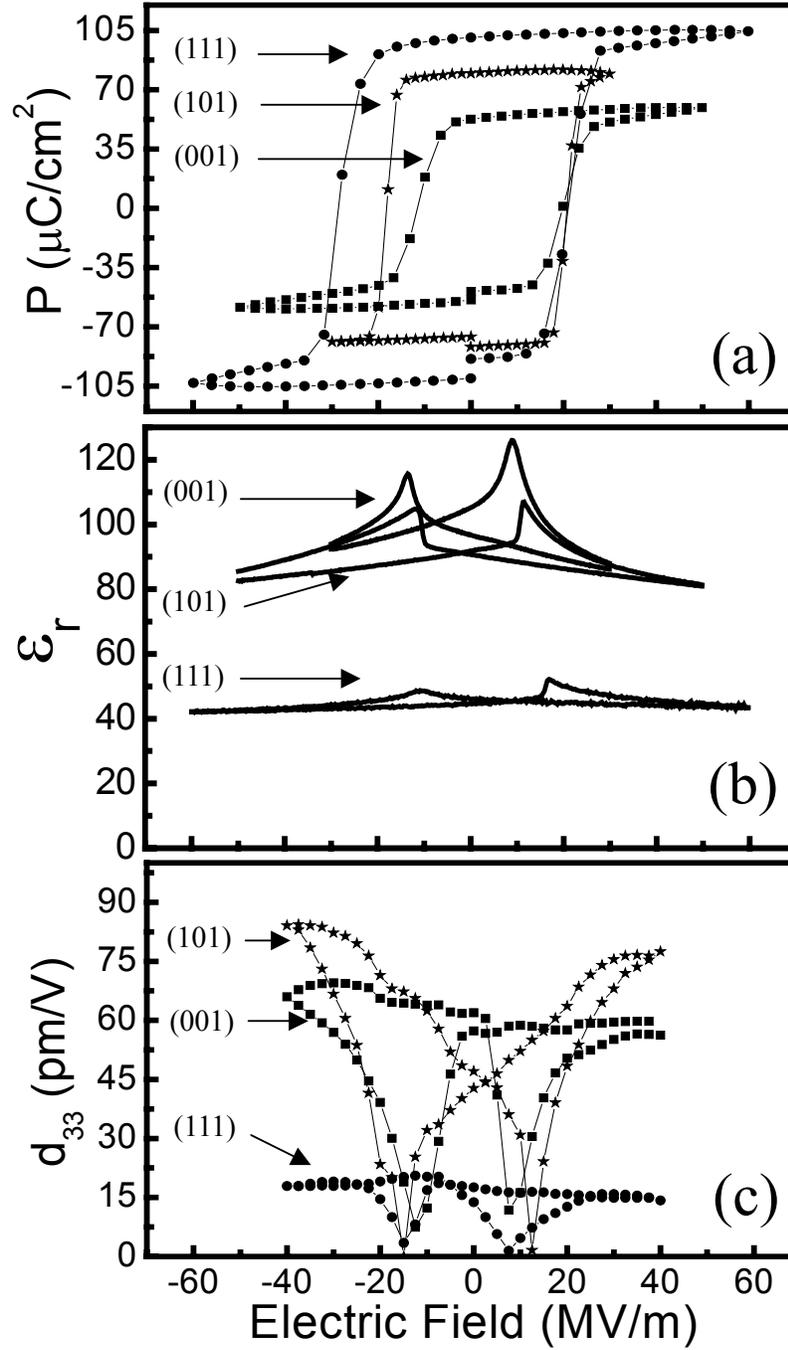
Figure 5. 1 (a) Ferroelectric hysteresis loops, (b) relative dielectric constants and (c) piezoelectric coefficients for the three orientations. $P_r(111){>}P_r(101){>}P_r(001)$, $\varepsilon_r(001){>}$ $\varepsilon_r(001){>}$ $\varepsilon_r(001)$ and $d_{33}(001){>}d_{33}(101){>}d_{33}(111)$ were observed.

change in $P_r$ was found after several days.

The remnant polarizations of BiFeO$_3$ films are dramatically higher than that previously reported for single crystals ($P_s(111)=6.1\mu C/cm^2$). [29] This could be due to changes in the films induced by epitaxial constraint. Or, an alternative explanation is that BiFeO$_3$ has a high intrinsic polarization, but previously due to poor bulk sample resistance, a complete saturated polarization could not be obtained. The first possibility was supported by the fact that XRD analysis does show dramatic changes in the film structure as revealed in Chapter 4, but can not explain the highest polarization for (111) films whose structure is identical to bulk. The second explains the high polarization from (111) film and the $\sqrt{3}\, P_{(001)} = \dfrac{\sqrt{6}}{2}\, P_{(101)} = P_{(111)}$ relation.

But, it can not explain why small polarizations were previously observed even from highly resistive BiFeO$_3$ ceramics and thin films.[72] Further investigations of high quality BiFeO$_3$ crystals are necessary to clarify this issue. Details of our efforts to understand this problem will be presented in the following section.

The dielectric properties of the films were also studied. Figure 5.1(b) shows the relative dielectric constant ($\varepsilon_r$) as a function of electric field (E) taken at a frequency of 100 kHz. We notice that the coercive fields indicated in dielectric constant response don't coincide with those obtained from P-E loops. This is due to the fact that these two measurements were performed at different frequencies. The dielectric constant was measured at 100 kHz, using a small AC signal; whereas the hysteresis loops were taken with triangle waves with corresponding frequency of 1-17 kHz. The (111)-oriented film had a relative dielectric constant of ~45, which is close to that previously reported for bulk samples.[73,74] This is consistent with an underlying structural similarity between epitaxial (111) films, crystal and ceramics.

Several differences between dielectric constant vs. electric field characteristics for (001), (101) and (111) oriented films should be noted. These are

(i) that the (001) and (101) oriented films had much higher relative dielectric constants ($\varepsilon_r \sim 80$ and 100, respectively) compared with (111) films;

(ii) that the value of $\varepsilon_r$ can be seen to be significantly increased with increasing E during polarization switching for (001) and (101) oriented films, but not for the (111) film even though the switchable polarization is the highest. This indicated that the (111) films have negligible contribution to $\varepsilon_r$ from domain dynamics; and

(iii) that the (101) and (111) films show much sharper increases of the dielectric constants near their coercive fields, whereas that of the (001) film was broader.

These features might be understood by recognizing, as discussed above, that the spontaneous polarization lies close to the (111) direction. Along (111), only $180^o$ domain switching will contribute to the dielectric response. Whereas along (001), applied E is at an angle of $\sim 54^o$ with respect to the easy axis of the polarization, thus polarization rotation may contribute significantly to the enhancement of the dielectric constant before $180^o$ domain reversal happens. Further evidence of this conjectured difference in the polarization reverse mechanism between E applied along different crystal directions can be seen by comparing the P-V loops, Figure 5.1 (a). In these data, a much sharper domain switching (near Ec) was observed along (111), relative to (101) and (001). Accordingly, polarization rotation under small applied E may increase the effective dielectric constant of (001) films; (101) films may also have enhanced effective permittivity somewhat between that of (001) and (111) films.

Figure 5.1(c) shows the piezoelectric hysteresis loops, measured using a scanning

90

force microscope in the peizo-response mode. Remnant longitudinal piezoelectric coefficient values of ~60 pm/V, ~42 pm/V and ~20 pm/V were observed for (001), (101) and (111) films, respectively. These results demonstrate a common trend between the dielectric and piezoelectric constants, i.e., $\varepsilon_r(001) > \varepsilon_r(101) > \varepsilon_r(111)$, and correspondingly $d_{33}(001) > d_{33}(101) > d_{33}(111)$. Such a commonalty is often found in perovskite ferroelectrics. [75] In a rhombohedral FE phase, the spontaneously polarization axis lies along (111), whereas the highest susceptibilities (dielectric and piezoelectric coefficients) are along the (001) rotated $54^{o}$ away from the (111). Both susceptibilities are high due to a "softening", which is most probably a polarization rotation and the corresponding structural distortion.

In summary, variously oriented $BiFeO_3$ thin films with the same thickness of 200nm were characterized as model systems. Electrical characterizations revealed a spontaneous polarization whose easy axis lies close to (111). On the other hand, both piezoelectric and dielectric coefficients were found to be highest along (001) direction. The results can be understood based on polarization rotation under an external electric field. Detailed investigations of the electrical properties and strain effects in films of various thicknesses will be shown in section 5.3.

**5.2 Why do BiFeO$_3$ thin films have large polarizations?**

In Figure 5.1, it was demonstrated that high quality BiFeO$_3$ films have much larger polarizations than previously reported for either BiFeO$_3$ single crystals or ceramics. However, since our initial report, [76] there have been numerous investigations indicating enhanced polarization values. Some of the recent results are summarized in Table 5.1.

It is natural to ask (i) where does the high polarization in epitaxial thin films come from; and (ii) what is the intrinsic property of BiFeO$_3$? There are basically two possible explanations for the discrepancy in observed polarization values, attributed to extrinsic or intrinsic causes, respectively.

1)  BiFeO$_3$ thin films are different from bulk.

(001) and (101) oriented BiFeO$_3$ films were shown to have different structure from single crystal, due to epitaxial stress. The large polarizations observed could then be due to structural changes. First principle calculations were performed by Neaton et al. [78] for (001) oriented films, starting with the same double perovskite structure as that of the rhombohedral phase, which is necessary to accommodate a G-type antiferromagnetic spin arrangement. In order to simplify the computations, a tetragonal structure belonging to the space group P4mm containing one formula unit per unit cell was chosen for the calculations. (i.e. the small monoclinic distortion that we observed by XRD was neglected.) Lattice parameters measured by electron diffraction for 200nm films (a=3.935Å and c/a=1.016) were used in the calculations. The magnitudes of the ionic displacements relative to the centrosymmetric strained perovskite structure were found to be extremely large: relative to the Bi ion, the Fe (Wyckoff position 4b) and apical O (4b) are displaced by about 9% (of the c-axis

Table 5. 1 Various measured values for the polarization in BiFeO$_3$, in chronological order with the oldest at the top.

| Sample studied | Polarization ($\mu$C/cm$^2$) | Reference |
|---|---|---|
| Bulk single crystal (low resistivity) | 3.5 along (001) | J. Teague, Solid State Comm. 8, 1073(1970) |
| 0.7BiFeO$_3$-0.3BaTiO$_3$ films (300nm) | 2.5 along (001) | K. Ueda, APL, 75, 555 (1999) |
| Polycrystalline BiFeO$_3$ thin films (200nm) | 2.2 | V. R. Palkar, APL, 80, 1628(2002) |
| Epitaxial BiFeO$_3$ thin films | 50 along (001) | J. Wang, Science. 299, 1719(2003) |
| Polycrystalline BiFeO$_3$ thin films | 35.7 | K. Y. Yun, APL, 83, 3981(2003) |
| Bulk ceramics | 8.9 | Y. P. Wang, APL. 84, 1731(2004) |
| Polycrystalline thin films (300nm) | 158 | K. Y. Yun, JJAP, 43, L647(2004) |

parameter) and 13%, respectively, and the equatorial O atoms (8c) by nearly 18%.

Notably, the Fe ion moves off-center relative to the distorted oxygen octahedron

altogether by about 4%, reducing its coordination from six to just a single O ion. The

corresponding calculated value of $P_s$ = 63.2 $\mu C/cm^2$ along [001]. (Here the

polarization quantum is 103.5 $\mu C/cm^2$ along [001]) These results of first-principles

calculations are consistent with the experimentally observed large values of

polarization of the (001) oriented films.

This model fails to explain the large polarization observed in (111) oriented films,

where the same rhombohedral structure as of single crystal was maintained, only that

the <111> d-spacing was increased due to epitaxial strain.


2) $BiFeO_3$ has an intrinsic large polarization.

A more natural explanation for the large observed polarization and the $\sqrt{3}\, P_{(001)} =$

$\dfrac{\sqrt{6}}{2} P_{(101)} = P_{(111)}$ relation is that $BiFeO_3$ has large intrinsic polarization along (111) in

the rhombohedral structure, whereas what we observe along (001) and (101) are

simply projections from the easy (111) polarization direction.

Early investigations by Teague et al reported a polarization value of ~3.5$\mu C/cm^2$

along (001), which when projected onto (111) yielded a spontaneous polarization of

6.1$\mu C/cm^2$. This study was performed on single crystals immersed in liquid nitrogen,

which was done to reduce leakage current. The authors pointed out that this value is

"considerably lower than what would be expected from a compound with such a high

Curie temperature and distortion". It was also stated that high coercive field may

prevent full polarization switching.

In 1968, Abrahams et al. [77] reported an experimental relationship between the

Curie temperature, atomic displacement Δz and spontaneous polarization as following:

$$T_c = \frac{\kappa}{2k}(\Delta z)^2 ; \qquad\qquad \text{Equation 5.1}$$

$$Ps = (258 \pm 9)\Delta z \ \mu C/cm^2 , \qquad\qquad \text{Equation 5.2}$$

where $\frac{\kappa}{2k} = (2.00 \pm 0.09) \times 10^4 \ ^o K \ \overset{o}{A}^{-2}$, $\kappa$ is a constant and has the dimension of force, and k is the Boltzmann's constant. The magnitude of the force constant is $\kappa = (5.52 \pm 0.25) \times 10^4 \, dyn \cdot cm^{-1}$. This value is similar in magnitude to the force constant between atoms in a crystalline solid, suggesting that $\kappa$ may be interpreted as an average force constant between the homopolar atom and the oxygen framework along the polar direction. [78] This relationship was proven to be true for most displacive ferroelectrics. Simple calculation based on these equations shows that BiFeO$_3$ single crystal should have a spontaneous polarization as high as 60μC/cm$^2$, taking the Curie temperature of 1100K.

To be more precise, it is standard to estimate the spontaneous polarization by simply summing the product of atomic displacements (from a centro-symmetric reference structure) and their corresponding Born effective charges (BECs) for archetypal perovskite ferroelectrics. This estimate corresponds to computing the Cartesian components of the polarization $\Delta P_\alpha$ to linear order in the atomic displacements, i.e.

$$\Delta P_\alpha \cong \sum_{j\beta} \frac{\partial P_{j\beta}}{\partial u_{j\beta}}(u_{j\beta} - u_{0j\beta}) = \frac{e}{\Omega}\sum_{j\beta} Z^*_{j\alpha\beta}\Delta u_{j\beta} ,$$

where $\Delta u_{j\beta}$ is the displacement of ion j in Cartesian direction β, $Z^*_{j\alpha\beta}$ is its Born effective charge tensor, and $\Omega$ is the volume of the unit cell. The zero in the subscripts

refers to an insulating centro-symmetric reference structure (in case of $BiFeO_3$, either cubic perovskite or $R\bar{3}c$). Defining such a reference implicitly selects half of a specific structural (or switching) pathway along which the polarization changes sign, as it would in an electrostatic Sawyer-Tower measurement. Applying this technique to $BiFeO_3$ proved to be rather simple, since in $BiFeO_3$, $Bi^{3+}$, $Fe^{3+}$ and $O^{2-}$ all displace along the (111) direction - $O^{2-}$ also rotate around [111] and did not contribute to the calculation. Using this equation and the Born effective charges calculated by Neaton et al [79] and the atomic displacements measured by [25], we can estimate the polarization of $BiFeO_3$ to be ~94.7$\mu C/cm^2$, which is in good agreement with the high values observed in thin films. The same calculation using theoretically calculated atomic displacements yields slightly smaller (but at the same order) values, as shown in Table 5.2.

Table 5. 2 Born effective charges (BECs) and corresponding polarization for displacements along [111] for $BiFeO_3$ in theR3c structure. Table adapted from Neaton et al. [82]

| | Born Effect Charges | | | Polarization |
|---|---|---|---|---|
| | Bi | Fe | O | |
| LSDA | 4.28 | 3.26 | -2.50 | 84.2$\mu C/cm^2$ |
| LSDA+U | 4.37 | 3.49 | -2.61 | 87.3$\mu C/cm^2$ |

This intrinsic high polarization model successfully explains the measured high values for (001), (101) and (111) oriented epitaxial thin films. However, it does not assist in explaining why numerous other studies have reported noticeably low values as summarized in Table 5.1. Several groups have reported polarization values of <

$10 \mu C/cm^2$ from samples that are highly resistive and stoichiometric. It is quite possible that such low values of polarization can not simply be explained based on sample quality or high coercive field.

## 5.3 Strain effects in BiFeO$_3$ thin films

Epitaxial stress can perturb the structural stability of thin films; and accordingly, might alter its properties. In the case of ferroelectric thin films, strain effect can manifest themselves in two ways: (i) by shifting phase transition temperature, unit distortion, polarization and dielectric constant; and (ii) by tuning the extrinsic, or dynamic, contributions in the susceptibilities (i.e. piezoelectric and dielectric) via mechanical boundary conditions.

Pertsev et al. have previously reported theoretical studies of Pb(Zr$_{20}$Ti$_{80}$)O$_3$ system. [80,81] They examined the equilibrium polarization states and physical properties of single-domain thin films epitaxially grown on dissimilar cubic substrates by a nonlinear thermodynamic theory. The dependences of the polarization components on the misfit strain at the room temperature were reported. Small-signal dielectric and piezoelectric responses of single-domain PZT films were also determined, and their misfit-strain dependence discussed. As shown in Figure 5.2, on the compression side (Sm<0), as the in-plane strain increases, the paraelectric-ferroelectric (c-phase) transition temperature clearly shifts upward, indicating a more stable c-phase at room temperature. Along with the shift of Tc, the room temperature dielectric constant was predicted to decrease as shown in Figure 5.3(b). The longitudinal piezoelectric coefficient was found to follow the same general trend as the dielectric constant, as can been seen in Figure 5.3(c). In addition, in-plane compression increased the film's tetragonality and induced larger polarizations, as shown in Figure 5.3 (a).
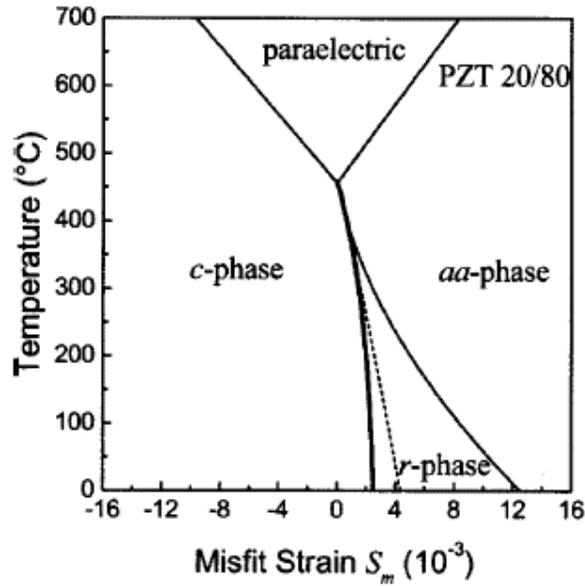
Figure 5. 2 Phase diagrams of (001)-oriented single-domain $Pb(Zr_{20}Ti_{80})O3$ films epitaxially grown on dissimilar cubic substrates. The second- and first-order phase transitions are shown by thin and thick lines, respectively. The triple or quadruple point at Sm=0 corresponds to the Curie-Weiss temperature u(x) of the stress-free bulk material. The dashed line indicates the (Sm ,T) conditions, at which the polarization in the r phase becomes oriented along the cube diagonal of the prototypic unit cell $(P_1=P_2=P_3)$. Figure adapted from Pertsev et al. [80]
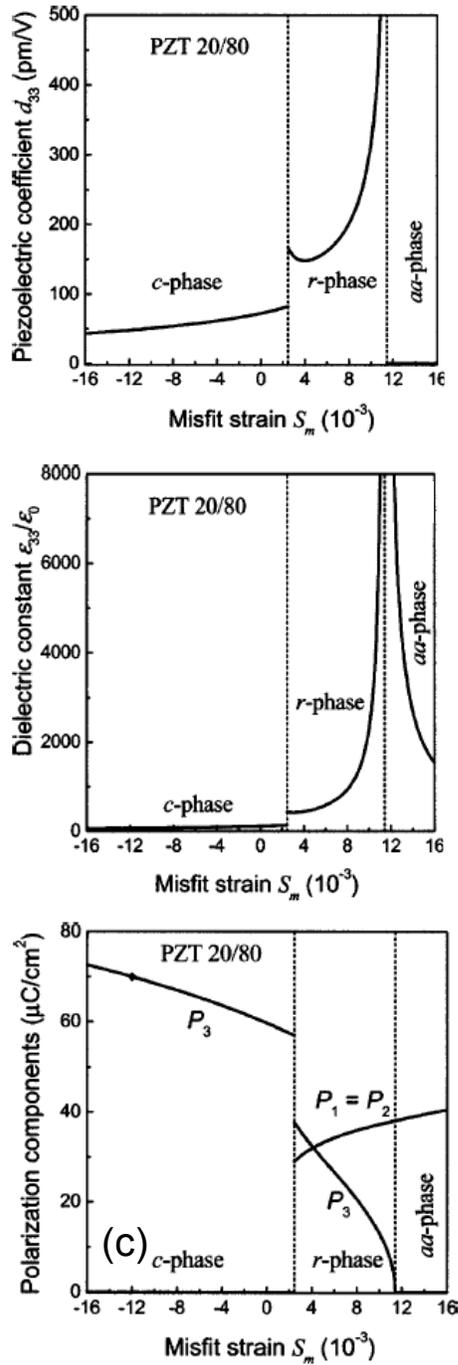
Figure 5. 3 (a) Misfit-strain dependence of the polarization components $P_1 = P_2$ and $P_3$; (b) Out-of-plane dielectric response $\varepsilon_{33}$ calculated; and (c) Piezoelectric coefficient d33 of epitaxial single-domain $Pb(Zr_{20}Ti_{80})O_3$ films calculated as a function of the misfit strain at T = 25 °C. Figure adapted from Pertsev et al. [80]

Strain effects in thin films are studied by varying the film thickness, and by varying heteroepitaxial mismatch by changing substrates. Numerous research activities have previously occurred in this area. As an example, Nagarajan et al. have studied PZT [82] and PMN-PT relaxor thin films [83] by varying the substrates. It was shown for an in-plane tension (MgO substrate) that the stability of a ferroelectric tetragonal structure is reduced and its transition temperature shifted towards lower temperatures. As a consequence, Tc becomes closer to room temperature, and the room temperature dielectric constant increased. On the other hand, in-plane compression (LAO, STO, etc) substrates favor the tetragonal ferroelectric phase, increasing Tc and reducing the room temperature dielectric constant.

In the following sections, details of the ferroelectric characterizations of the variously oriented films will be presented. The thickness dependence will be summarized to exam the strain effects for (001), (101) and (111) oriented films.

### 5.3.1 Electrical properties of (001) $BiFeO_3$ films

Details of the electrical properties for a 200nm $BiFeO_3/SrRuO_3/SrTiO_3(001)$ film with a Pt top electrode are presented in Figures 5.4 (a) and (c). Pulsed polarization measurements were performed, whose operational principle is schematically illustrated in Figure 5.4 (c). A writing pulse was first applied to the sample first to align the polarization into one variant. A positive pulse (P) was then applied to switch the polarization; and the switching current recorded, together with leakage current arising from transport of charged defects. A second positive pulse (U) generates only the leakage current, which subsequently allows for the subtraction from the first current. Theoretically, after this measurements, only the current due to spontaneous polarization is left, which is plotted in Figure 5.4 and 5.5. However, since part of the

charged defects may be lost during the first switch and can not be regenerated in the short pulse delay, the measured leakage current during the second positive pulse could be smaller than it actually is, and consequently, the measured polarization may be larger than the actual value. This effect can be minimized by using short pulse width. Our pulse width dependent measurement ($\Delta P = P^* - P^{\wedge} \approx 2P_r$ where $P^*$ is the switched polarization and $P^{\wedge}$ is the non-switched polarization) down to 1μs revelaed a switchable polarization of ~100 μC/cm$^2$ for (001) oriented BiFeO$_3$ films, which is consistent with the Pr of ~55 μC/cm$^2$ observed in the P-E measurements, see Figure 5.1(a).

In Figure 5.4 (a), the measured pulsed polarization can bee seen to increase with pulse time for t>0.1ms, indicating noticeable leakage current contribution. This is commonly observed in most ferroelectric thin films. Figure 5.4(b) shows the pulsed remanent polarization vs. applied electric field, which was measured using 10μsec wide pulses. A sharp increase of ΔP around 15MV/m can be seen, which reaches a value of ~100μC/cm$^2$ at 55MV/m. This figure also shows that the films had a resistivity of ~10$^9$Ω.cm under zero bias, which is comparable with values obtained for epitaxial Ti-rich lead zirconate titanate (PZT) films. [71] Dielectric breakdown of the films was found with further increase in DC bias to ~40MV/m. This field is somehow lower than the maximum field that can be used in pulse polarization measurement, and it is because that the leakage measurement takes longer time, so the DC bias was applied on the sample for longer time.

Stability of the polar state was characterized with polarization retention conducted over several days, as shown in Figure 5.5. The measurements were done in a closed-loop setup, meaning that the leads were in contact with the capacitor during the measurement period. Electric pulses of 30MV/m were applied to read the
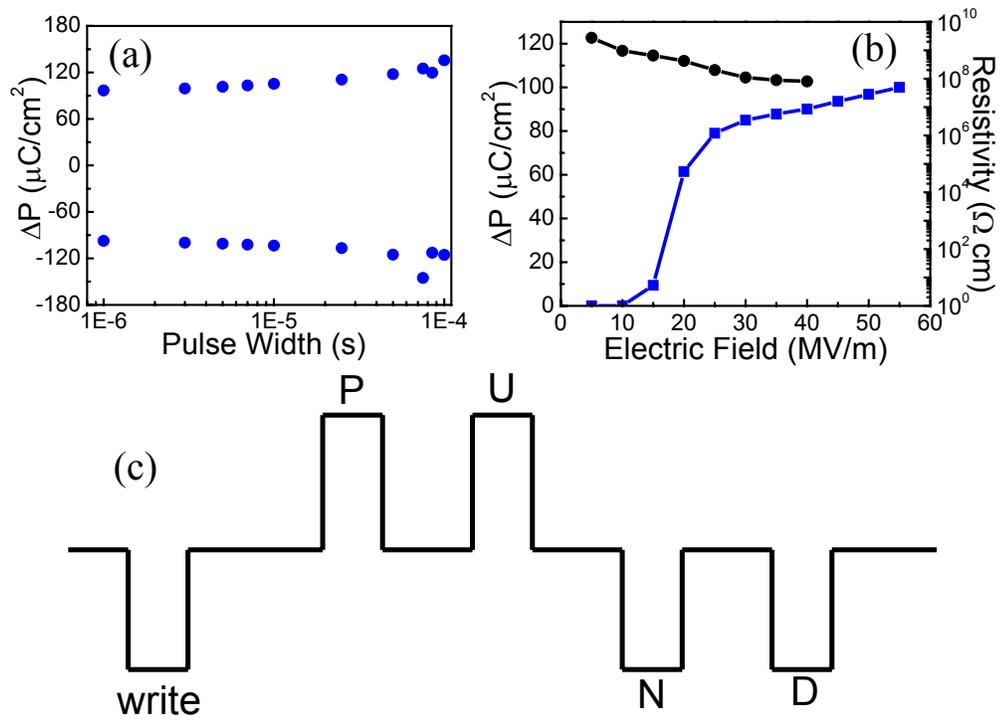
Figure 5. 4 (a) Pulsed polarization vs. pulse width down to 1μs; (b) Pulsed polarization and resistivity vs. applied field results for typical $BiFeO_3$(200nm)/ $SrRuO_3$(20mm)/$SrTiO_3$ (001) sample; (c) Schematic illustration of pulsed polarization measurements process.
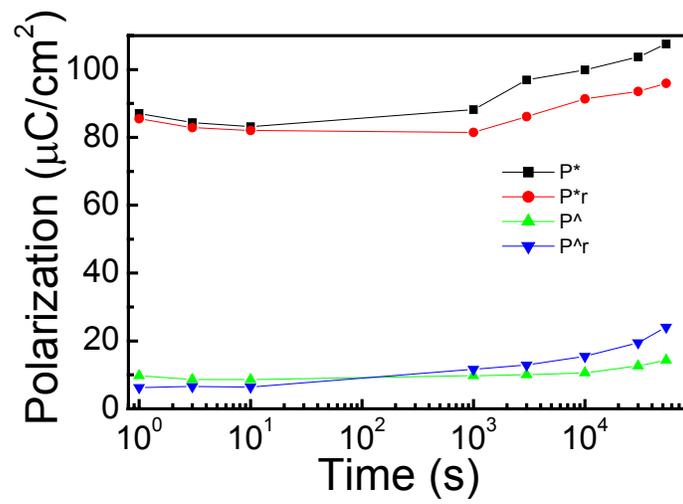
Figure 5.5 Retention measurement for Pt/BiFeO$_3$/SrRuO$_3$/SrTiO$_3$(001) sample, measured at 30MV/m field.

polarization at every time point. The results demonstrate a stable polarization value.

Figure 5.6 summarizes the lattice parameter, P-E loop, small signal dielectric and piezoelectric data for (001) films with different thickness. Inspecting the data will reveal that as the XRD peaks shifted towards higher angles (i.e., smaller lattice d-spacing), (i) both the polarization and coercive field became smaller; and (ii) dielectric constant and piezoelectric coefficients increased. These observations are summarized in Figure 5.7. Only a small portion, $<1\mu C/cm^2$, of the increase in polarization can be attributed to rotation as the unit distorts, if we assume that the absolute value of spontaneous polarization does not change. The observed large increase can only be explained corresponding to the increased tetragonality (c/a), consistent with theoretical prediction by Pertsev et al. [64]

The dielectric constant was measured using a 0.01V peak-to-peak AC sine wave (100 kHz) superimposed with the DC bias. Since $\varepsilon_r$ is related to the piezoelectric electrostrictive coefficient through $d_{33} = 2\varepsilon_0\varepsilon_r Q_{11}P_S$, where $\varepsilon_0$ is the free space permittivity, $Q_{11}$ is the electrostrictive coefficient, and $P_S$ is the saturation polarization. Piezoelectric coefficient is expected to follow the same trend as the dielectric constant. This is confirmed by comparing Figures 5.7 (a) and (b).

For the past few decades, the semi-empirical scaling law, [84,85] $E_c(d) \propto d^{-\frac{2}{3}}$, has been used successfully to describe the thickness dependence of the coercive field in ferroelectric films ranging from 200nm to 100μm. In the derivation of this scaling law, it is implicitly assumed that there are no internal electric fields in the ferroelectric film so that the coercive field measured in the external circuit is identical to that in the film itself. This is true for an ideal capacitor where the electrodes are perfectly conducting and the charge needed to compensate the polarization resides at the film/
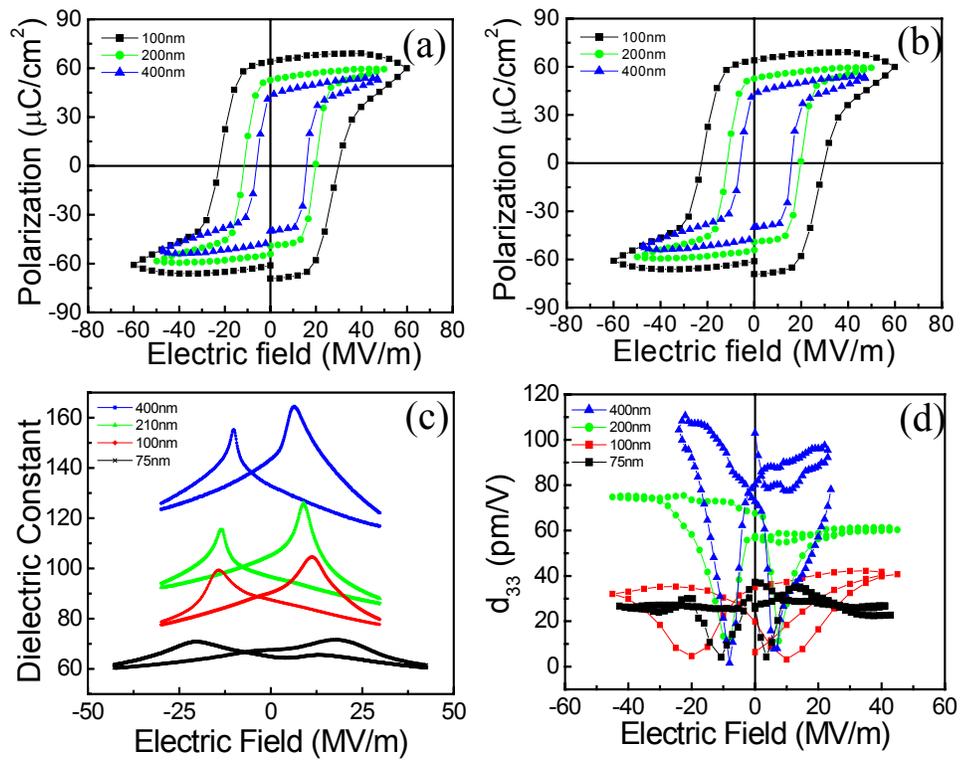
Figure 5. 6 (a) X-ray 2 theta scans, (b) polarization hysteresis loops, (c) small signal dielectric constant, and (d) piezoelectric coefficient of $BiFeO_3/SrRuO_3/SrTiO_3(001)$ samples with different $BiFeO_3$ layer thicknesses.
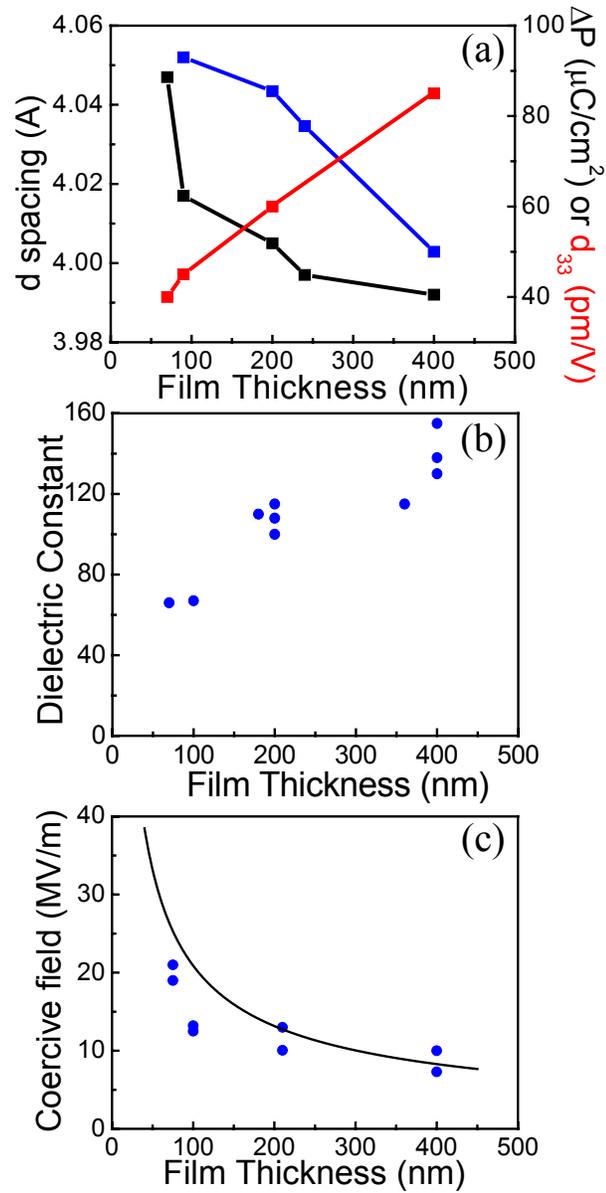
Figure 5. 7 (a) Summary of out-of-plane d spacing, pulsed switched polarization and piezoelectric coefficient vs. films thickness. Thickness dependence of (b) small signal dielectric constant and (c) coercive field taken from dielectric constant, and fitting curve using $E_c(d) \propto d^{-\frac{2}{3}}$.

electrode interface in a negligible thickness. [86] In reality, screening charges in the electrode are always distributed over a small but finite region, resulting in incomplete compensation. For a ferroelectric capacitor measured in short-circuit setup, this spatial charge distribution leads to a voltage drop in the electrode and a corresponding depolarization field in the film to ensure that the whole circuit is equipotential. Since P generally does not depend on film thickness beyond the nm scale, this depolarization field will simply scale as 1/d and will becomes more important at small thickness, resulting in a small measured coercive field. As shown in Figure 5.7 (c), the fitted curve and the measured coercive fields indicate good fitting at larger thickness. But, the measured results indeed show divergence at smaller films thickness, indicating depolarization field effect due to uncompleted compensation.

### 5.3.2 Electrical properties of (101) and (111) oriented BiFeO$_3$ films

Pulse polarization results for (101) and (111) oriented films are shown in Figure 5.8. The polarization responses over the pulse width of $10^{-6}<t<10^{-4}$ sec were nearly flat, indicating negligible contribution from leakage current to the polarization. Field dependent pulse measurements revealed domain switching near E=18MV/m and 22MV/m for (101) and (111) films, respectively. This is consistent with the values for the coercive fields deduced from dielectric and piezoelectric coefficients measurements. However, resistivities of the (101) and (111) oriented films were somewhat lower than that of (001) films: $\sim 1\times10^{9}\Omega\cdot cm$ and $\sim 3\times10^{8}\Omega\cdot cm$ respectively, even though TEM analysis revealed that the (111) and (101) films were of notably better epitaxy than (001) ones. It is also shown in Figure 5.8 (c) and (d) that (111) and (101) films have much smaller dielectric breakdown fields, as revealed by the resisitivity vs. E results. Theoretically, BiFeO$_3$ is predicted to be

semiconducting, and accordingly the intrinsic resisitivity will depend on the strength of the correlation in this material. For standard values of on-site correlation (i.e., choice of U parameter), theory predicts band gaps between 1.2 and 1.9 eV [private comm with Jeff], which is much smaller than typical perovskite ferroelectrics values of 3-4 eV, but higher than typical semiconductor values. However, since the states near the Fermi level are the O p and Fe d orbits, it can be speculated that appreciable effective masses may result, reducing the conductivity over typical semiconductors. Future measurements are needed to confirm the specific details. Nevertheless, the resistivity of $BiFeO_3$ is likely between semiconductor and typical perovskite ferroelectrics. The small band gap might be the reason for an inability to fully switch the polarization in bulk samples.

Ferroelectric hysteresis loops and dielectric responses of $BiFeO_3$ thin films with different thickness grown on (101) and (111) oriented substrates are summarized in Figure 5.9. Unlike (001) films, the spontaneous polarizations along (101) and (111) do not show a distinct thickness dependent within the rang studied. This is consistent with the reduced lattice distortion observed by XRD for these orientations. However, decrease of coercive field with increasing film thickness was still observed. Due to a low resistivity and dielectric breakdown strength, the P-V characteristics of the (101) and (111) films could not be measured for thickness below 100nm.
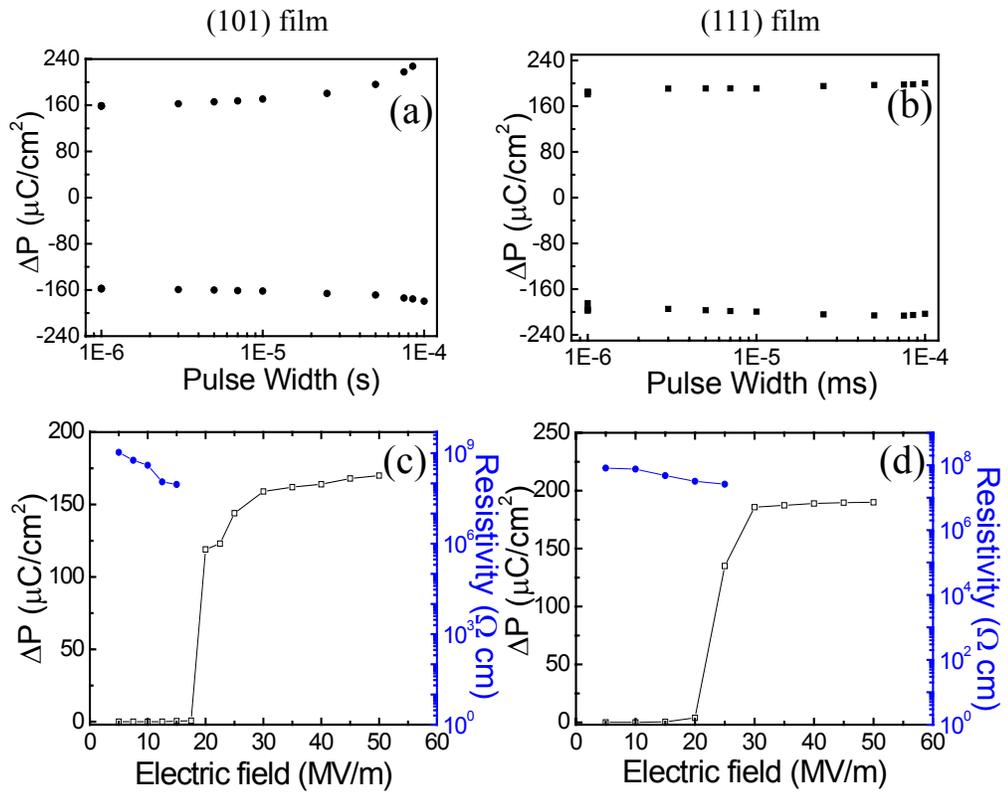
Figure 5. 8 (a, b) Pulsed polarization vs. pulse width; (c, d) resistivity and pulsed polarization vs. applied field for typical BiFeO$_3$/SrRuO$_3$/SrTiO$_3$(101), (111) with 200nm BiFeO$_3$ layer.
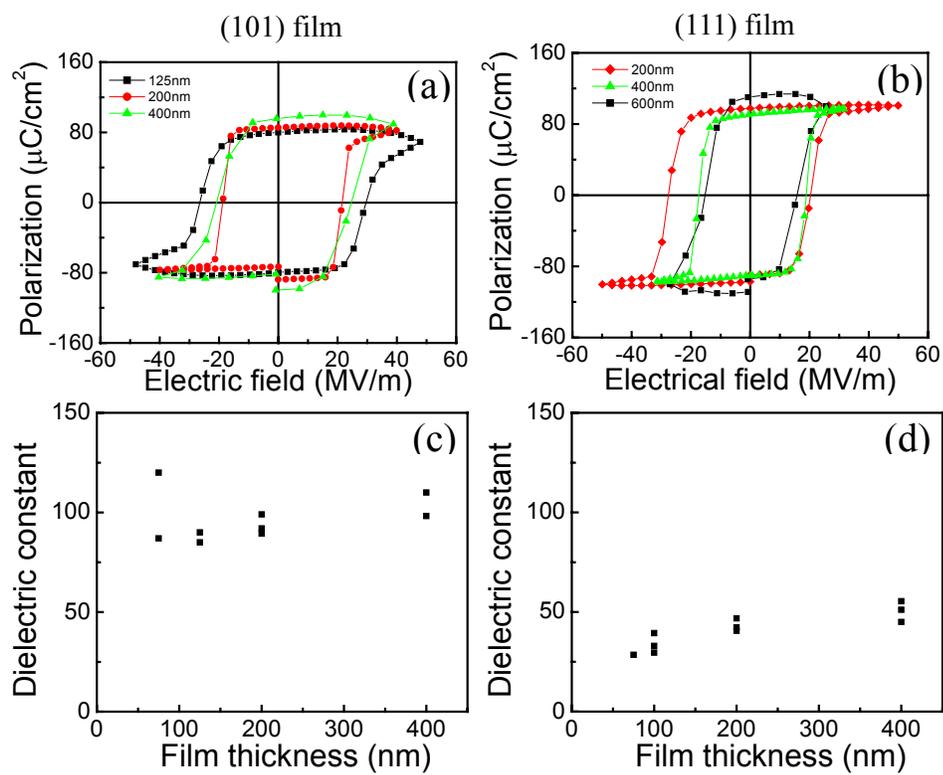
Figure 5. 9 Summary of the P-V responses and dielectric constants of (101) (a, c) and

(111) (b, d) oriented BiFeO₃ films with different thickness.

## 5.4 Summary

To summarize, the electrical properties of BiFeO$_3$ thin films with reasonably high resistivies ($\sim 10^9 \Omega$cm at zero bias) have been studied. We have found

(i)     that the easy axis of the spontaneous polarization of BiFeO$_3$ lies along the (111) direction in (001), (101) and (111) oriented films, this is in spite of the fact that the (001) and (101) films were distorted from the rhombohedral symmetry. It is important to note that the spontaneous polarization was $\sim 100 \mu$C/cm$^2$ along (111), which was corroborated by theoretical calculations. This value is much higher than prior results, but I believe is likely the intrinsic spontaneous polarization of BiFeO$_3$.

(ii)    the values of the polarization, dielectric constant and piezoelectric coefficient for 200nm BiFeO$_3$ layers oriented along the (001), (101) and (111); as summarized in Table 5.3.

Table 5. 3 Summary of electrical properties of typical BiFeO$_3$ 200nm layers grown on (001), (101) and (111) oriented substrates.

|  | (001) | (101) | (111) |
|---|---|---|---|
| Polarization ($\mu$C/cm$^2$) | 55 | 80 | 100 |
| Dielectric constant, $\varepsilon_r$ | 100 | 85 | 40 |
| Piezoelectric coefficient (pm/V) | 60 | 45 | 20 |

# CHAPTER 6, MAGNETIC PROPERTIES OF BiFeO$_3$

# THIN FILMS

The magnetic point group of BiFeO$_3$ is 3m, and the Neel temperature $T_N = 400°C$. The magnetic structure has a 3-fold rotation axis along $[001]_h$ and a mirror plane m along $[110]_h$. Early neutron diffraction studies [87] have revealed that BiFeO$_3$ possesses the antiferromagnetic ordering of the G type, where every $Fe^{3+}$ is surrounded by six ions with oppositely oriented spins. The $Fe^{3+}$ magnetic moments are coupled ferromagnetically within the pseudo-cubic $(111)_c$ planes and antiferromagnetically between adjacent planes.

In perovskite oxides, direct spin-spin interaction does not exist. Rather, interactions are mediated by a so-called "superexchange" mechanism. Essentially, the spin moments of the $Fe^{3+}$ ions on the opposite side of $O^{2-}$ interact with each other via the oxygen p-orbit electrons. If the spins are oriented perpendicular to the $[111]_c$ direction (as predicted by first principle calculation [88] and supported by previous experimental observation [89]), the symmetry also permits a canting of the antiferromagnetic sublattices, resulting in a macroscopic magnetic moment: the so-called weak ferromagnetism.

In fact, precise measurements performed using a time-of-flight neutron diffractometer [90,91] have revealed a quite complicated magnetic structure. The antiferromagnetic ordering possesses a spiral spin modulation with a large period of $\lambda = 620 \pm 20$ Å, which is also incommensurate with the fundamental lattice. Accordingly, the magnetic moments of the iron ions retain their local mutually antiferromagnetic G-type orientation and rotate along the propagation direction of the modulation wave in the plane perpendicular to the hexagonal basal plane. The wave

vector of such a cycloid is perpendicular to the threefold axis and lies in the plane of spin rotation. The existence of the incommensurate cycloidal structure has also been confirmed by line-shape analysis of nuclear magnetic resonance (NMR) spectra [92,93]. Theoretical analysis has been performed to explore the physics for the formation of such a structure. [94]

Because of the cycloidal modulation, the net magnetization due to spin canting within each pair of $Fe^{3+}$ ions and the volume-averaged magnetoelectric (ME) effect are averaged to zero over a wavelength. [95] This means that the spontaneous magnetization of bulk single crystal $BiFeO_3$ should be zero even though its symmetry permits weak ferromagnetism. Indeed, a linear magnetization (M) vs. field (H) curve has been observed from a single crystal sample, as shown in Figure 6.1. Most of the early work on $BiFeO_3$ could be found in references. [96,97,98]

The purpose of this chapter is to show how the magnetic properties of these highly resistive $BiFeO_3$ epitaxial films are altered with respect to the bulk specimen. This part of the work is conducted in collaboration with Feiming Bai at Virginia Tech. Specifically, we have (i) <u>consistently</u> found a weak ferromagnetism with a spontaneous magnetization of <u>no</u> less than 5 emu/cc; (ii) <u>sometimes</u>, found a significant excess magnetization of ~80 emu/cc in ultra thin films; and (iii) measured the anisotropy of this magnetization.

## 6.1 Magnetic properties of $BiFeO_3$ thin films

### 6.1.1 Magnetization in $BiFeO_3$ thin films

In sharp contradictory to bulk single crystals, slim hysteresis loops typical of weak ferromagnetic materials were observed for our $BiFeO_3$ thin films. Again, highly resistive 200nm $BiFeO_3$ thin films grown on (001), (101) and (111) oriented $SrTiO_3$

substrates with $SrRuO_3$ bottom electrodes were studied. Figure 6.1 (a) shows the in-plane M vs. H responses for all three orientations. Also shown in the figure is the curve from a bulk single crystal sample, shown in open circle. The magnetic field was applied in-plane, along (100) for the (001) film, and (110) for the (101) and (111) ones. We can summarize several interesting features concerning these results, which are

(i)      films for all three orientations exhibited magnetic hysteresis behavior, with high field susceptibilities similar to that of single crystals;

(ii)     slim hysteresis loops with essentially zero remnant magnetization and no coercive field; and

(iii)    saturation magnetizations of ~15 emu/cc, ~7.5 emu/cc and ~5.5 emu/cc for (001), (101) and (111) films, respectively.

The results clearly reveal different magnetic behavior for these highly resistive $BiFeO_3$ thin films, relative to that of single crystal. The observed slim hysteresis loops were similar to those observed in superparamagnetic materials. [99] However, unlike a super- paramagnet that exhibits normal M vs. H loops below a blocking temperature, we found nearly identical slim curves for the $BiFeO_3$ films at T=5K, 300K, as seen in Figure 6.1 (b) for a $BiFeO_3/SrTiO_3$(001) specimen.

Samples without electrode were studied to insure that the enhanced magnetization was not from the $SrRuO_3$ electrode, which becomes ferromagnetic at temperature ~160K. [100] The results showed that the saturation magnetization was similar for films with and without electrodes, but higher at lower temperatures. However, the main characteristics remain unchanged, including the enhanced remnant magnetization, a low coercive field, and slim M-H curve. Figure 6.2 shows the M-T behavior of specimen with/without $SrRuO_3$ electrodes, over the range of 5<T<300K.
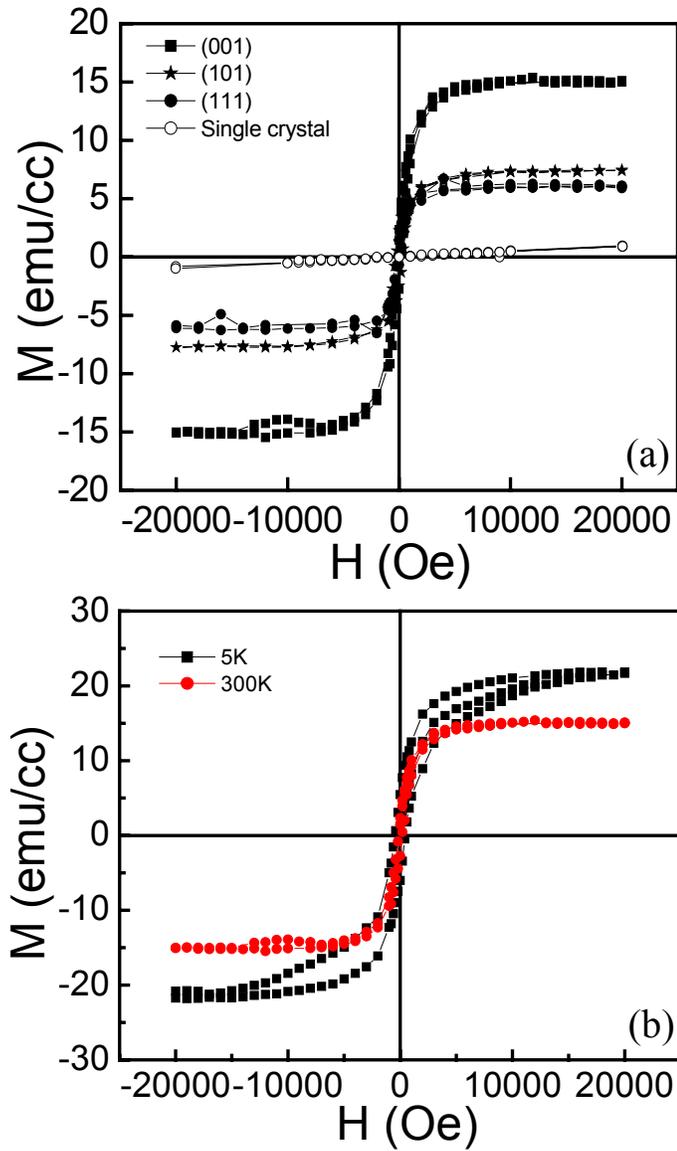
Figure 6. 1 (a) M vs. H for BiFeO$_3$ thin films (200nm) grown on SrTiO$_3$ (001), (101)

and (111) substrates. The SrRuO$_3$ electrodes are ~20nm thick. (b) M vs. H at 5k and

300k for (001) BiFeO$_3$ films.
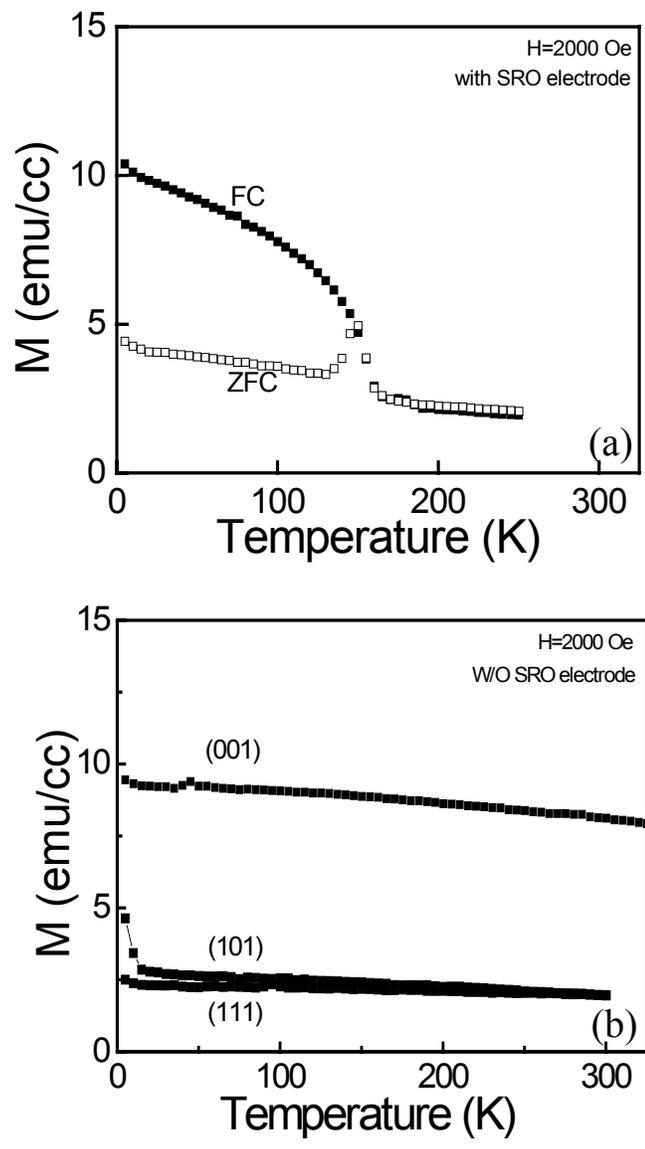
Figure 6. 2 M vs. T response for 200nm BiFeO$_3$ thin films (a) grown on SrTiO$_3$(111)

with 15nm SrRuO$_3$ and (b) on SrTiO$_3$(001), (101) and (111) without SrRuO$_3$.

Field cooling (FC) and zero field cooling (ZFC) responses for samples with $SrRuO_3$ electrodes, see Figure 6.2(a), demonstrate a ferromagnetic phase transition for $SrRuO_3$ near 160K. This is consistent with prior reports. [100] Field cooling measurements of $BiFeO_3$ films grown directly on $SrTiO_3$ were also performed in under a DC bias of $10^3$ Oe. A smooth change in magnetization was observed for all three orientations, as seen in Figure 6.2(b). The decrease in magnetization values from (001) film to (101) and (111) ones is consistent with the slope of the M-H curves of Figure 6.1.

We also noticed that all three films show saturation behavior above 2000Oe. However, the saturation magnetizations along these three directions did not coincide at higher field. [Please note that during the in-plane measurement, the magnetic field is along (100) for (001) film, and (110) for both (101) and (111) films.] If the difference in magnetization was solely due to crystal anisotropy, we would expect the M-H curves for the various orientations to eventually meet at higher field. However, this was not fund to be the case, indicating an intrinsic difference in the magnetization between variously oriented films.

To further exploit the magnetic anisotropy of $BiFeO_3$ thin films, we performed M-H studies with fields applied in-plane along both the (100) and (110) directions, which was done by rotating the $BiFeO_3/SrTiO_3$(001) sample by 45°; as well as with field applied in-plane along (100) and out-of-plane along (001). These results are shown in Figure 6.3. No clear difference was observed for fields applied along (001), (110) or (100) in this particular case: the low field susceptibilities and saturation magnetizations remain the same.
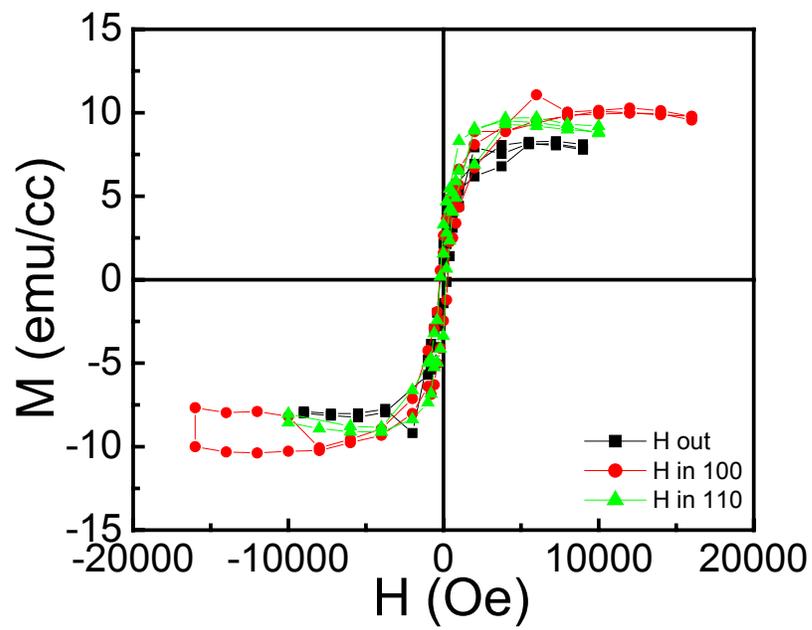
Figure 6. 3 In-plane vs. out-of-plane M-H response for a (001) oriented BiFeO$_3$ film.
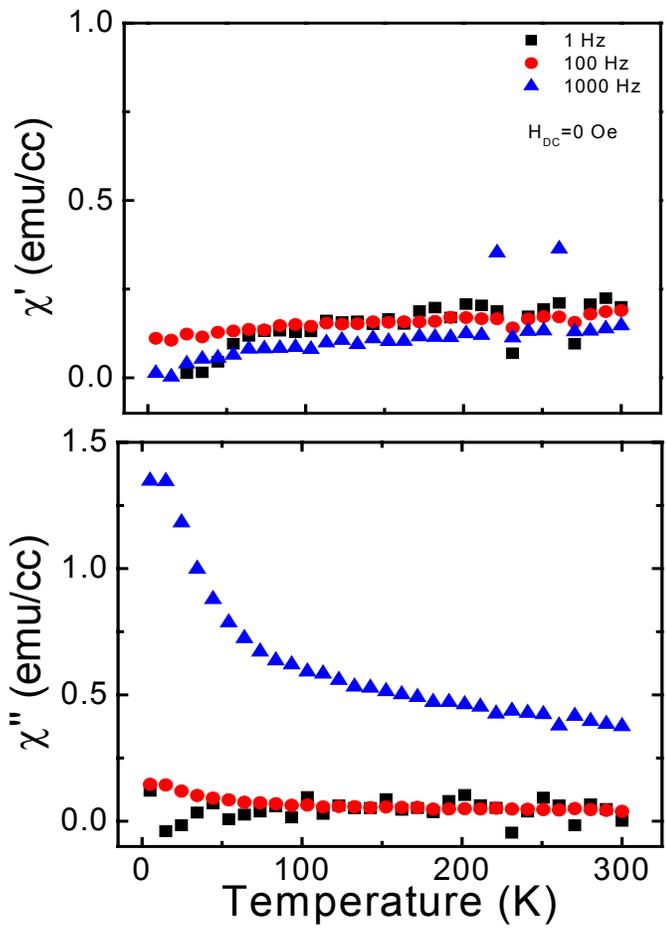
Figure 6. 4 Magnetic susceptibility χ' and χ'' of BiFeO$_3$(90nm)/SrTiO$_3$(001) under 0 DC field. [Data taken in collaboration with Naigang Wang.]

Temperature dependent susceptibility measurements have proven to be very powerful in characterizing magnetic phase transitions. We performed these characterizations on both (001) and (111) oriented $BiFeO_3$ thin films. As shown in Figure 6.4 for the $BiFeO_3/SrTiO_3(001)$ sample, no phase transition was observed between 5k and 300k, consistent with the high Neel temperature of $BiFeO_3$. The slight decrease of $\chi$' with decreasing temperature is consistent with the antiferromagnetic nature of $BiFeO_3$.

### 6.1.2 How do we understand the magnetic property of $BiFeO_3$ thin films?

The key to understand the magnetization of $BiFeO_3$ thin films lies in the fact that magnetic structure can be perturbed by external forces, e.g. (i) high magnetic field; (ii) elastic constraint; and/or (iii) chemical doping. [101,102,103] This means that weak ferromagnetism of $BiFeO_3$ can be released by external perturbation upon destruction of the cycloidal spin structure. Recent high field experiments on $BiFeO_3$ single crystal revealed interesting results in this manner. [104,105] Ruette et al performed [104] electron spin resonance (ESR) measurements under a wide range of magnetic field of 0<H<25T. Dramatic changes in the ESR spectra were observed, as shown in Figure 6.5. A low field spin resonance mode that had linear relationship between resonance frequency, $\upsilon$, and magnetic field, H, was observed, which had a slope of ~27 GHz/Tesla and a slope intercept of zero. This mode is attributed to the incommensurate cycloidal spin structure. For H>18T, a secondary spin resonance mode was observed that had a linear relationship between $\upsilon$ and H. The slope of this secondary mode was 13GHz/Tesla, ~1/2 of that of the low field one. A theoretical approach was then developed to understand the nature of the second resonance mode, which evidences supported the phase transition from a cycloidal spin structure to a
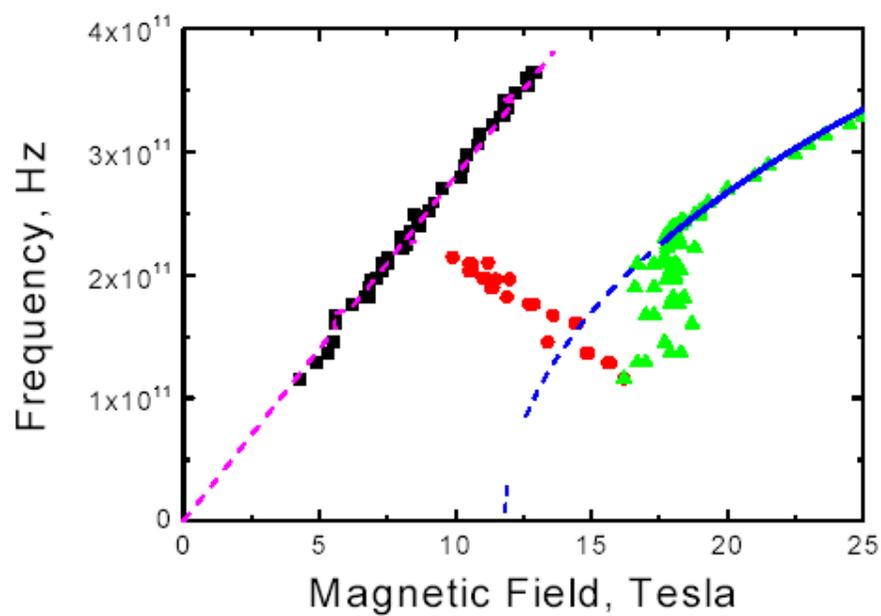
Figure 6. 5 Electron spin resonance frequency as a function of magnetic field H. The abnormal behavior of f vs. H between 10 to 18T indicates a transition between different magnetic states. Figure adapted from Ruette et al. [104]

spatially uniform one.

Additional experiments in support of an induced cycloidal to homogeneous spin order under high field was reported by Kadomtseva et al. [106], who observed a magnetic transition of $BiFeO_3$ at high magnetic field of ~20T. This was illustrated by a sudden jump of magnetization, as shown in figure 6.6. Extrapolating the high field M-H curve down to zero field yields a moment of ~2-3 emu/cc, which is smaller than, but of the same order of that predicted by spin canting.

The net magnetization of $BiFeO_3$ in a uniform antiferromagnetic state can be estimated based on the unit cell volume and spin-canting angle. Assuming a canting angle of 0.8 degree [88], and an effective magnetic moment of iron ions in $BiFeO_3$, 3.75; [107] the net magnetization of a spatially uniform spin structure should be ~ 8emu/cc. This value is larger than that of crystals under high field. The difference may be due to that the canting angle of adjacent $Fe^{3+}$ ions is not uniform within the whole sample.
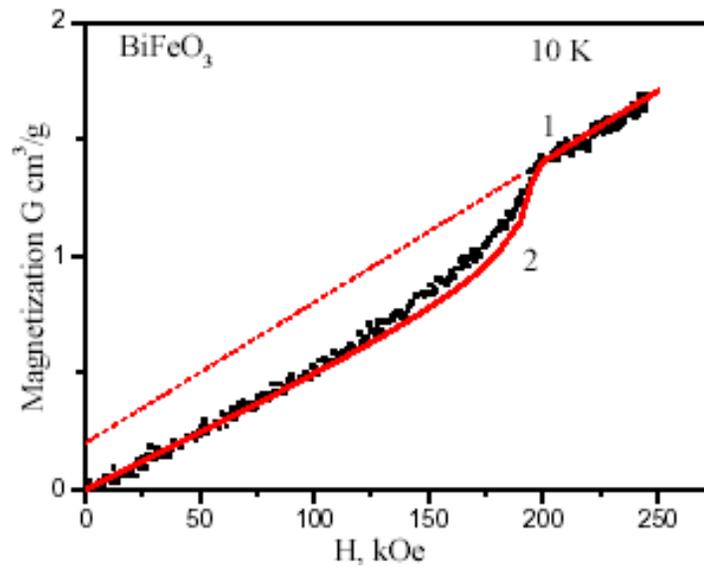
Figure 6. 6 The field dependence of BiFeO₃ magnetization at 10K. (1) experimental curve with field oriented along the pseudo-cubic (001) direction, (2) theoretically calculated curve. Figure adapted from Kadomtseva et al. [106]

The results of Figures 6.1-6.3 show that epitaxial thin films under a field of $H \leq 0.2 Tesla$ have magnetizations higher than that of bulk crystals under H>20Tesla. In addition, theses results reveal that films have similar high field magnetic properties relative to bulk single crystal, but have dramatically enhanced weak field permeabilities: the permeability of the films is dramatically changed, but not their magnetizations. Accordingly, the uniform antiferromagnetic spin state is intrinsically stable in thin films.

Now the question is what breaks the cycloidal spin structure in thin films? According to Dzyaloshinskii and Moriya, [108,109] the long range modulation and spin canting in a magnetic system are caused by an antisymmetric spin coupling, the so-called DM interaction. Materials of this type have been studied extensively. [110,111] It has been established that the superstructure arises as a result of instability of the ordered phase against interactions of the spin-lattice and spin-spin types. Theoretical analysis has confirmed that weak ferromagnetism will not happen without spin-orbit coupling. [88] It is also shown by using thermodynamic analysis that a phase transition from the cycloidal to the homogeneous anitferromagnetic spin state will occur at a critical value of the perturbation $K_{pert}^c$, when the energy of the cycloidal state is equal to that of the homogeneous one. [104] In case of BiFeO$_3$, this will occur when the anisotropy constant fulfills the critical perturbation condition of

$$K_{pert}^c > \frac{(\gamma \cdot P_s)^2}{2A} + K_u - \chi_\perp \frac{(\beta \cdot P_s)^2}{2} \approx 2x10^6 \frac{erg}{cm^3} = 2 \cdot 10^5 \frac{J}{m^3} \, ;$$

One of the perturbation sources in thin film systems is the epitaxial constraint of substrates. We can roughly estimate the elastic energy coming from the substrate in BiFeO$_3$ thin films. The Young's modulus is taken as Y=10$^{11}$ N/m$^2$, by comparisons with other complex ferroelectric perovskites. [112] The calculated elastic energy

is $E_{Elastic} = \frac{1}{2} Y\varepsilon^2 \approx 2 \times 10^5 \frac{J}{m^3}$, assuming a strain of 0.2% which is easily achievable

in epitaxial thin film. As shown in Chapter 4, strain >0.2% persists in all the thin

films up to 400nm. It is clear that epitaxial constraint is large enough to destruct the

cycloidal spin structure of $BiFeO_3$.

### 6.1.3 Thickness dependence of the magnetic properties

To further understand the magnetization in $BiFeO_3$ thin films, we deposited films

with thickness ranging from 30nm to 300nm. The M-H characteristics of these films

were measured. Films with and without $SrRuO_3$ bottom electrodes were also compared

to determine the possible buffer-layer effect. Figure 6.7-6.9 show a summary of M-H

curves for (001), (101), and (111) films of various thickness.

Observations can be summarized as follows:

(i)     for thickness of ~300nm, the magnetization of all three orientations saturate

        at ~5emu/cc. This is close to the estimated bulk value of the uniform

        antiferromagnetic state, indicating the destruction of spin cycloid by film

        constraint;

(ii)    as the thickness is decreased, the saturation magnetization is increased;

(iii)   for film thickness less than 100nm, a large variation in the saturation

        magnetizations was observed, even among samples deposited under

        seemingly identical conditions (i.e., within experimental controllability).

        The variation was largest for (001) oriented films: Ms of ~80emu/cc was

        observed for some samples (indicated in Figure 6.7 as situation 1), whereas

        ~15emu/cc was observed for others (see situation 2). Similarly, for (101)

        oriented films, Ms was found to vary between ~30emu/cc and
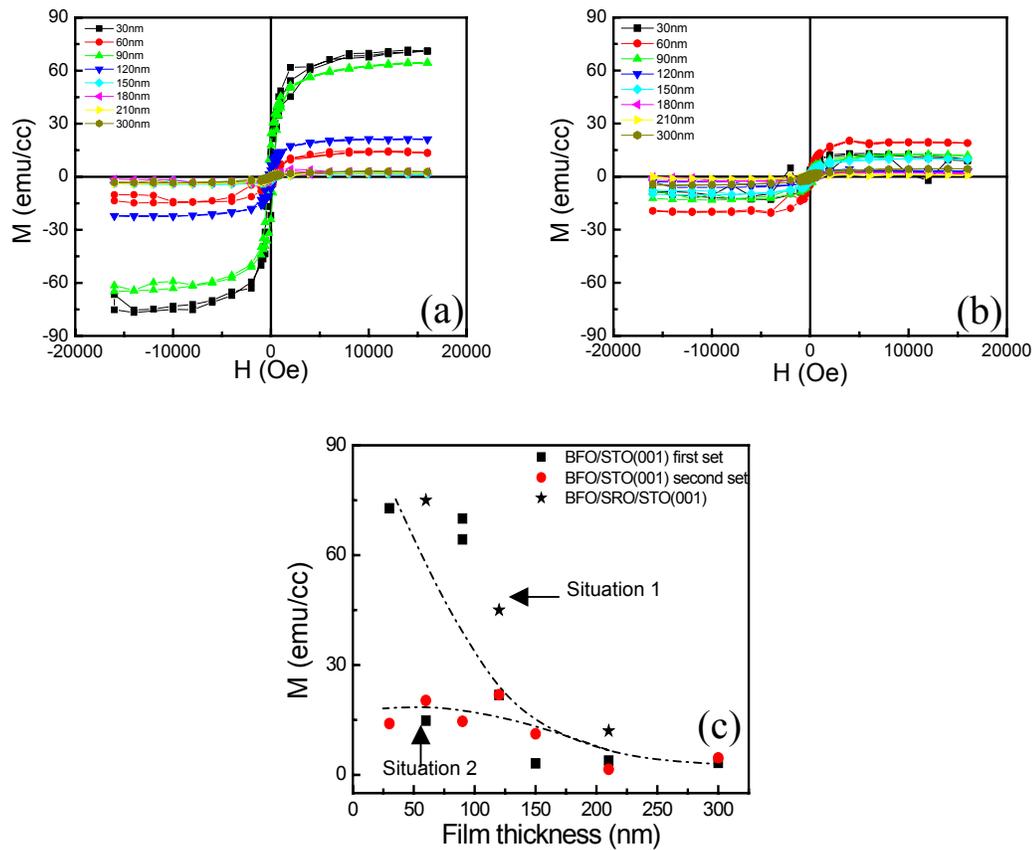
Figure 6. 7 M vs. H loops for $BiFeO_3/SrTiO_3(001)$ from (a) first set and (b) second set

of samples. (c) Summary of saturation magnetization vs. film thickness. The lines are

used to guide eyes. [Data taken in collaboration with Feiming Bai.]
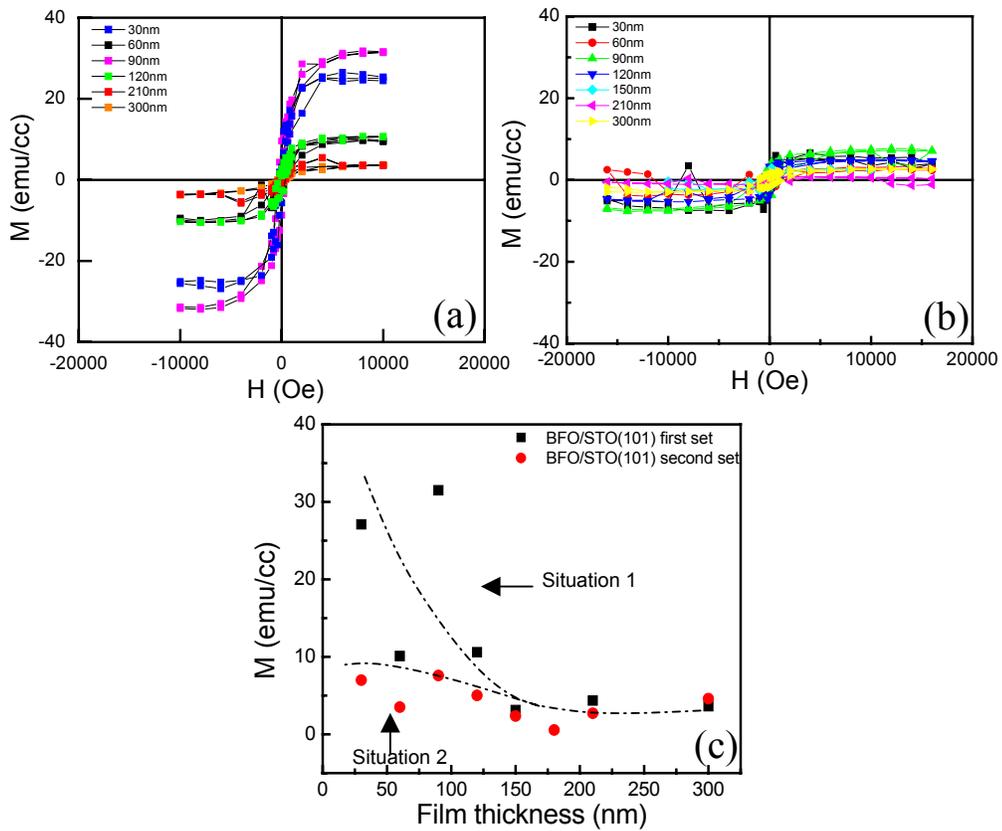
Figure 6. 8 M vs. H loops for BiFeO$_3$/SrTiO$_3$(101) from (a) first set and (b) second set of samples (c) Summary of saturation magnetization vs. film thickness. The lines are used to guide eyes. [Data taken in collaboration with Feiming Bai.]
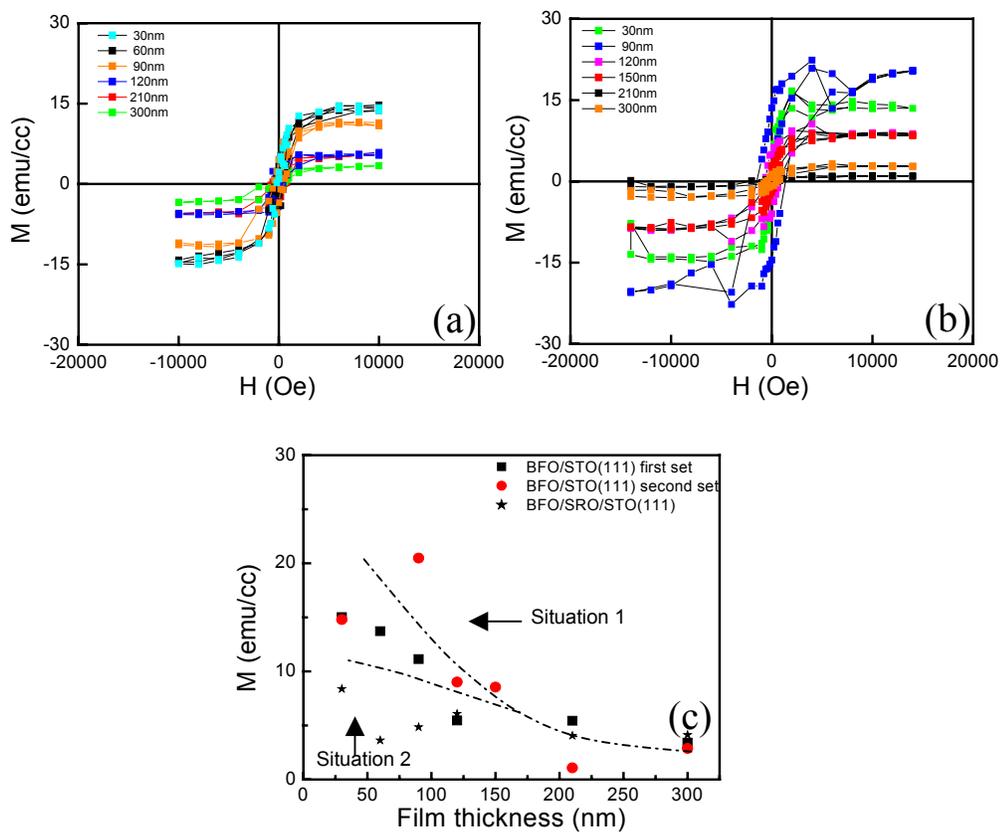
Figure 6. 9 M vs. H loops for $BiFeO_3/SrTiO_3(111)$ from (a) first set and (b) second set of samples (c) Summary of saturation magnetization vs. film thickness. The lines are used to guide eyes. [Data taken in collaboration with Feiming Bai.]

~10emu/cc, as shown in Figure 6.8; and for (111) oriented films, between

10emu/cc and 20emu/cc as shown in Figure 6.9; and

(iv)     in case of situation 1, the observed specific higher values of Ms follow the

same trend as out-of-plane lattice parameters, indicating a possible role of

epitaxial strain.

It is relevant at this point to note that interactions between neighboring $Fe^{3+}$ ions,

the so-called superexchange interaction, is very sensitive to the $Fe^{3+}$-$Fe^{3+}$ spacing and

the bond angle. [113] Accordingly, it might be expected that with lattice parameter

changes, that the two other structural aspects are altered. This would then perturb the

magnetic interaction, and possibly result in the manifestation of changes in the

macroscopic magnetization.

Further evidence supporting the possible role of epitaxial strain on magnetic

property of $BiFeO_3$ thin films is given in Figure 6.10. The low field regions of the M-

H responses of $BiFeO_3$/$SrTiO_3$(001) samples with 30nm, 150nm, 210nm $BiFeO_3$

layers are shown in this figure. As Ms decreased with increasing film thickness, the

coercive field and the remanent magnetization were found to increase. Similar

features were observed when comparing films grown on $SrRuO_3$ buffer layers with

those grown directly on $SrTiO_3$, see Figure 6.10 (b). This similarity can be understood,

since both film thickness and a buffer layer will effectively reduce the epitaxial stress

in the $BiFeO_3$ layer. However, the physics behind the observation is still unclear.

Based on the above observations, a model can be conjectured to explain the

magnetic properties of $BiFeO_3$ thin films. At larger film thickness (>300nm), the

cycloidal spin modulation of the antiferromagnetic order is destroyed. However, the

canting angle between neighboring $Fe^{3+}$ spins remains unchanged. This yields a

minimum saturation magnetization of ~5emu/cc, which is independent of the film
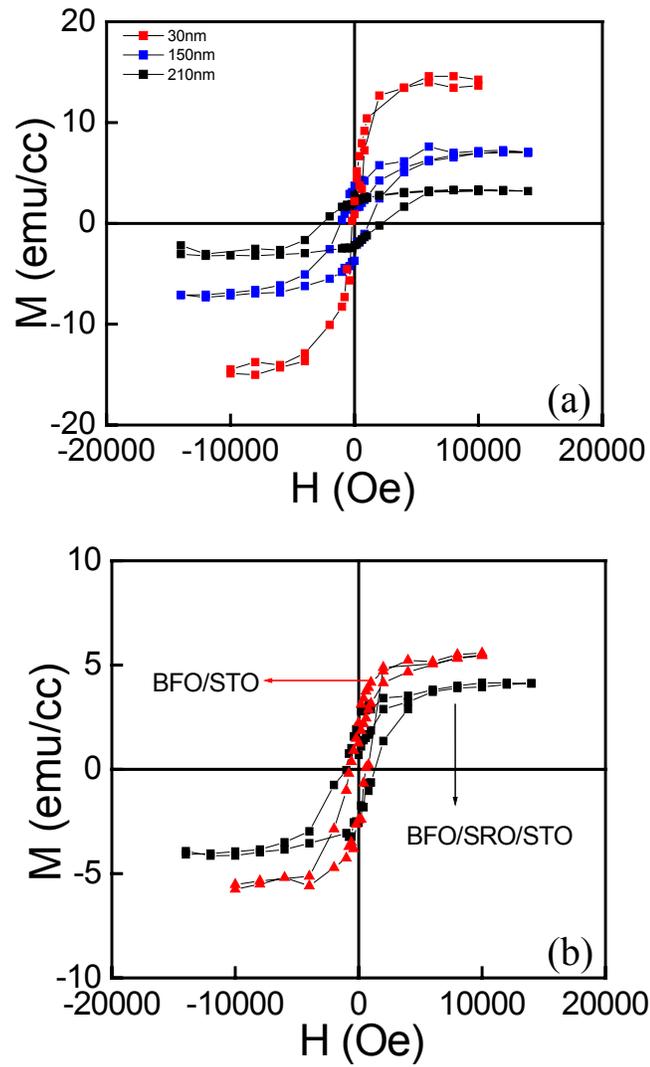
Figure 6. 10 (a) M vs. H responses of BiFeO$_3$/SrTiO$_3$ (111) samples with BiFeO$_3$ layer of 30nm, 150nm, and 210nm thick. (b) M vs. H loops for 210nm BiFeO$_3$ films grown directly on SrTiO$_3$ substrate and with SrRuO$_3$ electrode. [Data taken in collaboration with Feiming Bai.]

orientation. The destruction of the spin cycloid may be induced by epitaxial strain, or possibly finite size effects. It is quite surprising that strain effect may persist to films of >200nm thickness. In fact, strains of ~0.2% were observed by XRD for $BiFeO_3$ films up to 400nm. Phenomenological estimations of Section 6.1.2 suggest that this elastic energy is sufficient to destroy the cycloidal spin structure. Note that this strain is not necessarily due to epitaxial stress. Oxygen vacancies could also induce large unit size.

Another possibility is size effect. When the sample thickness becomes comparable to that of the modulation length, ~ 60nm for $BiFeO_3$, the modulated structure may become unstable due to dimensional limitations. Clearly, further theoretical study in this area is needed.

However, it is not completely clear why the magnetization was variable from film to film, as can be seen by comparing the two situations indicated in Figure 6.7-6.9. It is important to note that we find a minimum Ms of ~ 5emu/cc, nearly equal to the homogeneous magnetic state value. Large variation in the observed saturation magnetization from film to film may result from an extreme sensitivity to deposition condition, which we have not yet successfully identified. It should be noted that there is a certain level of uncontrollability in thin film deposition by PLD. The possibility that second phase (e.g. $Fe_3O_4$) contributes to the large observed magnetization can not be completely ruled out. If the second phase forms nano sized particles in the films, it will be very difficult for XRD and/or TEM to distinguish them.

### 6.1.4 Mont Carlo Simulation: Role of magnetoelectric coupling

The above discussion does not take into account the effect of the coupling between the electric and magnetic orders that coexist in multiferroics. Unlike in other materials, the internal electric field resulting from the spontaneous polarization of multiferroics could act on the magnetic sublattice. Scientists have been trying to understand the coupling fundamentally and by using microscopic simulation. The earliest theoretical work traced back to 1959 when Landau and Lifshitz predicted the possible existence of magnetoelectric (ME) effect in some ordered magnetic materials. An allowed term in the free energy of the form $\alpha_{ij} H_i E_j$ shows the correlation between H and E. [114] While nonlinear ME effect can occur in any materials (not necessarily magnetically ordered), ferroelectromagnetic materials differ from the others in that they show a spontaneous ME effect in addition to the effects induced by external fields. It is caused by the existence in the crystal of spontaneous electric and magnetic moments. This phenomenological approach constituted the starting point for the subsequent theoretical works. [115,116]

It is now understood that the ME effect originates from symmetry breaking of an AFM crystal or spin canting in AFM or FM crystals by applying an electric field, external applied or internal field arising from the spontaneous polarization. Liu et al. performed a series of simulations [117]. The results provide interesting features about the phase transitions of a FE-AFM system, which could contribute to our understanding of the observations in $BiFeO_3$ thin film system. The Mont Carlo simulation was based on the Janssen model [118]. The most relevant result is cited in Figure 6.12, where simulated magnetization, magnetic susceptibility, polarization and ME susceptibility are plotted as a function of temperature. Two interesting points are readily seen: (i) With large coupling coefficient, a phase transition into ferromagnetic
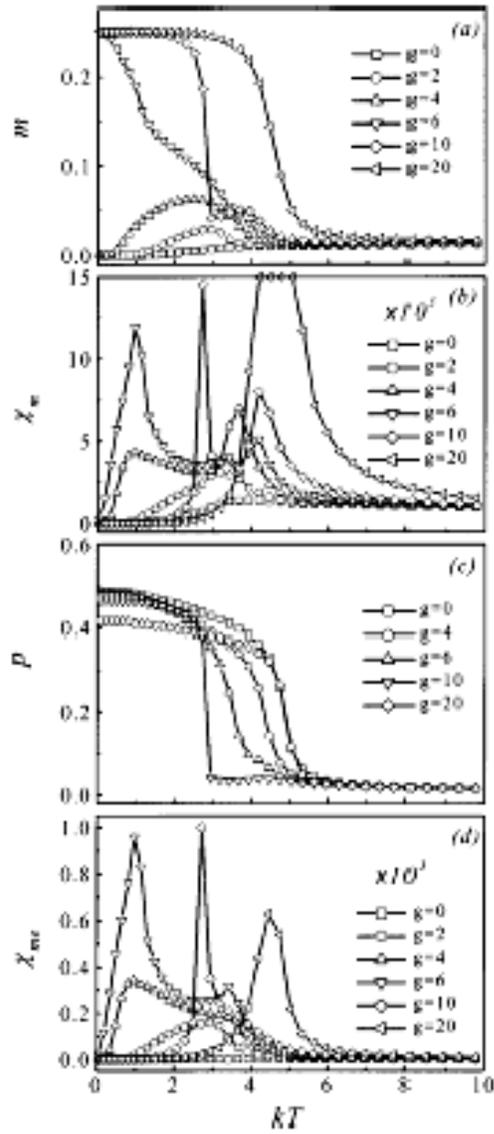
Figure 6.12 Simulated (a) magnetization m, (b) susceptibility $\chi_m$, (c)electric polarization P and (d) the magnetoelectric factor $\chi_{ME}$ as a function of kT at different g in the FE-AFM system. Figure adapted from Liu et al. [117]

rather than antiferromagnetic state is observed; (ii) Both Curie and Neel temperatures are shifted upwards in temperature due to the coupling effect.

Questions in this manner lead to our investigation of the coupling between the electric and magnetic order parameters in $BiFeO_3$ thin films.

## 6.2 ME coupling measurement setup and preliminary results

The ME effect in $BiFeO_3$ thin films under external magnetic field was studied using a small signal susceptibility measurement setup. [119] In this setup, a DC magnetic field ($H_{DC}$) was applied to the sample, superimposed with an AC field ($H_{AC}$) generated by a Helmholtz coil. A lock-in amplifier was used to detect the voltage that develops across the sample, which consists in part of the ME effect, $V_{ME}$, and in part induced by the measuring field $H_{AC}$ due to the finite size of measurement loop ($V_{in}$). Theoretically, these two contributions differ by $\pi/2$ in phase if we assume that the ME coefficient has negligible dispersion (in-phase with stimulation).

$$V_{meas}e^{i\omega t} = V_{ME}e^{i\omega t} + \gamma V_{in}e^{(i\omega t+\frac{\pi}{2})}.$$

The quantity $\gamma$ indicates the magnitude of inductive coupling. [120] By adjusting the reference phase of the lock-in amplifier, we can display $V_{ME}$ in one channel, and $V_{in}$ in the other separated by $90^o$ in phase. However, it is not so straightforward in reality since the resistivity/capacitance of the sample is comparable with the lock-in input impedance. The partial signals detected by the lock-in amplifier (from the two sources respectively) do not always differ by $90^o$. Certain measurement condition needs to be fulfilled to correctly measure the ME coefficient. Details of the circuit analysis are presented in Appendix A (Done by visiting scholar, Chan Gao from UTSC, China. Cited with permission).

Due to the limitation of our lock-in amplifier, we performed the measurements

with $H_{AC}$ at frequencies $\leq$ 100kHz. This limits the accuracy we could achieve. But, care was taken to eliminate the induced voltage from being recorded. In details, $H_{DC}$ was first increased to maximum (4000Oe with our system) where the ME coefficient is expected to be zero. The only signal detected under this condition was the induced voltage, and its phase was recorded. One channel of the lock-in amplifier was then set to display this signal. The signal from the other channel, whose phase was set $90^{o}$ away, was recorded as the $V_{ME}$. Dividing $V_{ME}$ by the $H_{AC}$ amplitude and the film thickness, we then get the ME coefficient in term of V/cm·Oe.

Measurements were performed at 100kHz and 1kHz. Figure 6.13 displays the results observed from 400nm $BiFeO_3$ thin films grown on $SrTiO_3$ (001) substrate with dimension of 5x5x0.5mm. The bottom $SrRuO_3$ electrode is 20nm thick. It is observed that: (i) At low (Hz to kHz) frequency, the ME coefficient is small, ~0.02V/cm·Oe under zero bias; (ii) The observed signal dramatically increases to ~3V/cm·Oe at a measurement frequency of 100kHz; (iii) Resonance like behavior was observed as the large signal drops quickly when measurement frequency shifts away from 100kHz (downwards in our case due to instrument limitation). The nature of this resonance behavior is still unclear. Comparing the results obtained at 1kHz and 100kHz, two common features need to be addressed: (i) Observed signal decreases as applied DC magnetic field increases; (ii) two peaks were observed at DC fields close to the coercive fields obtained from M-H measurements. These are expected features for a susceptibility that is related to magnetic hysteresis loop.

We also compared our observation with reported ME coefficient. Popov et al. measured the induced charge on the surface of a single crystal $BiFeO_3$ sample under high magnetic field, as shown in Figure 6.14. [121] The sharp increase of charge at ~20T is attributed to a field induced phase transition, which is also confirmed by later
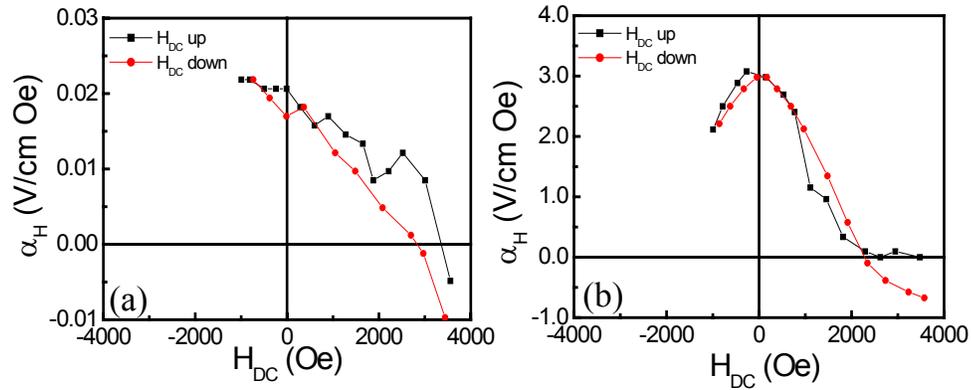
Figure 6.13 ME coefficient ($\alpha_H$) measured using a lock-in technique at (a) 1045 Hz and (b) 100Hz. The sample is $BiFeO_3$ (400nm)/$SrRuO_3$ (20nm)/$SrTiO_3$ (001). The substrate size is 5x5x0.5mm.
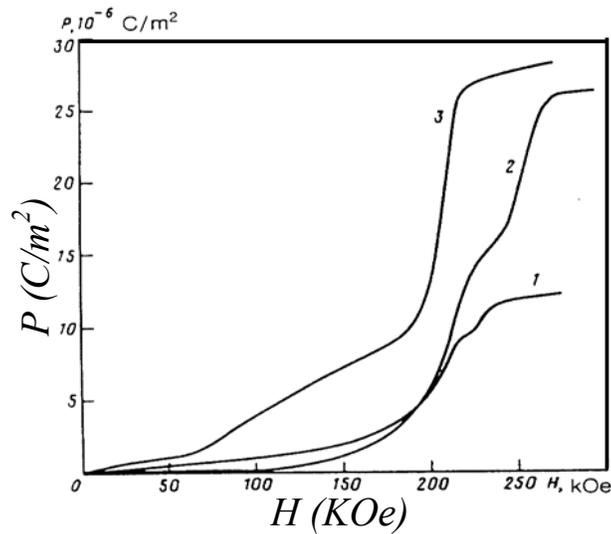


Figure 6.14 Magnetic field induced surface charge of single crystal $BiFeO_3$. The slope of this curve is the ME coefficient in V/cm·Oe. Figure adapted from Popov et al. [121]

experiments. [104, 106] The slope of this curve gives the ME coefficient in terms of V/cm·Oe. As discussed early in this chapter, elastic energy brought the phase transition point down to 0Oe in the thin film system. So we compared the thin film ME signal with the coefficient deduced from Figure 6.14. At around the phase transition, the slope is estimated to be $\sim 0.01$V/cm·Oe, which is of the same order as our low frequency result. These are preliminary results and further study is necessary to understand the coupling mechanism, especially at frequency $\geq 100$kHz.

# CHAPTER 7, INTEGRATION OF BiFeO$_3$ ON Si

In previous chapters, it was demonstrated that high quality BiFeO$_3$ thin films with high resistivity can be deposited by PLD. These films showed large polarizations even higher than that of PZT. They also had high piezoelectric coefficients, offering promise for applications in MEMs. An aspect of concern with the PZT system is its relative toxicity accruing from lead. BiFeO$_3$ provides an alternative choice of a Pb-free ferro/piezoelectric material, which is environmentally preferable. Approaches to grow high quality BiFeO$_3$ films on Si substrates are desirable from application point of view. In this chapter, my work on integrating BiFeO$_3$ with Si substrates is presented. It has also been demonstrated that epitaxial SrTiO$_3$ template layer can be deposited directly on Si by molecular-beam epitaxy (MBE), [122,123] adding in the integration of BiFeO$_3$ with Si technologies. A similar approach has previously been used to integrate PZT with Si. [124,125]

The SrTiO$_3$ coated substrates used in this study were provided by our collaborators. Eisenbeiser et at reported the deposition process. [122] SrTiO$_3$ thin films ~100–150 Å were grown on Si substrates, using a V100 production-type molecular beam epitaxy system (VG Semicon). The base chamber pressure was less than $3\text{-}8\text{x}10^{-10}$ mbar. Sr and Ti metals from effusion cells were used with molecular oxygen to form the epitaxial SrTiO$_3$ film in the temperature range 200–800 °C. Metallic Sr was used to react with the silicon oxide at temperatures greater than 700 °C, and under high vacuum producing a 2x1 surface reconstruction. The authors stated that this method forms a silicate layer, resulting from the reaction of the metallic Sr and silicon oxide. [126] The O$_2$ partial pressure in the growth chamber was varied from $10^{-7}$ to $10^{-5}$ mbar during the growth of the SrTiO$_3$ layer. The Sr and Ti fluxes were adjusted to give a deposition rate of about one monolayer of SrTiO$_3$ per minute. Conventional cross

sectional high resolution transmission electron microscopy was used to examine the crystalline quality of $SrTiO_3$ films as well as the $SrTiO_3$ /Si interface. An extremely thin amorphous interfacial layer was found at the interface.

## 7.1 Structure of BiFeO₃ thin films on Si

### 7.1.1 X-ray and electron diffraction analysis

A typical X-ray θ-2θ scan, Fig7.1 (a), shows only (00l) diffraction peaks from $BiFeO_3$ and $SrRuO_3$ in addition to Si peaks. No reflections were detected that would be indicative of second phases. A phi scan of the $BiFeO_3$ (202) and Si (404) planes is displayed in Figure7.1 (b). Only four sharp peaks originate from $BiFeO_3$ indicating that the film has good in-plane orientation. The inset also reveals a 45˚ rotation of $BiFeO_3$ peaks with respect to those from the Si substrate.

Selected area electron diffraction from a cross section TEM sample, Figure 7.2, confirmed this rotation. The diffraction patterns originating from $SrRuO_3$, $SrTiO_3$ overlap with that from $BiFeO_3$, indicating cubic-on-cubic growth with respect to $SrTiO_3$. These results can be understood based on the lattice match $d_{SRO<100>}$=3.94 Å, $d_{STO<100>}$=3.91 Å with $d_{Si<110>}$=3.82 Å. The out-of-plane lattice constant of $BiFeO_3$ was calculated to be ~3.95 Å (pseudo-cubic unit) for 200nm film, which is smaller than its bulk value. This observation is a consequence of two competing effects: a) the compressive stress imposed by the $SrRuO_3$/$SrTiO_3$ layers, which have in-plane lattice parameters smaller than that of $BiFeO_3$; and b) a tensile stress due to the smaller thermal coefficient of Si compared with that of oxides (Si: $\alpha \sim 3 \times 10^{-6}$ deg$^{-1}$, $BiFeO_3$: $\alpha \sim 6 \times 10^{-5}$ deg$^{-1}$ [24]). Since the films are thicker than the expected critical thickness for dislocation formation, the thermal stress dominates at room temperature, leading to an in-plane tensile stress and the decrease in the out-of-plane lattice parameter.
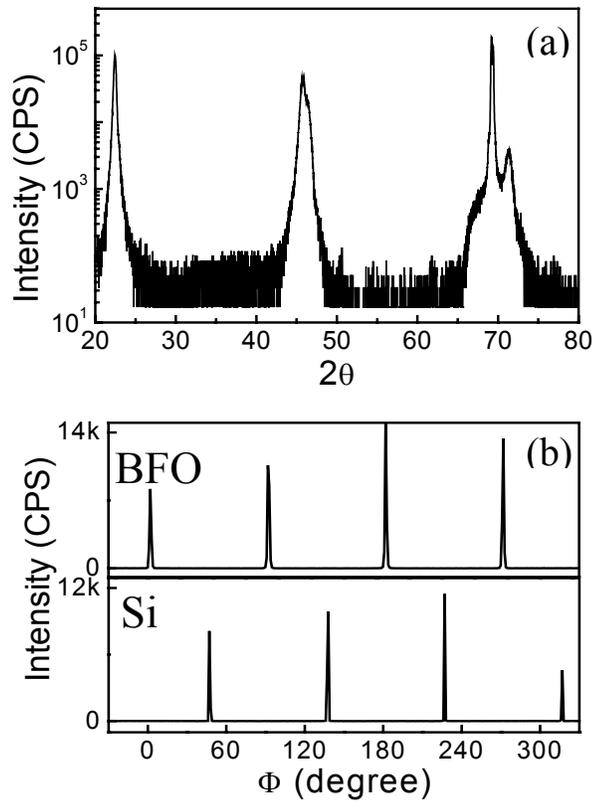
Figure 7. 1 X-ray 2θ scan (a) for BiFeO$_3$ films grown on Si with SrTiO$_3$ as template layer. (b) φ scan of the same sample reveals the 45° rotation between the BiFeO$_3$ and Si unit cells.
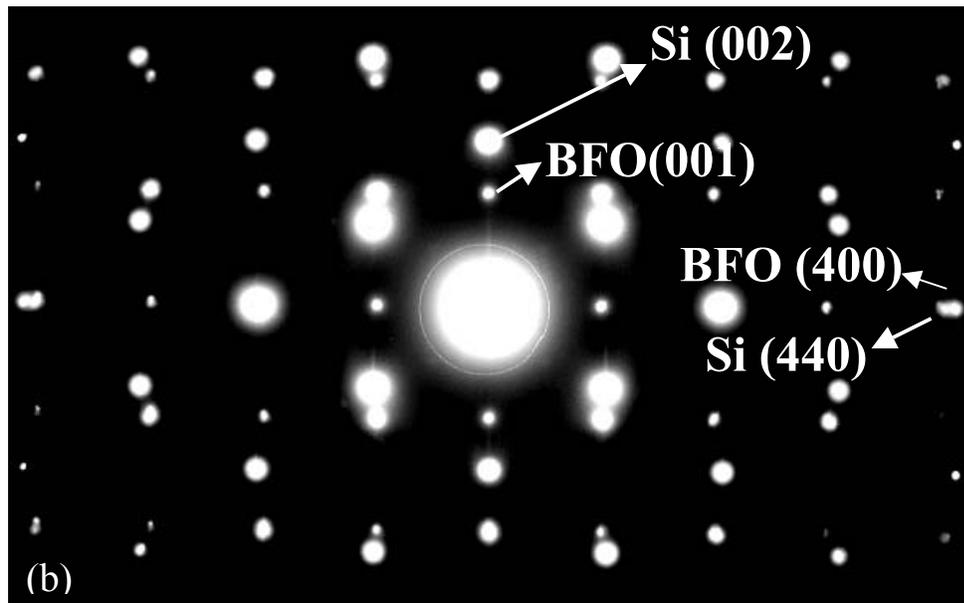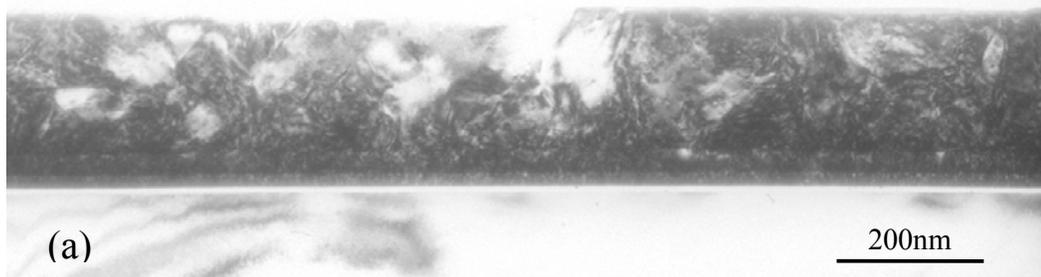
Figure 7. 2 (a) Transmission electron microscopy image showing the clear interfaces.

(b) Selected area electron diffraction pattern confirms the epitaxial growth of $BiFeO_3$

on Si.

141

### 7.1.2 Domain analysis using XRD

Scans of $\omega$-$2\theta$ were performed on typical samples with 200nm and 400nm thick BiFeO$_3$ layers at room temperature. This was done to study the domain structure and lattice evolution. As shown in Figure 7.3, a clear split along $\omega$ was found for the (002) reflection. This is in distinct difference comparing to BiFeO$_3$ films grown directly on SrTiO$_3$, where only a single reflection was found. However, similar mesh scan patterns were found for BiFeO$_3$/SrRuO$_3$/SrTiO$_3$ and BiFeO$_3$/SrRuO$_3$/SrTiO$_3$/Si about (101). Comparing the results for BiFeO$_3$/SrRuO$_3$(20nm)/SrTiO$_3$/Si samples with 200nm and 400nm BiFeO$_3$ layers, we can see that the patterns are quite similar, except that there was considerably more peak broadening along the $\omega$-direction for the thicker film. This clearly indicates a strain gradient in the thicker film, which is expected due to the relaxation of the elastic energy with increasing thickness.

The mesh scan patterns for BiFeO$_3$ films grown on SrTiO$_3$/Si and its difference from the patterns obtained for films grown on SrTiO$_3$ substrates can be explained based on the monoclinic Ma phase. The only difference is that films grown on SrTiO$_3$/Si substrates have their prototypic c-axis (defined for the longer axis) oriented in-plane, where those grown on SrTiO$_3$ substrates have their c-axis lays out-of-plane. Characteristic reciprocal unit cells and expected mesh scans are shown in Figure 4.7 (a) along the (001) and (100) zones; and in Figure 4.7 (b) along the (001) and (101) zones. We can attribute the difference between BiFeO$_3$/SrRuO$_3$/SrTiO$_3$ and BiFeO$_3$/SrRuO$_3$/SrTiO$_3$/Si to the difference in stress state induced by Si, as described earlier. Si has a much smaller thermal expansion coefficient and will stretch the film in-plane during cooling, inducing a larger in-plane lattice constant (c-axis). Then, normal (100) pattern (corresponding the shorter lattice) will be observed when conducting out-of-plane mesh scans. However, (101) pattern will remain the same for
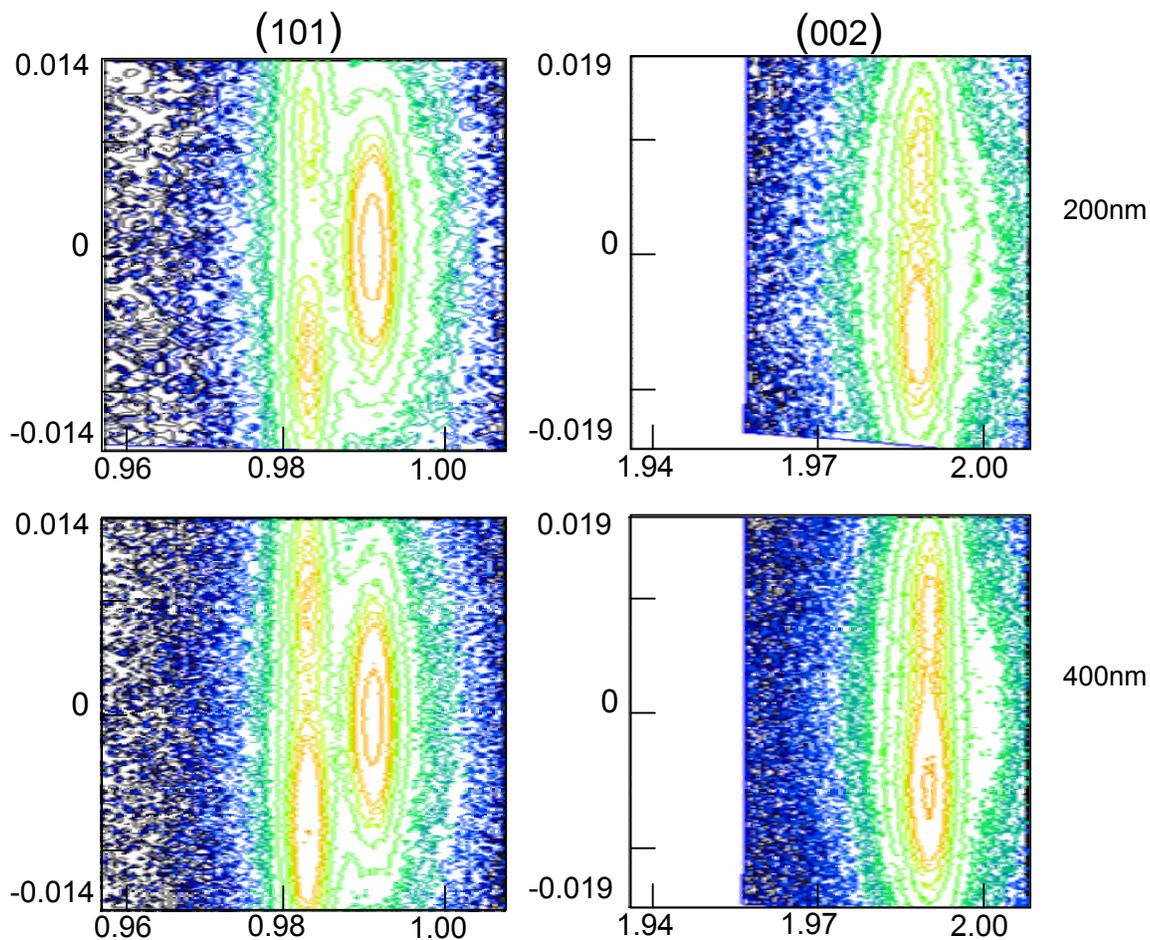
Figure 7. 3 Mesh-scans for two samples with 200nm and 400nm BiFeO$_3$ layers grown on STO-Si substrate with 20nm SrRuO$_3$ electrodes, showing the domain splits of (101) and (002) planes.

both films with the c-axis oriented in- or out-of-plane, which is consistent with our observations.

These reciprocal unit cell + resultant mesh scans (Figure 4.7) are identical to the experimental ones in Figure 7.3. This clearly illustrates the difference between $BiFeO_3$ films grown on $SrRuO_3/SrTiO_3$ (c-axis oriented in-plane), and those grown on $SrRuO_3/SrTiO_3/Si$ (c-axis oriented out-of-plane).

## 7.2 Electrical properties of $BiFeO_3$ on Si

Ferroelectric properties were also characterized using polarization hysteresis, as well as pulsed polarization measurements. Figure 7.4 (a) shows a set of hysteresis loops measured on a 32 μm diameter capacitor at a frequency of 15 kHz. A remnant polarization of $P_r \sim 45$ μC/cm$^2$ is observed, which is smaller than that of films grown on single crystal $SrTiO_3$ substrates (~55 μC/cm$^2$ on [100] $SrTiO_3$ and ~95 μC/cm$^2$ on [111] $SrTiO_3$). [76] This can be understood as a consequence of the smaller c/a ratio of $BiFeO_3$ on Si. The spontaneous polarization of $BiFeO_3$ still lays close to (111)c direction, and the Pr measured along (001) is a projection. The difference between the two films is that, $BiFeO_3$ film on $SrTiO_3$ is compressed in-plane, inducing a larger out of plane lattice (c/a>1); while $BiFeO_3$ grown on Si is stretched in-plane due to the small thermal coefficient of Si, inducing a smaller out-of-plane lattice. Nevertheless, the polarization projection from (111) does not change dramatically. Pulse polarization measurement that are less likely convoluted by leakage and nonlinear dielectric effects, confirmed this result. Figure 7.4 (b) shows the pulsed remnant polarization vs. applied electric field, measured using 10 μsec pulses. We observed an increase of ΔP around 3 V reaching a value of ~100μC/cm$^2$ at 12 V. For use in memory applications, the coercive field (which is currently ~2-3 V) has to be lowered

to about 0.7-1 V. In the case of PZT thin films, this has been shown to be possible through cationic substitutions, which tunes the tetragonality of the material. Our preliminary experiments using La substitution at the Bi–site suggest a similar prospect in the $BiFeO_3$ system. The resistivity of these films is ~$10^9$ $\Omega$.cm at zero bias, decreases to ~$10^8$ $\Omega$.cm under 10V DC bias. The pulse width dependence of $\Delta P$ down to 1 $\mu$sec is shown in Fig. 7.4 (c), slightly increase of the measured $\Delta P$ as pulse width increases reveals contribution from leakage current. The stability of the polar state is confirmed by retention measurements as shown in Fig.7.4 (d). No significant change of the polarization was observed over a period of several days.

Piezoelectric hysteresis loop, Fig.7.5 (a), shows a remnant $d_{33}$ value of 60pm/V for the fully clamped film, which is comparable to that obtained from Ti-rich PZT films (Zr/Ti ratio of 20/80). Figure 7.5 (b) shows the small signal dielectric constant, $\varepsilon_r$, for a 32 $\mu$m capacitor. The observed $\varepsilon_r$ was ~170.

Fatigue of switchable polarization of ferroelectric materials is of great concern for application in memory area. It has been shown that oxygen vacancies accumulated at the metal electrode/oxide interfaces play a big role, and oxide electrode can improve the fatigue property dramatically. [127,128] I have performed fatigue measurements on $BiFeO_3$ thin film using both $Pt/BiFeO_3/SrRuO_3$ and $Pt/SrRuO_3/BiFeO_3/SrRuO_3$ structures deposited on $SrTiO_3$ terminated Si substrates. As shown in Figure 7.6, capacitors with Pt electrodes fatigue after $10^7$ cycles, while those with symmetric oxide electrodes show no sign of fatigue after $10^{11}$ cycles. These observations are consistent with results from PZT system.
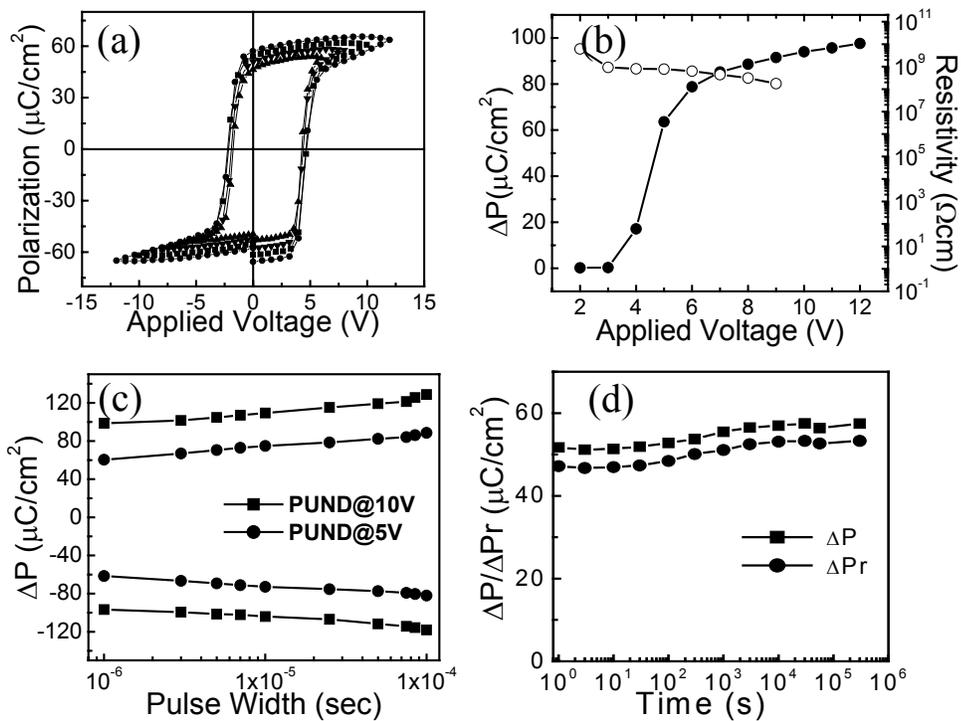
Figure7. 4 (a) Ferroelectric hysteresis measured at a frequency of 15 kHz. The remnant polarization equals ~45 $\mu C/cm^2$. (b) Pulsed polarization, $\Delta P$ vs. electric field, determined with electrical pulses of 10$\mu$sec width and resistivity vs. electric field measured using 1sec pulses. (c) Pulse width dependence of $\Delta P$. (d) Polarization retention showing no significant change after several days.
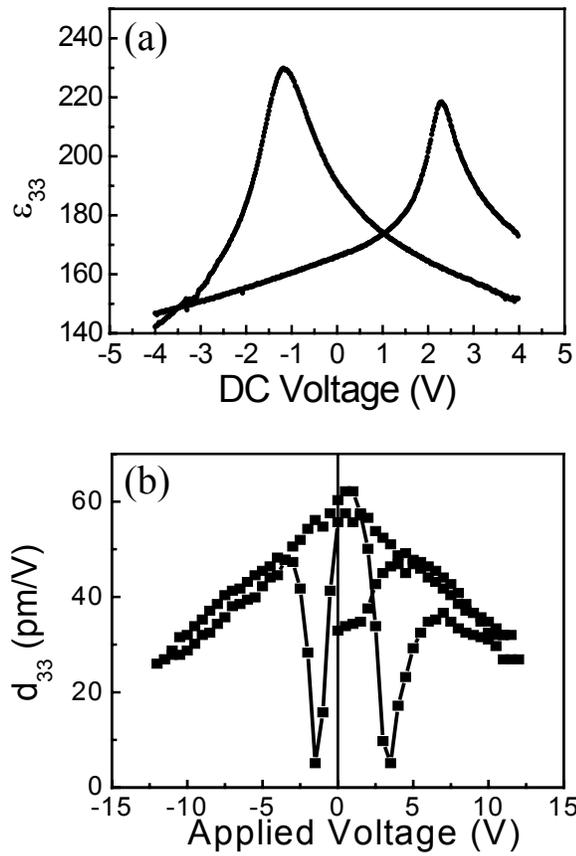
Figure 7. 5 (a) Small signal d33 (b) Small signal dielectric constant, $\varepsilon_r$ of a 32 $\mu$m

capacitor.
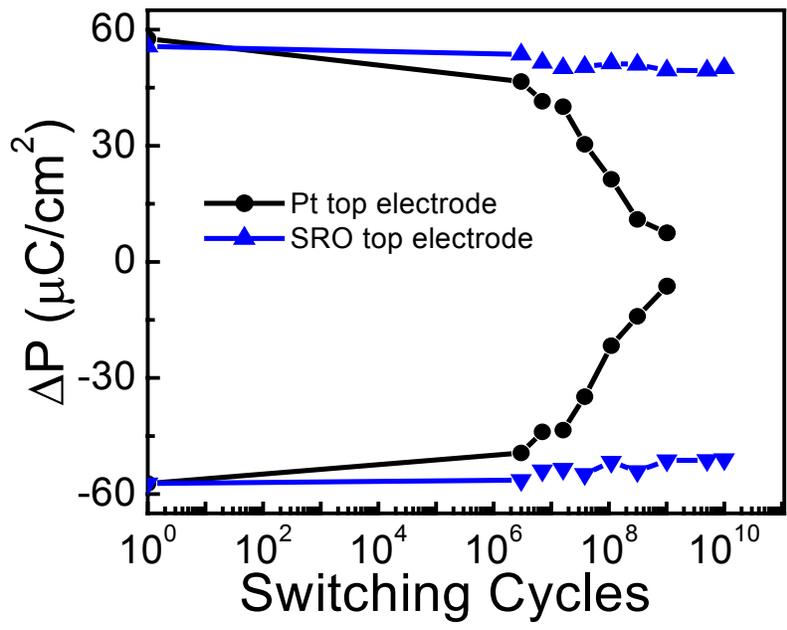
Figure 7. 6 Results of fatigue measurements from Pt/BiFeO$_3$/SrRuO$_3$/SrTiO$_3$/Si (black)

and Pt/SrRuO$_3$/BiFeO$_3$/SrRuO$_3$/SrTiO$_3$/Si (red) with 5V, 10µsec pulses.

## 7.3 Summary

Films with different thickness were grown on Si with the same deposition parameters. The change of lattice parameter, polarization and piezoelectric coefficient were studied. Due to the difference between the thermal coefficients of Si and perovskite oxides, the results are different from films grown on $SrTiO_3$ substrate where the films and substrate have almost the same thermal coefficients and lattice mismatch dominates.

Figure 7.7 (a) clear demonstrates the lattice parameter thickness dependence. As films gets thicker, the $BiFeO_3$ peak shifts to higher $2\theta$ value, indicating a smaller d-spacing. Figure 7.7 (d) summarized this change and shows an interesting feature. The out-of-plane d-spacing actually are actually smaller than the bulk value, also indicated in the figure. I have explained this based on the fact that Si has a much smaller thermal coefficient and stretched the films in plane during cooling. And, this effect does not change with the film thickness since the Si substrate is much thicker. Figure 7.7 (b) summarized the hysteresis loop at different thickness. A larger polarization and coercive field are observed at smaller thickness, which is typical for ferroelectric films on substrates with smaller lattice parameters. This observation is also consistent with $BiFeO_3$ films grown directly on $SrTiO_3$ substrates. A piezoelectric coefficient as large as 120pm/V was observed from films at 400nm thick, showing promise for application in MEMs and actuators. This value progressively decreases to ~30pm/V at 100nm. Again, similar trend was observed for films grown on $SrTiO_3$ substrates.
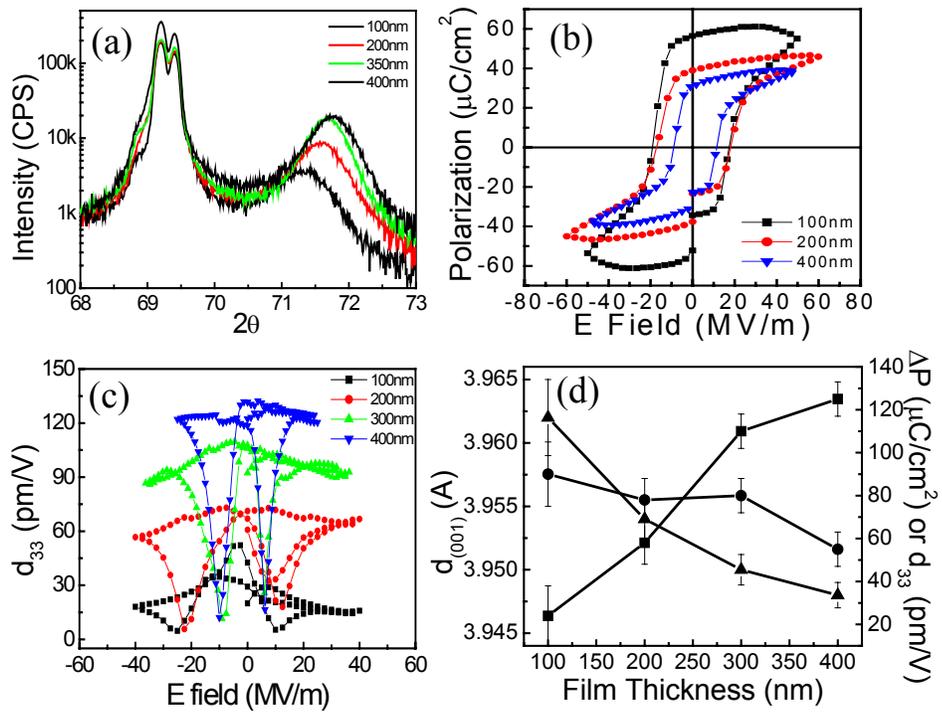
Figure 7. 7 Thickness dependence of (a) out-of-plane d-spacing, (b) polarization (c)

piezoelectric hysteresis loops and (d) summary.

In summary, epitaxial BiFeO$_3$ thin films were grown on Si substrate using a SrTiO$_3$ template layer. A significant polarization, ~45μC/cm$^2$, was observed at room temperature for a 200 nm film. Retention analyses up to several days confirmed the polarization stability. 400 nm thick films possess a large piezoelectric coefficient, ~120 pm/V, which is useful for applications in MEMS and actuators.

# CONCLUSIONS AND FUTURE WORK

In the course of this study, high quality epitaxial multiferroic $BiFeO_3$ thin films were deposited for the first time using pulsed laser deposition. (001), (101) and (111) cut $SrTiO_3$ substrates were used to control the film orientation. Electric and magnetic properties of the films were characterized. Si substrate with $SrTiO_3$ buffer layer was also used, demonstrating the possible integration of $BiFeO_3$ with semiconductor industry.

The main conclusions can be summarized as follows:

(i)     The structure of $BiFeO_3$ thin films is very sensitive to epitaxial constraint. It is observed that (111) oriented film has the same rhombohedral structure as single crystal. However, (001) and (101) oriented films are distorted monoclinically due to the lattice mismatch. Domain splitting was observed in both cases using X-ray diffraction mesh scan. Thickness dependent measurements reveal larger lattice d-spacing even at thickness larger than 400nm, possibly due to oxygen vacancies incorporation.

(ii)    All the $BiFeO_3$ thin films have resistivity of $\sim 10^9 \Omega$ cm, much larger than that of bulk sample. This insulation resistivity enables careful electric characterization at high field. Remnant polarizations ($P_r$) of $\sim 55$ $\mu C/cm^2$ for (001) films, $\sim 80$ $\mu C/cm^2$ for (101) films, and $\sim 100$ $\mu C/cm^2$ for (111) films were observed. A simple calculation shows that the values of $\sqrt{3}$ $P_{(001)}$, $\frac{\sqrt{6}}{2}$ $P_{(101)}$, and $P_{(111)}$ are nearly equivalent, indicating that the spontaneous polarization ($P_s$) lies close to (111). The values observed along (001) and (101) are its projections. Theoretical analysis confirms that $\sim 100$ $\mu C/cm^2$ along (111) is likely the intrinsic spontaneous polarization of $BiFeO_3$, considering

the larger ionic displacements and high Curie temperature. These observed results also demonstrate a common trend between dielectric constant and piezoelectric coefficient; i.e., $\varepsilon_r(001) > \varepsilon_r(101) > \varepsilon_r(111)$ and correspondingly $d_{33}(001) > d_{33}(101) > d_{33}(111)$, with specific values listed in Table 5.3. These observations again confirm that the spontaneous deformation (and polarization) lies along (111).

(iii) Magnetic analysis reveals hysteresis behavior from all three films with different orientations. It is demonstrated that epitaxial stress plays an important role. Elastic energy provided by the substrate destroys the cycloidal modulated spin structure in bulk sample, thus releasing the net magnetization due to spin canting. It is observed that for thin films, (001) oriented film has the largest saturation magnetization, consistent with the largest lattice mismatch (thus largest elastic energy). As films get thicker, saturation magnetization for (001), (101) and (111) oriented films coincide, consistent with relaxation of mismatch strain.

(iv) Integration of $BiFeO_3$ with Si is important from application point of view. One way of doing so is by using $SrTiO_3$ template layer. This process was demonstrated in this work. $BiFeO_3$ thin films grown on $SrTiO_3$ terminated Si substrate demonstrate high polarization and good fatigue properties. Large dielectric and piezoelectric coefficients were also observed.

**Future work**

The availability of high quality $BiFeO_3$ thin films with high resisitivity, large spontaneous polarizations, large piezoelectric and dielectric coefficients provides enormous opportunities. Further investigations in the following directions could prove

fruitful.

(i) With the large polarization and piezoelectric coefficients, $BiFeO_3$ could be a good alternative ferro/piezoelectric material for the current most popular PZT system. It is Pb-free and environmentally preferable. However, its coercive field it too large and piezoelectric needs to be improved from application point of view. One way of doing so is by doping $BiFeO_3$ with other elements, e.g. Lanthanum. As we know, $PbTiO_3$ also has large distortion and high Curie temperature, thus large polarization and coercive field. By doping $PbTiO_3$ with Zirconium, the spontaneous distortion is reduced, and so the polarization and coercive field. At composition close to MPB, large piezoelectric and dielectric coefficients are observed. Previous study reveals that Lanthanum doping in $BiFeO_3$ effectively decreases the Curie temperature, as shown in Figure 8.1. [129] Our preliminary analysis shows that 10% Lanthanum doping doubled the piezoelectric coefficient, indicating a softening of the unit cell. Further investigation in this direction could be fruitful.

(ii) Very large saturation magnetizations were observed in some of the $BiFeO_3$ thin films. It was conjectured that oxygen vacancies and increased canting angle may contribute to the large moments. But, we can not completely eliminate the possibility of second phase contribution, if it is nano-scale. Further study is necessary to clarify this issue. Furthermore, different ways can be used to change/improve the magnetic property of $BiFeO_3$. One way is to carefully engineering the elastic constraint in ultra thin films, thus changing the exchange interaction and the canting angle of neighboring $Fe^{3+}$
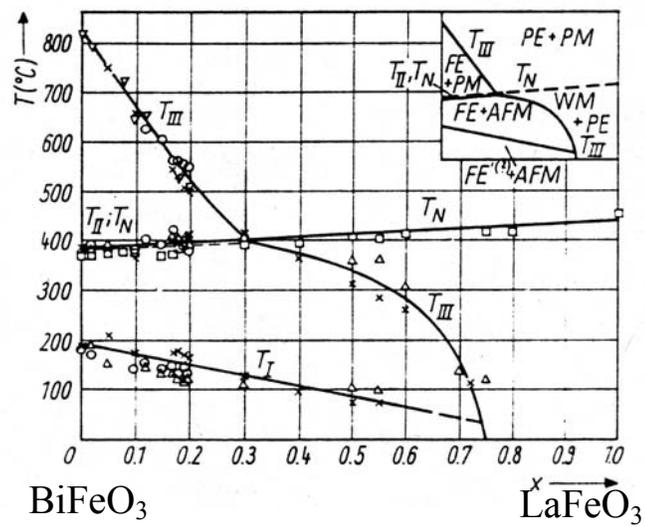
Figure 8. 1 Phase diagram of BiFeO$_3$+LaFeO$_3$ solid solution. Figure adapted from Polosmka et al. [129]
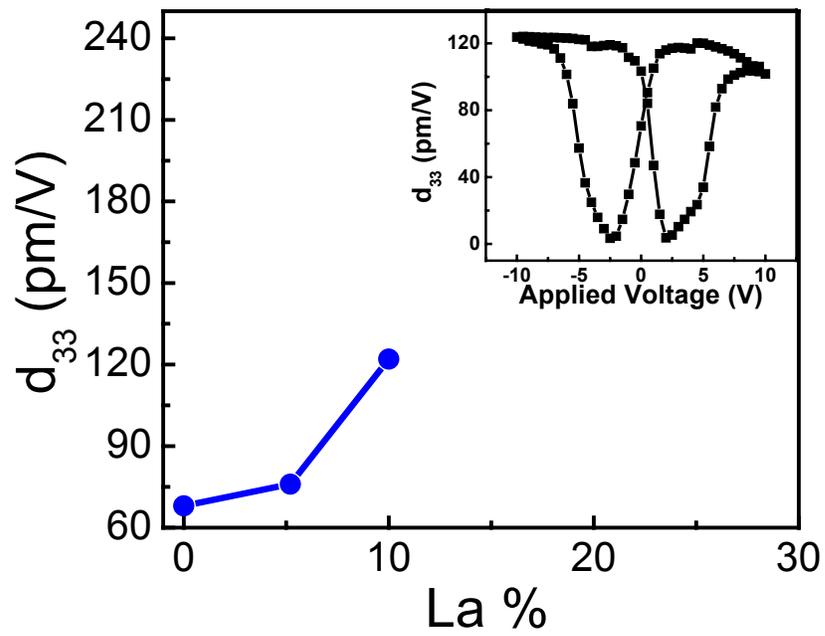
Figure 8. 2 Preliminary results of La doping effect on $BiFeO_3$ using piezoelectric coefficient measurements.

ions. Another way is to substitute part of the $Fe^{3+}$ ions with other magnetic (e.g. Chromium) or nonmagnetic (e.g. Scandium) elements, thus changing the balance of positive and negative spins and the overall magnetic properties.

(iii) Magnetoelectric coupling in single-phase materials is generally small. Preliminary measurements done on $BiFeO_3$ thin films using a lock-in method have revealed a resonance-like feature at ~100kHz, where larger outputs were observed. Further studies in this area are needed.

# APPENDIX A, MODELING OF ME MEASUREMENT

By visiting scholar, Chen Gao from USTC

**System setup and the equivalent circuit**
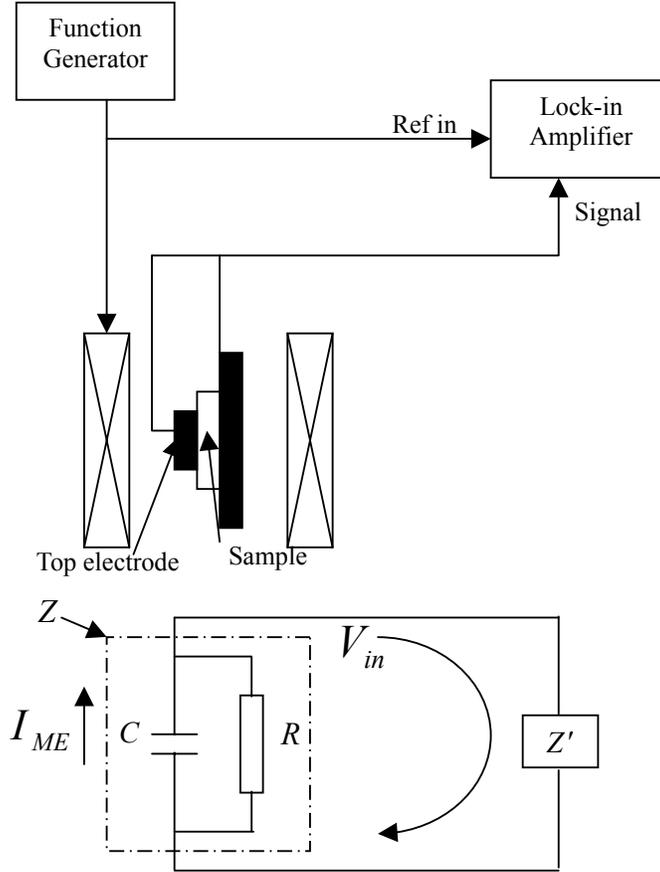


**System analysis**

There are two effects caused by the AC magnetic field: ME and the induction due to the finite area of the measurement loop.

Assume that the sample's capacity is $C$, resistance $R$, and the input impedance of the Lock-in amplifier $Z'$. Then the impedance of the sample is:

$$Z = \frac{R}{1 + j\omega RC},$$

where $\omega$ is the frequency of the AC magnetic field.

1.     Induced voltage

$$V_{in} = \iint \frac{\partial \vec{B}}{\partial t} \cdot d\vec{S} = j\omega \iint \vec{B} \cdot d\vec{S} = j\omega SB,$$

where $S$ is the effective area of the measurement loop, $B$ the amplitude of the AC magnetic field.

2.     ME current

$$I_{ME} = \frac{dQ}{dt} = \frac{d(\sigma s)}{dt} = \frac{dP}{dt}s = \frac{\alpha s}{\mu}\frac{dB}{dt} = j\omega\frac{\alpha s}{\mu}B$$

where $Q$ is the charge on the electrodes of the capacitor, $\sigma$ the surface charge density, $\alpha$, $\mu$ and $s$ are the magnetoelectric coefficient, magnetic susceptibility, and area of the capacitor, respectively.

**Signals**

For the induced voltage, $Z$ and $Z'$ are in series, so the induced voltage and current detected by the lock-in are:

$$I_{in} = \frac{V_{in}}{Z + Z'} = \frac{1}{Z + Z'}j\omega SB$$

$$v_{in} = Z'I_{in} = \frac{Z'}{Z + Z'}j\omega SB$$

For the ME current, $Z$ and $Z'$ are in parallel, so the ME voltage and current detected by the lock-in are:

$$V_{ME} = \frac{ZZ'}{Z + Z'}I_{ME} = \frac{ZZ'}{Z + Z'}j\omega\frac{\alpha s}{\mu}B$$

$$i_{ME} = \frac{V_{ME}}{Z'} = \frac{Z}{Z + Z'}j\omega\frac{\alpha s}{\mu}B$$

**Working condition**

Signal ratios

$$\begin{cases} \dfrac{i_{ME}}{I_{in}} = \dfrac{\dfrac{Z}{Z + Z'}}{\dfrac{1}{Z + Z'}}\dfrac{I_{ME}}{V_{in}} = Z\dfrac{\alpha s}{\mu S} \\[20pt] \dfrac{V_{ME}}{v_{in}} = \dfrac{\dfrac{ZZ'}{Z + Z'}}{\dfrac{Z}{Z + Z'}}\dfrac{I_{ME}}{V_{in}} = Z\dfrac{\alpha s}{\mu S} \end{cases}$$

To conclude:

a) the voltage and current input modes of lock-in give the same results;

b) to separate the induced voltage from the ME signal by adjusting the Lock-in phase, it is required that:

   i)      the phase between $i_{ME}$ and $I_{in}$ (or $V_{ME}$ and $v_{in}$) must be 90°, so that the two components are perpendicular;

   ii)      the phase of $I_{in}$ (or $i_{ME}$, $V_{ME}$, $v_{in}$) with respect to B does not change from sample to sample, so that the system can be calibrated with a non-ME sample.

These two requirements can be expressed as:

   i)      $\Phi_Z = \dfrac{\pi}{2}$ or $\omega RC \gg 1$, indicates that higher measurement frequency, higher sample resistance and capacitance is required;

ii)    $|Z| \gg |Z'|$  or  $|Z| \ll |Z'|$, the first one corresponds to current mode, while the second voltage mode of the lock-in. As  $Z'$  is 10MΩ/25pF for voltage mode, the same order as  $Z$, so, the second inequality is hard to satisfied. However, as  $Z'$  is 1kΩ for current mode, the first inequality can be well satisfied, so it is the only right way of measurement.

Optimized condition
From above analysis, the measurement condition is:
$$\begin{cases} \omega RC \gg 1 \\ |Z| \gg |Z'| \end{cases}$$

then:
$$\begin{cases} i_{ME} = I_{ME} = j\omega \dfrac{\alpha s}{\mu} B \\ I_{in} = \dfrac{V_{in}}{Z} = -\omega^2 SCB \end{cases}$$

and
$$\frac{i_{ME}}{I_{in}} = \frac{1}{j\omega C} \frac{\alpha s}{\mu S} = \frac{\alpha d}{j\omega \varepsilon \mu S}$$

To get larger  $\dfrac{i_{ME}}{I_{in}}$  ratio, we should increase the film thickness  $d$, and decrease the frequency  $\omega$  and loop area  $S$. However, decreasing  $\omega$  contradicts the requirement of  $\omega RC \gg 1$  and increasing  $i_{ME}$.  $\omega$  must be well traded off to balance the two requirements. As a general guide, chose a smallest  $\omega$  while keeping  $\omega RC \gg 1$.

**Typical parameters**
For a typical sample:
$\alpha = 10^{-10}$ C/Am
$\mu = \mu_0 = 4\pi \times 10^{-7}$ C/Am
$s = 0.1 \times 0.1 \, \text{mm}^2$
$S = 1 \times 0.1 \, \text{mm}^2$
$\varepsilon = 200\varepsilon_0 = 200 \times 8.85 \times 10^{-12} \; F/m$
$d = 200 \; nm$
$R = 10 \; M\Omega$
$$C = \varepsilon \frac{s}{d} = 200 \times 8.85 \times 10^{-12} \times \frac{0.1 \times 0.1 \times 10^{-6}}{200 \times 10^{-9}} = 88.5 \; pF$$
Chose                  200kHz,                  so                  that
$\omega RC = 200 \times 10^3 \times 10 \times 10^6 \times 8.85 \times 10^{-12} = 111 \gg 1$  is satisfied.

$$\begin{cases} \dfrac{i_{ME}}{B} = j10^{-6} \ A/T = j0.1 \ nA/Os \\[4mm] \dfrac{i_{ME}}{I_{in}} = \dfrac{1}{j14} \end{cases}$$

or in the other word, the induced current is more than 1 orders magnitude larger than that of ME effect. Its projection is about:

$$I'_{in} = \frac{Z'}{Z} I_{in} = j\omega CR' \frac{1}{j14} i_{ME} = 8\times10^{-3} i_{ME}$$

two orders of magnitude smaller than the ME current.

Under such configuration, the measurement of magnetoelectric coefficient is possible.

# BIBLIOGRAPHY

[1] Kenji Uchino, Ferroelectric devices, (2000)

[2] Ferroelectrics and related materials, Lines and Glass, Oxford (1977)

[3] Aizu, K., J. phys. Soc. Jpn. **19**, 918; **20**, 959. Phys. Rev. **140**, 590; **146**, 423

[4] B. Ruette, MS thesis, Virginia Tech (2003).

[5] W. Cochran, Advan. Phys. **9**, 387 (1960); **10**, 401 (1961)

[6] P. W. Anderson, Fizika dielektrikov (Akad. Nauk, SSSR, Moscow, 1959)

[7] Introduction to Solid State Physics, C. Kittel, (1976)

[8] W. Heisenberg, Z. Physik, **49**, 619 (1928)

[9] Van E. Wood and A. E. Austin, Magnetoelectric interaction phenomena in crystals, edited by A. J. Freeman and H. Schmid, Gordon and Breach Science Publishers, (1975)

[10] Nicola A. Hill, J. Phys. Chem. B **104**, 6694 (2000)

[11] G. A. Smolenskii and I. E. Chupis, Sov. Phys. Usp. **25,** 475 (1982)

[12] Van E. Wood and A. E. Austin, Int. J. Magnetism **5**, 303 (1974) and references therein

[13] J. Van Suchtelen, Philips Res. Rep. **27**, 28 (1972).

[14] J. Ryu, A. Vázquez Carazo, K. Uchino, and H. E. Kim, J. Electroceramics **7**, 17 (2001).

[15] B. T. Cong, N. N. Dinh, D. V. Hien, and N. L. Tuyen, Phyisca B **327**, 370 (2003).

[16] R. P. Mahajan, K. K. Patankar, M. B. Kothale, S. C. Chaudhari, V. L. Mathe, and S. A. Patil, Pramana J. Phys. **58**, 1115 (2002).

[17] J. Ryu, S. Priya, A. Vázquez Carazo, and K. Uchino, J. Am. Ceram. Soc. **84**, 2905 (2001).

[18] J. Ryu, A. Vázquez Carazo, K. Uchino, and H. E. Kim, Jpn. J. Appl. Phys. **40**, 4849 (2001).

[19] L. D. Landau and E. M. Lifshitz, Electrodynamics of Continuous Media, Translation of a Russian edition of 1958

[20] I. E. Dzyaloshinsky, J. Exptl. Theor. Phys. (USSR) **37**, 881 (1959) [Sov. Phys. JETP **37**, 628(1960)

[21] D. N. Astrov, J. Exptl. Theor. Phys. (USSR) **38**, 984 (1960) [Sov. Phys. JETP **11**, 708 (1960)]

[22]  V. J. Folen, G. T. Rado and E. W. Stalder, Phys. Rev. Lett **6**, 607(1961); G. T. Rado and V. J. Folen, Phys. Rev. Lett. **7**, 310 (1961)

[23]  Christian Michel, Jean-Michel Moreau, Gary D. Achenbach, Robert Gerson, and W. J. James, Solit State Communications **7**, 701 (1969)

[24]  J. D. Bucci, B. K. Robertson and W. J. James, J. Appl. Cryst. **5**, 187(1972)

[25]  F. Kubel and H. Schmid, Acta Cryst. **B46**, 698 (1990).

[26] Yu. Ya. Tomashpol'skii, Yu. N. Venevtsev, and G. S. Zhedanov, Soviet Physics-Crystallography **9**, 715(1965)

[27]  P. Fischer, M. Polomaska, I. Sosnowska and M. Szymanski, J. Phys. C: Solid St. Phys. **13**, 1931(1980)

[28]  A. J. Jacobson and B. E. F. Fender, J. Phys. C: Solid State Phys. **3**, 844(1975)

[29]  James R. Teague, Robert Gerson and W. J. James, Solid State Communications **8**, 1073(1970)

[30]  K. Ueda, H. Tabata, and T. Kawai, Appl. Phys. Lett. **79**, 988 (2001)

[31]  V. R. Palkar, J. John, and R. Pinto, Appl. Phys. Lett. **80**, 1628 (2002)

[32]  M. Polomska, W. Kaczmarek and Z. Pajak, Phys. Stat. Sol. (a) **23**, 567(1974)

[33]  I. Sosnowska, T. Peterlin-Neumaier and E. Steichele, J. Phys. C: solid State Phys., **15**, 4835 (1982)

[34]  I. Sosnowska, M. Loewenhaupt, W. I. F. Davie and R. M. Ibberson, Physica B, **180&181**, 117 (1992)

[35]  S. V. Kiselev, R. P. Ozerov and G. S. Zhdanov, Sov. Phys. Dokl, Vol. **7**, 742(1963)

[36]  V. R. Palkar, J. John, and R. Pinto, Appl. Phys. Lett. **80**, 1628(2002)

[37]  S. V. Kiselev, R. P. Ozerov and G. S. Zhdanov, Sov. Phys. Dokl, Vol. **7**, 742(1963)

[38]  I. Sosnowska, T. Peterlin-Neumaier and E. Steichele, J. Phys. C: solid State Phys. **15**, 4835 (1982)

[39]  I. Sosnowska, M. Loewenhaupt, W. I. F. Davie, R. M. Ibberson, Physica B **180&181**, 117 (1992)

[40]  A. M. Kadomtseva, A. K. Zvezdin, Yu. F. Popov, A. P. Pyatakov, and G. P. Vorob'ev, JETP Lett. **79**, 571 (2004)

[41]  Yu. F. Popov, A. M. Kadomtseva, S. S. Krotov, D. V. Belov, G. P. Vorob'ev, P. N. Makhov, and A. K. Zvezdin, Low Temperature Physics, **27**, 478 (2001)

[42]  T. J. Jackson, S. B. Palmer, J. Phys. D: Appl. Phys. **27**, 1581 (1994).

[43]  Hao Li, Ph.D thesis, University of Maryland, College Park, (2001)

[44] Haimei Zheng, Ph.D thesis, University of Maryland, College Park, (2004)

[45] H. Maiwa, N. Ichinose, Jpn. J. Appl. Phys. Part 1-Regular papers, short notes and review papers **39**, 5403 (2000)

[46] S. Buhlman, B. Dwir, J. Baborowski, P.Muralt, Appl. Phys. Lett. **75**, 3195 (2002)

[47] V. Nagarajan, et al., Appl. Phys. Lett. **81**, 4215 (2002).

[48] K.-H. Hellwege, A. M. Hellwege, Eds., Landolt-Börnstein, Numerical Data and Functional Relationships in Science and Technology **16**, Springer Verlag, Berlin (1981).

[49] C. Harnegea, M. Alexe, Presented at the 2001 Fall MRS , Boston (2001)

[50] F. Xu, et al., J. Appl. Phys. **89**, 1336 (2001)

[51] C. W. Jones, P. D. Battle, and P. Lightfoo, Acta Cryst. **C45**, 365(1989).

[52] J. C. Jiang, X.Q. Pan, Philosophical Magazine Letters, **80**, 271 (2000).

[53] V. G. Koukhar, N. A. Pertsev and R. Waser, Physical Review B **64**, 214103 (2001)

[54] Alexander L. Roytburd, J. Appl. Phys. **83**, 228 (1998).

[55] Alexander L. Roytburd, J. Appl. Phys. **83**, 239(1998)

[56] A. G. Zembilgotov, N. A. Pertsev, H. Kohlstedt, and R. Waser, J. Appl. Phys. **91**, 2247 (2002)

[57] V. Nagarajan, I. G. Jenkins, S. P. Aplay, H. Li, S. Aggarwal, L. Salamanca-Riba, A. L. Roytburd and R. Ramesh, J. Appl. Phys. **86**, 595 (1999).

[58] S. P. Alpay, V. Nagarajan, L. A. Bendersky, M. D. Vaudin, S. Aggarwal, R. Ramesh, and A. L. Roytburd, J. of Appl. Phys. **85**, 3271 (1999).

[59] J. S. Speck and W. Pompe, J. Appl. Phys. **76**, 466(1994).

[60] S. P. Alpay and A. L. Roytburd, J. Appl. Phys. **83**, 4714 (1998)

[61] W. J. Burke, and R. J. Pressley, Solid State Communications **7**, 1187, (1969).

[62] W. J. Burke, and R. J. Pressley, Solid State Communications **9**, 191 (1971).

[63] Hiromoto Uwe, and Tunetaro Sakudo, Physical Review B **13**, 271 (1976).

[64] N. A. Pertsev, A. K. Tagantsev, and N. Setter, Physical Review B **61**, R825 (2000).

[65] J. F. Li, J. Wang, N. Wang, F. Bai, B. Ruette, A. P. Pyatakov, M. Wuttig, R. Ramesh, A. K. Zvezdin, and D. Viehland, Appl. Phys. Lett. **84**, 5261 (2004)

[66] A. M. Glazer, Acta Cryst., **B28**, 3384 (1972)

[67] A. M. Glazer, Acta. Cryst., **A31**, 756 (1975)

[68] H. Shmid, "Some supplementing comments on the proceedings of MEIPIC-5", (2004)

[69]  Yu. E. Roginskaya, Yu. Ya. Tomashpol'skii, Yu. N. Venevtsev, V. M. Petrov, G. S. Zhdanov. Soviet Physics JETP **23**, 47 (1966).

[70]  P. Fischer, M. Polomska, I. Sosnowska, and M. Szymanski, J. Phys. C: Solid St. Phys. **13**, 1931 (1980).

[71]  B. Nagaraj, S. Aggarwal, and R. Ramesh, J. Appl. Phys. **90**, 375 (2001).

[72]  Y. P. Wang, L. Zhou, M. F. Zhang, X. Y. Chen, J.-M. Liu and Z. G. Liu, Appl. Phys. Lett. **84**, 1731 (2004)

[73]  M. Mahesh Kumar, V. R. Palkar, K. Srinivas, and S. V. Suryanarayana, Appl. Phys. Lett. **76**, 2764 (2000)

[74]  Yu. E. Roginskaya, Yu. Ya. Tomashpol'skii, Yu. N. Venevtsev, V. M. Petrov, and G. S. Zhdanov, Soviet Physics JETP **23**, 47(1966)

[75]  Seung-Eek Park and Thomas R. Shrout, J. Appl. Phys. **82**, 1804 (1997)

[76]  J. Wang et al., Science **299**, 1719 (2003)

[77]  S. C. Abrahams, S. K. Kurtz, and P. b. Jamieson, Physical Review **172**, 551(1968)

[78]  "Proceedings of the International Conference on Theoretical Physics, Kyoto and Tokyo", P. 824 (Science Council of Japan, Tokyo, 1954)

[79]  J. B. Neaton, C. Ederer, U. V. Waghmare, N. A. Spaldin, and K. M. Rabe, submitted (2004).

[80]  N. A. Pertsev, V. G. Kukhar, H. Kohlstedt and R. Waser, Physical Review B **67**, 054107 (2003).

[81]  A. G. Zembilgotov, N. A. Pertsev, H. Kohlstedt and R. Waser, J. Appl. Phys. **91**, 2247 (2002)

[82]  V. Nagarajan, I. G. Jenkins, S. P. Alpay, H. Li, S. Aggarwal, L. Salamanca-Riba, A. L. Roytburd and R. Ramesh, J. Appl. Phys. **86**, 595 (1999)

[83]  V. Nagarajan, S. P. Alpay, C. S. Ganpule, B. K. Nagaraj, S. Aggarwal, E. D. Williams, A. L. Roytburd and R. Ramesh, Appl. Phys. Lett. **77**, 438 (2000)

[84]  Janovec V, 1958, Czech. J. Phys. **8**, 3(1958)

[85]  Kay H. F. Nd Dunn J. W., Phil. Mag. **7**, 2027 (1962)

[86]  M. Dawber, P. Chandra, P. B. Littlewood, and J. F. Scott, J. Phys.: Condens. Matter **15**, L393 (2003)

[87]  S. V. Kiselev, R. P. Ozerov, and G. S. Zhdanov, Dokl. Akad. Nauk SSSR **145**, 1255 (1962) [Sov. Phys. Dokl. **7**, 742 (1962)]

[88]  Claude Ederer and Nicola A. Spaldin, Submitted (2004)

[89] Sosnowsak I., Sosnowski J., Kiselev C. V., Kshniakina A. N., and Ozerov R. P., JINR Dubna Rep. **NO. 2653**, (1966)

[90] I. Sosnowska, T. Peterlin-Neumaier, and E. Steichele, J. Phys. C **15**, 4835 (1982)

[91] I. Sosnovska, Ferroelectrics **79**, 127 (1988).

[92] A. Zalesskii, A. Zvezdin, A. Frolov, and A. Bush, JETP Lett. **71**, 465 (2000).

[93] A. V. Zalesskii, A. A. Frolov, T. A. Khimich, A. A. Bush, V. S., Pokatilov, and A. K. Zvezdin, Europhys. Lett. **50**, 547 (2000).

[94] I. Sosnowska , AK. Zvezdin, Jaumal of Magnetism and Magnetic Materials 140-144 (1995) 167-168

[95] A. M. Kadomtseva, A. K. Zvezdin, Yu. F. Popov, A. P. Pyatakov, and G. P. Vorob'ev, JETP Letters **79**, 571 (2004)

[96] Yu.N. Venevtsev, V.V. Gagulin, V.N. Lubimov, Ferroelectromagnetics, Nauka, Moscow, 1982 (in Russian)

[97] H. Schmid, Int. Z. Magnetism **4**, 337 (1973).

[98] H.Schmid, Magnetoelectric Interaction Phenomena in Crystals, A.Z. Fraeman and H.L.Schmid (Editors), pp. 121-146 (Gordan and Breach, New York, 1975)

[99] C. Eom, R.J. Cava, R. Fleming and J. Phillips, Science **258**, 1766 (1992).

[100] J. M. Longo, P. M. Raccah and J. B. Goodenough, J. Appl. Phys. **39**, 1327 (1968)

[101] R. Blinc and A. P. Levanyuk, North Holland, New York (1986)

[102] Y. Imry and S. Ma, Phys. Rev. Lett. **35**, 1399 (1975)

[103] W. Palme et al, Phys. Rev. Lett. **76**, 4817 (1996)

[104] Benjamin Ruette, S. Zvyagin, A. P. Pyatakov, A. Bush, J. F. Li, V. I. Belotelov, A. K. Zvezdin and D. Viehland, Phys. Rev. B **69**, 064114 (2004)

[105] Yu.F. Popov, A.M. Kadomtseva, A.K. Zvezdin, et al., in Magnetoelectronic Phenomena in Crystals, Edited by Manfred Fiebig, Kluwer Academic, Boston, (2004)

[106] A. M. Kadomtseva, A. K. Zvezdin, Yu. F. Popov, A. P. Pyatakov, and G. P. vorob'ev, JETP Letters **79**, 705(2004)

[107] I. Sosnowska, W. Schafer, W. Kockelmann, K. H. Andersen, and I. O. Troyanchuk, Appl. Phys. A **74**, S1040 (2002)

[108] I. E. Dzyaloshinskii, Sov. Phys. JETP **5**, 1259 (1957)

[109] T. Moriya, Phys. Rev. **120**, 91 (1960)

[110] P. Bak and M. H. Jensen, J. Phys. C **13**, L881 (1980)

[111] G. Shirane, R. Cowley, C. Maikrzak, J. B. Sokoloff, B. Pagonis, C. H. Perry, and

Y. Ishikawa, Phys. Rev. B **28**, 6251 (1983)

[112] D. Viehland, F. Tito, E. McLaughlin, H. Robinson, R. Janus, L. Ewart, and J. Powers, J. Appl. Phys. **90**, 1496-1500 (2001)

[113] A. Weisse, H. Fehske, Journal of Magnetism and Magnetic Materials, **272-276**, pt.1, (2004)

[114] L. D. Landau and E. M. Lifshitz, Electrodynamics of Continuous Media (Addison-Wesley, Reading, MA, 1960)

[115] J. F. Scott, Phys. Rev. B **16**, 2329 (1977)

[116] P. Toledano, Ferroelectrics **161**, 257 (1997)

[117] See for example, J.-M. Liu, Q. C. Li, X. S. Gao, Y. Yang, Physical Review B **66**, no.5, 054416, (2002)

[118] T. Janssen, Ferroelectrics **162**, 265 (1994)

[119] G. Harshe, Ph.D. thesis, PennState University, (1991)

[120] S. Stein, M. Wuttig, D.Viehland, and E. Quandt, submitted, (2004)

[121] Yu. F. Popov et al., JETP Lett. **57,** (1993)

[122] K. Eisenbeiser, J. M. Finder, Z. Yu, J. Ramdani, J. A. Curless, J. A. Hallmark, R. Droopad, W. J. Ooms, L. Salem, S. Bradshaw, and C. D. Overgaard, Appl. Phys. Lett. **76**, 1324 (2000).

[123] R. A. McKee, F. J. Walker, and M. F. Chisholm, Phys. Rev. Lett. **81**, 3014 (1998).

[124] Y. Wang, C. Ganpule, B. T. Liu, H. Li, K. Mori, B. Hill, M. Wuttig, R. Ramesha J. Finder, Z. Yu, R. Droopad, and K. Eisenbeiser, Appl. Phys. Lett. **80**, 97 (2002).

[125] B. T. Liu, K. Maki, Y. So, V. Nagarajan, R. Ramesha, J. Lettieri, J. H. Haeni, D. G. Schlom, W. Tian, X. Q. Pan, F. J. Walker, and R. A. McKee, Appl. Phys. Lett. **80**, 4801 (2002).

[126] J. Wang, J. Hallmark, D. S. Marshall, W. J. Ooms, P. Ordejon, J. Junquera, X. Hu, X. Yao, and D. Sarid, Presented at the APS Centennial Meeting, Atlanta, GA, USA March 20–26 (1999).

[127] R. Ramesh et al., Appl. Phys. Lett. **61**, 1537 (1992)

[128] C. B. Eom et al., Appl. Phys. Lett. **63**, 2570 (1993)

[129] M. Polomska, W. Kaczmarek and Z. Pajak, Phys. Stat. Sol. (a) **23**, 567 (1974)